Photo-induced dynamics in complex materials probed with femtosecond x-rays and few-cycle optical pulses

Simon Wall

St. Johns College, Oxford

Submitted for the degree of Doctor of Philosophy

Trinity Term 2009

Abstract

This thesis reports on experiments and simulations of ultrafast dynamics in correlated materials. Using some of the shortest pulses of light currently available, the response of correlated materials to prompt excitation is probed on their fundamental timescale. Experiments are performed over a broad spectral range, from IR to the hard X-rays, highlighting physics unseen to date.

Photo-induced melting of the Mott state in the 1D organic (BEDT-TTF)-F_2TCNQ was measured using frequency resolved IR pump-probe spectroscopy with 10 fs resolution. By detecting the change in reflectivity at different wavelengths, the melting of Mott phase was observed, and compared to a many-body quantum model to reveal the formation of a coherent state that rapidly de-phased into a collection of localized excitons.

Colossal magneto-resistive manganites were also measured with 10 fs resolution, focusing on transitions at visible wavelengths. The photo-induced dynamics of the parent compound, $LaMnO_3$, demonstrate the coupling between the light field, electrons, lattice, spins and orbital degrees of freedom. These results provide a mechanism through-which light can influence the magnetic state of the material. The photo-induced phase transition in the doped manganite $Pr_{0.7}Ca_{0.3}MnO_3$ was investigated by measuring the timescale on which the phase transition occurs. Evidence for the observation of a high-energy quasi-particle called the orbiton is also presented and discussed. Time resolved X-ray absorption spectroscopy was used to understand the nature of the photo-induced phase by measuring the changes in the unoccupied electronic density of states near the Fermi-level.

Finally, simulations of phonon-polariton propagation were performed in order to interpret femtosecond hard X-ray diffraction measurements in $LiTaO_3$. The simulations showed that the lattice vibrates at a frequency of 1.2 THz, with atomic displacements of order 5 mÅ

Role of the author

Much of the research presented in this thesis was the result of several multi-national collaborations. Unless clearly stated, the data acquisition and analysis presented in this thesis was performed by the author.

The measurements presented in chapter 4 where performed using the IR-OPA at the Politecnico Di Milano in collaboration with D. Brida and G. Cerullo, who helped with data accumulation. H. Okamoto, at the university of Tokyo, provided the static reflectivity data. Quantum many body simulations, used to interpret the dynamics, were provided by S. Clarke and D. Jaksch at Oxford University.

The results on $LaMnO_3$ presented in chapter 5 are entirely the work of the author, including the design and construction of two independent visible NOPAs.

Resistivity measurements presented in chapter 6 were performed by M. Rini at the Lawrence Berkeley National Laboratory. Pump-probe experiments were performed using the visible NOPAs at the Politecnico Di Milano in collaboration with D. Polli and G. Cerullo. The author helped with the data accumulation and performed the data analysis.

The XANES measurements in chapter 7 were a result of a collaboration with the group of R. W. Schoenlein at the Lawrence Berkeley National Laboratory. The author played a significant role in the experimental setup and data accumulation, and performed the data analysis together with M. Rini.

The X-ray diffraction results in chapter 8 were measured by A. Cavalleri and collaborators. The author adapted FDTD code, written by D. Ward at Massachusetts Institute of Technology, in order to simulate the experimental conditions. Further optimization of the program was made by C. Simpson.

Acknowledgements

My time as a DPhil student has been an enjoyable one, mainly due to people that I have had the pleasure to work with. I am indebted to my supervisor, Andrea Cavalleri, for introducing me to an area of physics I previously knew nothing about, for the enthusiasm and insight he has for the subject, his personal support and his willingness to send me all over the world.

I couldnt have asked for a better research group, both socially and scientifically. The frequent Friday night beers will be sorely missed. I would particularly like to thank Ron Tobey and Nicky Dean for really making a group out of the previous two-man operation and Henri Ehrke, particularly for inviting me to many long days and nights at Diamond. Again, I would like to thank Ron for his guidance on how to build a decent experiment and his 'no dogs' and 'line of holes' philosophy. Everyone in the office, both past and present has made it a great working experience and environment, one which is unlikely to be replicated.

I will always be grateful to Simon Hooker, Charlotte Woolley, Tom Robinson and Kevin O'Keeffe for allowing me to use their lab when mine was nothing but a building site, and then letting me drill a hole in their wall in order to take their laser when mine wasn't working.

I would like to thank my collaborators for the many successful collaborations, in particular, Bob Schoenlein, Matteo Rini and Yi Zhu in Berkeley, Giulio Cerullo, Daniele Brida, Dario Polli in Milan and recently Stephen Clark in Oxford.

Finally, I would like to thank my parents for their unquestioning support.

Author's publications

- Coherent Evolution of Mott Excitations Captured on the Time Scale of Electron Correlations
  S. Wall, D. Brida, H. P. Ehrke, S. R. Clark, D. Jaksch, A. Ardavan, S. Bonora, H. Matsusaki H. Uemura, Y. Takahashi, T. Hasegawa, H. Okamoto, G. Cerullo, A. Cavalleri
  In preparation

- Probing transient orbital order in a photo-doped manganite
  H. Ehrke, R. I. Tobey, S. Wall, D. Prabhakaran, A. T. Boothroyd, M. Gensch, P. Reutler, A. Revcolevschi, S. A. Cavill, S. S. Dhesi, A. Cavalleri
  In preparation

- Transient electronic structure of the photoinduced phase of $Pr_{0.7}Ca_{0.3}MnO_3$ probed with soft x-ray pulses
  M. Rini, Y. Zhu, S. Wall, R. I. Tobey, H. Ehrke, T. Garl, J. W. Freeland, Y. Tomioka, Y. Tokura, A. Cavalleri and R. W. Schoenlein
  Physical Review B. **80**, 155113 (2009)

- Ultrafast coupling between light, coherent lattice vibrations, and the magnetic structure of semicovalent $LaMnO_3$
  S. Wall, D. Prabhakaran, A. T. Boothroyd, and A. Cavalleri
  Physical Review Letters. **103**, 097402 (2009)

- Optical switching in VO_2 films by below-gap excitation
  M. Rini, Z. Hao, R. W. Schoenlein, C. Giannetti, F. Parmigiani, S. Fourmaux, J. C. Kieffer, A. Fujimori, M. Onoda, S. Wall, and A. Cavalleri.
  Applied Physics Letters. **92**, 181904 (2008)

- Coherent orbital waves in the photo-induced insulatormetal dynamics of a magnetoresistive manganite
  D. Polli*, M. Rini*, S. Wall*, R. W. Schoenlein, Y. Tomioka, Y. Tokura, G. Cerullo, A. Cavalleri.
  Nature Materials **6**, 643 - 647 (2007)

- Tracking the motion of charges in a terahertz light field by femtosecond X-ray diffraction
  A. Cavalleri, S. Wall, C. Simpson, E. Statz, D. W. Ward, K. A. Nelson, M. Rini, R. W. Schoenlein.
  Nature **442**, 664 - 666 (2006)

Contents

1 Introduction **1**

1.1 Ultrafast science . . . 1

1.2 Strongly correlated electron materials . . . 3

1.2.1 Band theory . . . 3

1.2.2 The Peierls distortion . . . 4

1.2.3 Correlation effects . . . 5

1.2.4 Control of materials . . . 6

1.3 Photo-induced phase transitions . . . 7

1.3.1 Probing materials on their fundamental timescale . . . 8

2 Strong correlations and complex manganites **11**

2.1 Mott insulators . . . 11

2.2 The Manganites . . . 13

2.2.1 Crystallographic and electronic structure . . . 15

2.2.2 Properties of manganites . . . 16

2.2.3 Models for the manganites . . . 21

3 Short pulse generation and the pump-probe technique **27**

3.1 Introduction . . . 27

3.2 Short pulse generation using optical parametric amplifiers . . . 28

3.2.1 Non-linear optics . . . 28

3.2.2 Short pulse generation at near-IR wavelengths . . . 30

3.2.3 Short pulse generation at visible wavelengths . . . 33

3.3 Femtosecond X-rays generated using the slicing technique . . . 37

3.4 Pump-probe . . . 41

3.4.1 Transient reflectivity and coherent phonon generation . . . 42

4 Photoinduced dynamics of a 1D Mott insulator **49**

4.1 Melting the Mott state with light . . . 49

4.2 BEDT-TTF F_2TCNQ . . . 51

4.3 Photo-induced melting of the Mott state . . . 53
4.3.1 Experimental setup . . . 53
4.3.2 Long timescale dynamics . . . 54
4.3.3 Response of the Mott gap . . . 58
4.4 Fitting the optical properties of the Mott gap . . . 62
4.4.1 Quantum simulation of the Mott dynamics . . . 67
4.5 Summary . . . 71

5 Magneto-elastic dynamics of $LaMnO_3$ 73
5.1 Introduction . . . 73
5.2 Static properties of $LaMnO_3$ . . . 74
5.2.1 Optical Properties . . . 75
5.3 Experimental setup . . . 76
5.4 Experimental results . . . 78
5.4.1 Origin of the magneto-elastic interaction . . . 88
5.5 Summary . . . 89

6 Dynamics of the Insulator-Metal phase transition 91
6.1 Photo-induced Insulator-Metal phase transition . . . 91
6.2 The insulator-to-metal phase transition on the ultrafast timescale. . . . 93
6.2.1 Transient metallic measurements . . . 93
6.2.2 Ultrafast changes in reflectivity: Low Temperature . . . 94
6.2.3 Ultrafast changes in reflectivity: High Temperature . . . 100
6.2.4 Orbitons . . . 102

7 Time resolved XANES spectroscopy of $Pr_{0.7}Ca_{0.3}MnO_3$ 105
7.1 XANES spectroscopy . . . 105
7.1.1 Static XANES spectra of $Pr_{0.7}Ca_{0.3}MnO_3$ . . . 106
7.1.2 Insulator-to-metal transition in XANES measurements . . . 108
7.2 Time resolved XANES . . . 109
7.2.1 Experimental setup . . . 110
7.2.2 Picosecond XANES . . . 113
7.3 Summary and conclusions . . . 116

8 Femtosecond X-ray diffraction 119
8.1 Introduction . . . 119
8.2 Phonon-Polaritons . . . 120
8.2.1 Light propagation in an IR active material . . . 120
8.3 Time resolved diffraction . . . 123
8.3.1 Kinematic diffraction . . . 123

8.3.2 Phonon effects on the diffraction signal 123
8.4 Experimental details and results 124
8.4.1 Properties of $LiTaO_3$ 124
8.4.2 Generation of THz waves from ISRS 127
8.4.3 Experimental setup 128
8.5 Simulation of phonon-polaritons 130
8.5.1 Phonon-polaritons propagation and Maxwell's equations 130
8.5.2 The Finite Difference Time Domain technique 132
8.5.3 Simulation details 133
8.5.4 Polariton propagation results 135
8.5.5 Simulation of diffraction signal 138
8.6 Comparison of the simulation and data 140

9 Summary and outlook 143
9.1 Summary of thesis 143
9.1.1 Dynamics in a 1D Mott insulator 143
9.1.2 Dynamics in manganites 144
9.2 Future directions 145

A Synchronization and timing between laser and X-ray sources 147

List of Figures

1.1 'The Horse in Motion' by Eadweard Muybridge. 2
1.2 Band structure diagrams 4
1.3 The Peierls transition 5

2.1 Band diagrams of Mott and charge transfer insulators 14
2.2 The ideal ABO_3 cubic perovskite crystal structure. 15
2.3 The electronic structure of the Mn ion within the crystal field. 16
2.4 Phase diagrams for low, intermediate and high bandwidth manganites. 17
2.5 Changes in resistivity as a function of temperature, pressures and magnetic fields 20

3.1 Schematic of a near-IR OPA 31
3.2 The amplified spectrum of the near-IR OPA 32
3.3 The FROG trace and reconstructed temporal profile of the compressed near-IR pulse 34
3.4 Phase matching angle of the BBO crystal 35
3.5 A photograph of a non-collinear optical parametric amplifier 36
3.6 Various spectra produced by the visible NOPA 36
3.7 Intensity autocorrelation of the visible NOPA pulse. 38
3.8 The experimental setup used to generated the first femtosecond bunches of electrons from the slicing technique. 40
3.9 Raman scattering by of light by phonons 44
3.10 DECP mechanism for coherent phonon generation 45

4.1 A representation of the BEDT-TTF F_2TCNQ crystal structure 51
4.2 The reflectivity and imaginary part of the refractive index for ET-F_2TCNQ . 52
4.3 Optical setup for the ET-F_2TCNQ experiments 53
4.4 Intensity dependence of the change in reflectivity at the Mott gap. 56
4.5 Threshold and saturation plots of Mott-insulator to metal photo-induced phase transition. 57
4.6 Transient change in reflectivity at the Mott transition 58
4.7 Transient response of the Mott gap 59

4.8 Transient reflectivity spectra of the Mott gap 60
4.9 Normalized change in reflectivity 61
4.10 The reflectivity and other optical properties of ET-F_2TCNQ 63
4.11 Time dependent fitting of the reflectivity 65
4.12 Time evolution of the Mott gap peak and the excited-state peak. 66
4.13 The optical conductivity of the Mott gap: simulation and experiment 69
4.14 The time dependence of the probabilities of state ρ. 70

5.1 The orbital, structural and magnetic ordering in $LaMnO_3$ 74
5.2 The dielectric function of $LaMnO_3$ 75
5.3 The optical spectra of the pump and probe beams 76
5.4 Cross correlation between pump and probe 77
5.5 Sketch of experimental layout of the pump probe experiment in $LaMnO_3$ . . 78
5.6 Pump-probe changes in reflectivity in $LaMnO_3$ 79
5.7 The temperature dependance of the electron-phonon thermalization. 80
5.8 The coherent oscillations in the transient reflectivity in $LaMnO_3$. 81
5.9 Fourier transform of the residual oscillations in $LaMnO_3$ 81
5.10 Ionic motions associated with the normal-mode displacements observed in the transient reflectivity of $LaMnO_3$. 82
5.11 The temperature dependence of the amplitude of the phonon modes. 83
5.12 A comparison between the change in absorption at 1.9 eV and the change in the amplitude of the coherent lattice vibration as a function of temperature. . 84
5.13 Damping rates of the lattice vibrations as a function of temperature. 85
5.14 The excited state of $LaMnO_3$ after a charge transfer excitation within the *ab*-plane 88
5.15 The response of a semicovalent bond due to a change in exchange constant . 89

6.1 The fluence dependence of the voltage drop across the load resister after photo-excitation of $Pr_{0.7}Ca_{0.3}MnO_3$. 94
6.2 The transient change in reflectivity of $Pr_{0.7}Ca_{0.3}MnO_3$ at 77 K 96
6.3 The reflectivity spectra and fluence dependence of the pump-probe signal in $Pr_{0.7}Ca_{0.3}MnO_3$ at at 77 K. 97
6.4 The Fourier transform of the low frequency oscillations 97
6.5 Heavily damped Jahn-Teller phonons in $Pr_{0.3}Ca_{0.7}MnO_3$ 99
6.6 The transient change in $Pr_{0.7}Ca_{0.3}MnO_3$ at room temperature 100
6.7 High temporal resolution transient change in reflectivity of $Pr_{0.7}Ca_{0.3}MnO_3$ at room temperature 101

7.1 Schematic of a transitions probed by XANES spectroscopy. 106
7.2 The oxygen and manganese XANES spectra measured in total electron yield. 107

7.3 The XANES spectra of $Pr_{0.7}Sr_{0.3}MnO_3$ and $Nd_{0.7}Ca_{0.3}MnO_3$. 108
7.4 Manganese $3d$ energy level diagram in $Pr_{0.7}Sr_{0.3}MnO_3$ in the room temperature insulating and low temperature metallic state 110
7.5 Biasing circuit for the channeltron detector. 111
7.6 Schematic of the experimental setup for the time resolved XANES measurements 112
7.7 Time resolved changes in the XANES signal and the oxygen K-edge and manganese L-edge 114

8.1 The dispersion relation for light propagation near an IR active resonance . . 122
8.2 High temperature paraelectric and low temperature ferroelectric phases of $LiTaO_3$. 125
8.3 A sub unit of the $LiTaO_3$ showing the low frequency A_1 and E modes. 125
8.4 The Laue diffraction pattern from $LaTiO_3$. 127
8.5 A sketch of the slicing experiment used to measure phonon-polaritons with femtosecond X-rays. 129
8.6 Time dependence of the (006) diffraction peak. 130
8.7 The discretization of the electromagnetic field using a Yee cell. 132
8.8 The control sequence for the evolution of equations 8.22-8.25. 134
8.9 A snapshot of the simulation performed on a coarse grid size. 136
8.10 An expanded view of the simulation. 136
8.11 High resolution simulation of the c-axis component of phonon-polariton field at the surface of $LiTaO_3$. 137
8.12 An illustration of the difference between the simulation time and the pump probe time delay. 139
8.13 The time dependent fit of the fractional change in 006 diffraction intensity to the experimentally measured quantity. 140

Chapter 1

Introduction

1.1 Ultrafast science

Recording a dynamical event requires a method of capturing a series of 'snapshots' of the evolving system at several points in time. Each snapshot records the average state of the system during the exposure time. If the system changes whilst the snapshot is being recorded, the dynamics are blurred and information is lost. Therefore, in order to capture a fast dynamical event, snapshots need to be recorded on a timescale much sorted than that over-which the event occurs.

One of the earliest reported time-resolved measurement was performed by Muybridge in 1878 in order to settle the then much debated question of whether or not there is a time, when a horse is galloping, at which all four of the horses hooves are off the ground [1]. Muybridge used 12 cameras to take a series of photographs of a horse as it travelled. The cameras were configured to take photographs sequentially after the horse triggered a tripwire. Muybridge developed a high speed shutter that enabled each photograph to be recorded within a millisecond. During this exposure time a horse, galloping at 30 miles per hour, will move 1 cm. The images Muybridge took are reproduced in figure 1.1. The images are clear and show that there is a time when all four of the horses hooves are off the ground during the gallop, settling the debate.

Time-resolved science uses similar concepts to study physical, chemical and biological processes. In 1967 the Nobel prize in chemistry was awarded to Eigen, Norrish and Porter

'for their studies of extremely fast chemical reactions, effected by disturbing

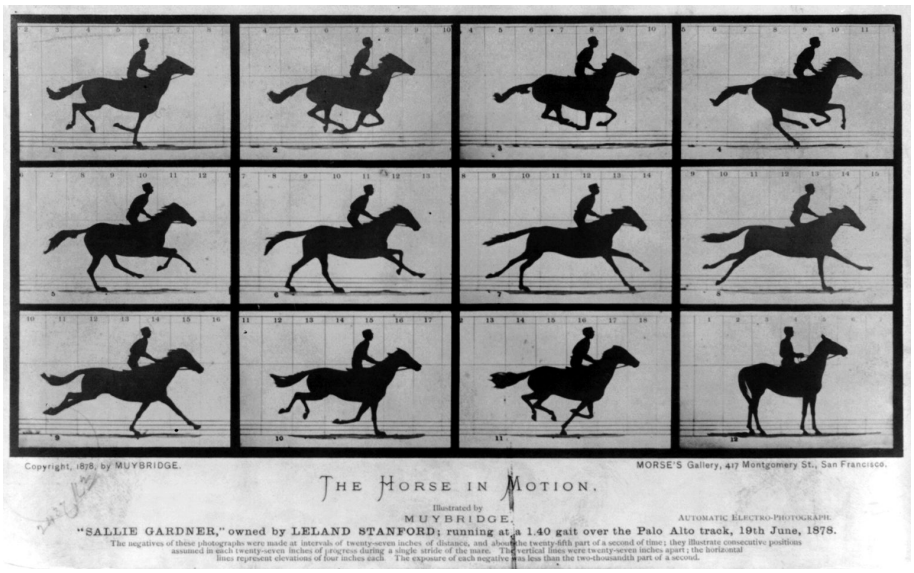

Figure 1.1: 'The Horse in Motion' by Eadweard Muybridge. The first time resolved measurement consisting of a series of images of a horse in motion. The measurement was used to prove that all four of a horse's hooves leave the ground at the same time during a gallop.

> *the equlibrium by means of very short pulses of energy'* [2].

Their studies of fast chemical reactions extended observable timescales from microsecond (10^{-6} seconds) to nanosecond (10^{-9} seconds) timescales. The development of the femtosecond laser [3] enabled the measurement of atomic rearrangements and 'transitional states' in chemical reactions. In 1999 Zewail was awarded the Nobel prize in chemistry

> *'for his studies of the transition states of chemical reactions using femtosecond spectroscopy'* [2].

By using ultrashort pulses of laser light, Zewail was able to record chemical reactions that occurred on a picosecond (10^{-12} seconds) to femtosecond (10^{-15} seconds) timescale.

In addition to chemical reactions, the ultrafast dynamics that occur in solid-state systems can be measured with similar techniques. The long-range order and cooperative behavior found in condensed phases gives rise to many interesting effects which occur on a femtosecond timescale. Furthermore, non-equilibrium phenomena, particularly important in materials driven into metastable or unstable states, are accessible with ultrafast probes. Effects that can be observed include electronic and lattice decoherence, scattering, thermalization and coupling between quasi-particles, and photo-induced phase transitions.

The current technological frontiers in ultrafast science are twofold. One direction is the continued development of faster probes, pushing the temporal resolution of measurements into the attosecond regime (10^{-18}s) [4], enabling the measurement of rapid electronic processes [5]. Another direction pursued is extending established static techniques, such as X-ray and electron diffraction, X-ray spectroscopy and photoemission, to the femtosecond timescale [6–10]. This enables different properties of the system, such as atomic positions and Fermi-surfaces, to be measured on the ultrafast time scale.

This thesis applies multiple probing techniques to study the photo-induced dynamics of complex materials, a class of materials with many interesting and unusual properties. The experiments reported here make use of probes covering a wide range of wavelengths, from the infrared to hard X-rays. The measured dynamics are amongst the fastest observed in many of the materials, capturing atomic, and in some cases electronic, dynamics on their elementary timescale, revealing the physics of Mott insulators, colossal magnetoresistive manganites and ferroelectrics.

1.2 Strongly correlated electron materials

Strongly correlated electron materials are those in which the Coulomb interactions between electrons is comparable to, or stronger than, the energy bandwidth of the individual electrons. In conventional band theory, which describes many materials very well, the energy bandwidth of an electron is a measure of how easily it can move through a crystal. If the Coulomb interaction between electrons is large, it restricts their motion so that the electrons cannot move independently. This results in material properties which can be vastly different to the conventional band picture.

1.2.1 Band theory

Basic band structure calculations can describe the insulating, metallic or semi-conducting properties of un-correlated materials very well. Bands, formed from a linear combination of the atomic orbitals, within the symmetry of the lattice, are constructed by ignoring the effects of electron-electron interactions. This approximation allows each electron to be treated independently. Each band can support a finite number of electrons and the bands are sepa-

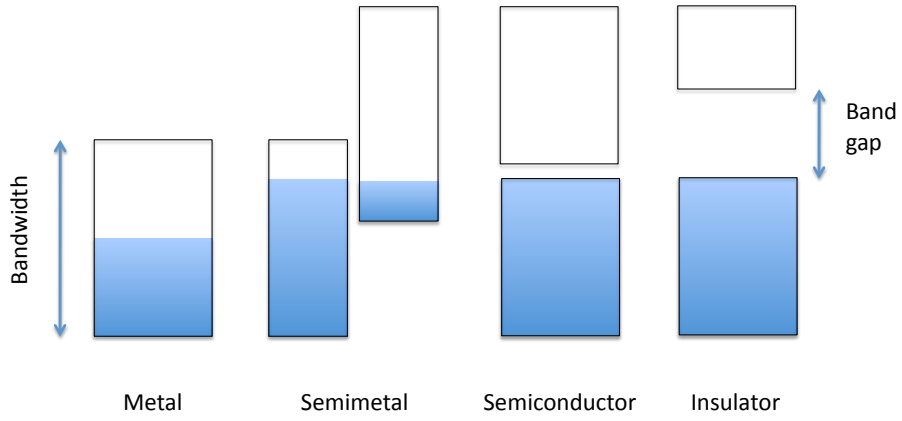

Figure 1.2: Band structure diagrams for metals, semimetals, semiconductors, and insulators

rated by an energy gap. The properties of a material are dictated by how many electrons are contributed to the band and the energy gap separating them. The band structure diagrams for metals, semimetals, semiconductors and insulators are shown in figure 1.2. If a band is full, a finite amount of energy is required to excite a charge and the material cannot respond to DC or low frequency electric fields. This type of material is an insulator. If, instead, some band states are unoccupied, electrons can easily move into them, allowing the material to respond to DC and low frequency electric fields. These materials are conductors. The lack of correlations between electrons ensures that the properties of the band, and the band gap, are independent of the band filling.

1.2.2 The Peierls distortion

Some metals, even in the absence of correlations, experience phase transitions to insulating states when cooled. One of the simplest examples of such a insulator-metal transition in the one dimensional Peierls effect.

Peierls showed that a half-filled 1D metal is unstable against a structural distortion transforming the metal into an insulator [11]. The electronic dispersion relation for a half-filled band is shown in figure 1.3a. The independent electrons occupy half of the available k states up to the Fermi-surface and the material is conducting.

However, if the material distorts, forming dimerized pairs as shown in figure 1.3b, the period of the lattice will double to contain two of the previous lattice points. The doubling

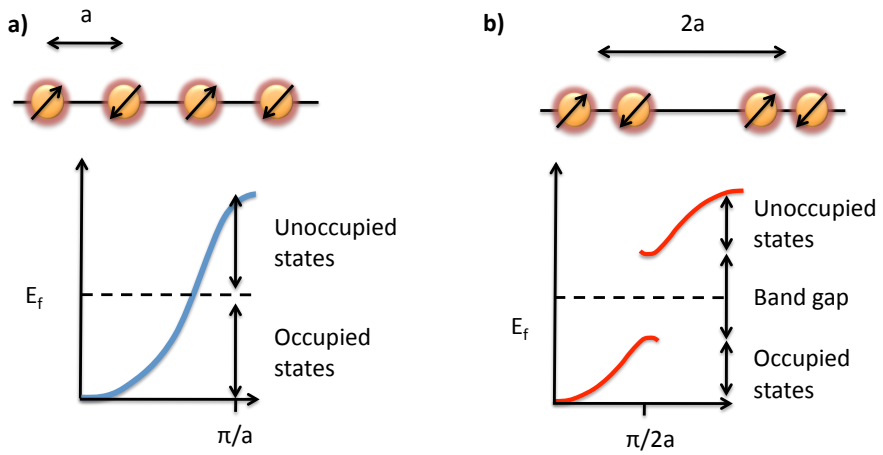

Figure 1.3: The Peierls transition. a. The dispersion relation for electrons in a periodic lattice, with lattice constant a. When the band is half-full, the Fermi-level resides half-way up the band and the material is a metal. b. If the lattice distorts, doubling the unit cell, the Brillouin zone halves. Now the Fermi level resides in a gap and the material is insulating.

of the lattice period corresponds to a halving of the Brillouin zone. This opens a gap at the Fermi-surface causing the material to become an insulator. Peierls showed that, for a one-dimensional material, the reduction in energy for the electrons at the Fermi-surface would be larger than the increase in elastic energy required to cause the distortion.

In materials with higher dimensionality, the long range Peierls distortion may not occur. However, the lattice can still couple to the electrons to form polarons. A polaron is formed when the electric field of the electron distorts the surrounding crystal lattice. As an electron moves through the crystal, the distortion travels with it, reducing the bandwidth of the electron and modifying the conducting properties of the material.

1.2.3 Correlation effects

When the band model is applied to materials that have strong electronic correlations the predicted properties can be vastly different to what is observed. This was first pointed out by Boer and Verwey [12], who noticed that many compounds consisting of transition metals with only partially filled d-levels turned out to be insulators instead of metals. For example, NiO has a full oxygen $2p$ level but an incomplete Ni $3d$ level. According to the band model, NiO would be metallic, however, it is an insulator with a large, 4.3 eV, band gap.

Wigner was amongst the first to point out the the importance of the Coulomb interaction between electrons and its impact on conductivity [13]. Wigner showed that, electrons in a uniform positive background would form a crystal at sufficiently low densities in order to maximize their mutual separation.

Mott investigated the effects of Coulomb screening on free carriers [14]. When an electron moves from one atom to another, it leaves behind a positive hole. The hole will have an attractive force on the electron with the potential to form a bound state. However, the presence of other electron-hole pairs will screen the electric field, reducing the range of the attractive interaction from the unscreened $U \propto -e^2/r$ to $U_s \propto -(e^2/r)\exp(-qr)$, where e is the charge of the electron, r is the electron hole separation and q is a screening factor which is dependent on the electron density, N.

When U_s no-longer exhibits bound sates, electrons are free to move throughout the crystal and the material will be metallic. Mott found that this occurred when [15]

$$N^{1/3}a_H \approx 0.2, \tag{1.1}$$

where a_H is the Bohr radius which demonstrates that there is a critical electronic density for the insulator-metal transition. As a result, Mott insulators should become metallic under compression, due to an increase in the electron density and metals should become insulating under tension due to the decrease in electron density. Mott transitions can be observed in semiconductors where a critical density of dopants is required before the material becomes metallic.

In the cases described by Wigner and Mott, the interactions between electrons correlates their behavior and play an important role in dictating the electronic properties of the system.

1.2.4 Control of materials

The competition between the single electron bandwidth, W, and the electron-electron Coulomb interaction, U, dictates the ground state properties of a material. If $W > U$, electrons can overcome their mutual repulsion and can move freely throughout the material. If $U > W$, the Coulomb repulsion dominates, localizing charge on atomic sites. These properties can combine with other correlation effects, such as electron-lattice coupling, which adds additional complexity to the system. When several couplings act on similar energy scales, they compete to dictate the ground state properties of the material in a complex way.

By changing the relative strengths of the couplings, many different phases can be achieved. For example, electron-phonon coupling, as well as reducing the electron bandwidth, can modify the Coulomb repulsion to provide an attractive interaction between electrons. The attractive interaction is the force behind the formation of Cooper pairs and is responsible for conventional superconductivity. Understanding the coupling between electrons, lattice, spin and orbital degrees of freedom is vital for determining the properties which give rise to high temperature superconductivity as well as the many other phases that arise in complex correlated materials.

The properties of complex materials can be controlled, to some degree, by chemical doping. Doping can be used to change the relative strengths of each couplings and promote certain characteristics. Doping can also change the number of valence electrons present in the material. Correlated materials are particularly sensitive to the number of valence electrons available. By substituting ions with a higher or lower valency, the properties can change dramatically and a filling controlled phase transition ensues [16]. The complexity found in many correlated materials gives rise to a large number of phases with vastly different properties. The different phases can be separated by relatively small energy differences and can result in phase transitions to states with completely different properties with only a small external perturbation.

1.3 Photo-induced phase transitions

The effects of photo-excitation on materials can range from exciting carriers across a band gap to inducing phase transitions. Shank et al. were amongst the first to use femtosecond pulses to study early timescale dynamics in photo-excited semi-conductors [17].

The first ultrafast phase transition observed was the laser induced solid-to-liquid phase change in highly excited semi-conductors [18]. These measurements were followed by time-resolved diffraction measurements to observe the change in atomic positions associated with the phase transition on an ultrafast timescale [19].

The properties of correlated materials can be changed by photo-excitation in ways similar to those induced by chemical doping. Koshihara et al. were amongst the first to investigate the photo-induced neutral-ionic phase transition in TTF-CA crystals induced by continuous-wave lasers [20]. Experiments to observe other ultrafast, solid-solid, phase transitions were

performed, almost two decades after the first ultrafast melting experiments, in Peierls distorted materials. By removing electrons from the valence band, the structural distortion can become unstable and the crystal structure relaxes. This has been observed using ultrafast X-ray probes in VO_2 [21] and Bismuth [22].

Excitation of correlated materials often results in large changes in the optical properties [23] and can lead to the creation of metallic states [24] on an ultrafast timescale. The similarity of the effects achieved by photo-excitation to chemical doping has led to the process being described as 'photodoping', where control of the materials properties is achieved with light [25].

Interest in the excited state of correlated materials has led to the development of new ultrafast probes. Cavalleri et al. used femtosecond soft X-rays to measure time resolved near edge X-ray absorption structure spectroscopy on the ultrafast timescale in VO_2 [26]. In addition to X-ray diffraction techniques, short pulse electron diffraction is an emerging new field [7, 8]. Recently, Perfetti et al. used laser based time resolved photoemission spectroscopy to measure the formation of the metallic state and the change in the Fermi surface of the charge-density wave solid TaS_2 [10].

New strategies for exciting materials are also being devloped. By using intense pulses in the mid-IR Rini et al. [27] were able to excite a specific phonon mode in a manganite in order to induce the insulator-metal phase transition. This excitation mechanism showed that a photo-induced phase transition can occur without exciting electrons and is, presumably, due to a structurally induced change in electronic-bandwidth.

1.3.1 Probing materials on their fundamental timescale

The Heisenberg uncertainty principle relates the energy scale of a process to a time over which it occurs as,

$$\Delta E \Delta t \geq \frac{\hbar}{2}. \tag{1.2}$$

In order to investigate how a system fundamentally responds to a prompt excitation, pulses with a duration of $\Delta t \approx \frac{\hbar}{2\Delta E}$ need to be used, where ΔE is the energy scale of the phenomena investigated. For chemical reaction that occur at room temperature with an energy scale of $\sim k_B T$, the time scale is $\Delta t > 10\,\text{fs}$, which is close to the timescales of $\sim$100 fs seen in femtochemistry.

The timescale on which a material melts is dictated by the heat diffusion coefficient as this describes the rate at which energy can be transfered into the crystalline solid. Exciting a material with a laser initially results in the excitation of electrons. The electrons rapidly thermalize to a higher temperature than the lattice. The electrons and the lattice thermalize on a time scale dictated by their coupling, usually several picosecond. By exciting and probing materials with a pulse much shorter than the electron-lattice thermalization time non-thermal melting was observed in which the liquid state of the material is formed before the electrons have had time to transfered their energy to the lattice [18, 19].

In complex materials, timescales which control the dynamics can be dictated by the electronic excitations, with an energy scale set by U and W [28], magnetic interactions, which occur on timescales set by the integral J, or the lattice response, which is dictated by phonon energies.

By measuring on a ultrafast timescale, Cavalleri et al. could determine the driving force behind the metal-insulator phase transition in VO_2 [29]. At high temperatures VO_2 is metallic. On cooling below 340 K, VO_2 undergoes a phase transition to an insulating state, together with a structural distortion which doubles the unit cell. It was known that electron-electron interactions had a significant impact on the physical properties of VO_2, however, it was unclear whether the insulator-metal phase transition was a direct result of the structural distortion [30], or if the structural transition was the byproduct of an insulating state induced by the electron-electron interactions [31].

As VO_2 exhibits a photo-induced insulator-metal phase transition, Cavalleri could measure the timescale on which the process occured. It was observed that, despite prompt photo-excitation, an 80 fs delay was found for the formation of the metallic state. This time scale could be related to a phonon mode of the system, suggesting that the structure properties dictated the electronic state more than the electron correlations.

Many complex materials have similar questions surrounding the nature of their ground state. The origin of the energy gap of high-temperature superconductivity, found in the cuperates and pnictides, is controversial, with electronic, phonon and spin components all believed to play a critical role in determining its nature. The ground state of the manganites is also dictated by similar degrees of freedom. By looking at the timescale on which gaps collapse and new states emerge after photo-excitation, information on the energy scales dictating the

correlation effects can be obtained.

The work performed in this thesis probes the photo-induced dynamics in Mott insulators, manganites and ferroelectrics, with some of the shortest pulses available in order to reveal the timescales and elementary processes these materials experience as they evolve into, and out of non-equilibrium states.

Chapter 2

Strong correlations and complex manganites

This chapter expands upon the ideas of correlations and complexity introduced in chapter 1. In particular it discusses the physics of the Mott-Hubbard model which underpins many of the concepts of strongly correlated electron materials. The second half of this chapter is dedicated to the manganites, a collection of materials whose properties are strongly influenced by correlation effects. Manganites are particularly susceptible to photo-excitation and the induced change in the materials properties are investigated in chapters 5-7.

2.1 Mott insulators

One of the key theoretical concepts used to study complex materials is the Mott-Hubbard model. By only considering interactions between electrons situated at the same lattice site, Hubbard recast the ideas of Mott into the mathematics of second-quantisation to give the Mott-Hubbard hamiltonian [32],

$$H = -t \sum_{<i,j>,\sigma} (c^{\dagger}_{i,\sigma} c_{j,\sigma} + H.c) + U \sum_{i} n_{i\uparrow} n_{i\downarrow}. \tag{2.1}$$

The first term comes from the tight binding model and corresponds to the kinetic energy of the electrons. $c^{\dagger}_{i,\sigma}$ is the creation operator for an electron at site i with spin $\sigma = \uparrow, \downarrow$ and t is the transfer integral for electrons between neighbouring sites. Larger values of t make it easier for electrons to 'hop' between sites. The value of t is arrived at by considering the

overlap of onsite electronic wavefunctions connected by the potential generated by the lattice and, therefore, depends on the separation of the atoms as well as the wavefunctions involved.

The second term, U, is the Coulomb interaction between two electrons. In order to reduce the complexity of the calculation, the interaction between electrons is often restricted to interactions between electrons that are situated on the same lattice site. In principle, U, can depend on the particular orbital occupied, however, in the example presented here, only one orbital with two spin states is considered. $n_{i\sigma} = c^{\dagger}_{i\sigma} c_{i\sigma}$ is the electron number operator for each spin state.

Equation 2.1 is in a simplified form of the general Hamiltonian as it only contains a single atomic orbital, it is isotropic, and the interactions are between nearest neighbours only. In the limit of $t \gg U$, the tight-binding model is retrieved and electrons are delocalized throughout the crystal with well defined k-vectors which form bands. However, in the opposite limit, $t \ll U$, the coulomb repulsion prevents electrons from moving onto occupied lattice sites which leads to charge localization. When the system is half-filled, i.e. when there is exactly one electron per lattice site, the system will be insulating.

As the filling is reduced/increased, the system will become metallic-like, as there are more vacant sites onto which electrons/holes can hop [16]. For transition metal ions with an occupation n of the d-levels, the hopping transitions will be of the type $d_i^n d_j^n \rightarrow d_i^{n-1} d_j^{n+1}$, i.e. the creation of an electron on site j and a hole on site i. The energy cost for this transition, U, can be measured by comparing the difference between the ionization energy, I, and the electron affinity, E, to give

$$U = I - E. \tag{2.2}$$

The Hubbard Hamiltonian results in the formation of a energy gaps, but these are now of electronic origin. In the limit of strong U, the energy splitting between the Mott levels, E_g, is given by,

$$E_g = U - W = U - 2nt, \tag{2.3}$$

where W is the bandwidth of the upper and lower Hubbard bands (UHB and LHB), and n is the number of nearest neighbours. However, in some materials the gap energy was significantly lower than expected, suggesting that the electron transfer was not between neighbouring transition metal ions, but between neighbouring cations and anions [33]. Such a transition can be represented as $d_i^n \rightarrow d^{n+1}\underline{L}$, where $\underline{L}$ corresponds to a hole in the anion valence band,

with the transfer process requiring Δ in energy. These systems, referred to as charge transfer insulators, can be considered as impurity doped semiconductors with the d-band acting as the impurity band and transport is due to holes in the oxygen band.

Figure 2.1 gives a schematic of the band structure for a Mott and charge transfer insulator when $U, \Delta \gg t$ and indicates the lowest energy transitions for each case. The dependence of the physical properties exhibited from the Mott-Hubbard model as a function of filling is one of the main areas of current theoretical investigation [16].

The physics of strong correlations and Mott insulating behaviour discussed above is of interest here for two reasons. Firstly, it underpins the physics of complexity in solids and is a necessary introduction to the discussion on manganites. Secondly, chapter 4 of this thesis is concerned with the photo-response of a quasi-one dimensional Mott Insulator, realized in the organic salt (BEDT-TTF)-F_2TCNQ.

2.2 The Manganites

The term 'manganites' refers to materials which contain either tetravalent or trivalent manganese ions [34]. They exhibit strong correlations between the charge, lattice, spin and orbital parameters. This gives rise to complex behaviour which results in a large variety of phases and interesting phenomena, which has sustained interest in these materials for the last 60 years.

One of the most remarkable phenomena found in the manganites is their response to magnetic fields. Usually, the electrical resistance of a material increases when it is in a magnetic field. This is because the magnetic field applies an extra force on the electron, causing it to deviate from the shortest path between two contacts. The increase in path length leads to more scattering and hence a higher measured resistivity. However, maganites behave in the opposite fashion, showing a negative magnetoresistance effect of up to 9-orders of magnitude [35]. The effect is so large that it was named the Colossal magnetoresistive effect (CMR) to distinguish it from the giant magneto-resistance effect.

Another area of interest is the change in the macroscopic properties of manganites induced by doping. By varying the ratio of tetravalent to trivalent manganese ions, many different phases can be accessed and a wide range of ordering phenomena have been observed. These include metallic and insulating ferromagnetic states as well as insulating anti-ferromagnetic,

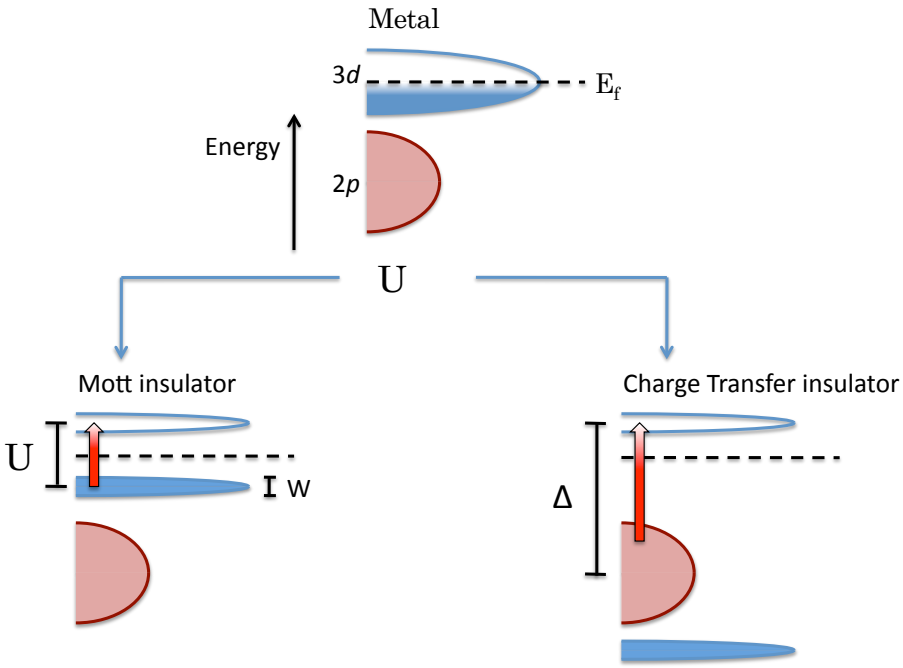

Figure 2.1: A band diagram of a transition metal compound, consisting of a partially full transition metal d-level and a full $2p$ anion band. When $t \gg U, \Delta$ the Hubbard bands are not split resulting in the fermi level lying in the middle of the d-band. When $U \gg t$ the $3d$ band is split into the upper and lower Hubbard bands resulting in an insulator. If $U < \Delta$ the material is a Mott insulator and excitations correspond to electrons and holes in the upper and lower Hubbard bands respectively. Whereas, if $U > \Delta$ the anion valence band lies closer to the fermi-level and excitations correspond to electrons in the upper Hubbard band and holes in the anion valence band. This type of material is a charge transfer insulator.

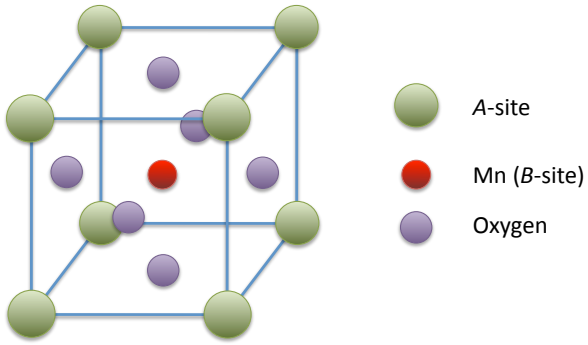

Figure 2.2: The ideal ABO_3 cubic perovskite crystal structure.

charge ordered, orbital ordered and long range cooperative Jahn-Teller distorted states. Most of the phases of manganites are 'unconventional' and poorly understood, and particularly unstable to small perturbations.

2.2.1 Crystallographic and electronic structure

Many manganites form an ABO_3 cubic perovskite crystal structure. Trivalent cations such as La^{3+}, Nd^{3+} or Pr^{3+} or divalent cations such as Ca^{2+} and Sr^{2+} occupy the A-sites at the corners of the cube unit cell. The $Mn^{3+/4+}$ ions occupy the B-site positions at the centre of the cube and the O^{2-} ions occupy the face-centre positions, forming an oxygen octahedra around the manganese ion. The unit cell of an ideal perovskite structure is shown in figure 2.2.

In this structure, the manganese ion experiences a cubic crystal-field generated by the surrounding oxygen octahedra. The cubic potential lifts the 5-fold degeneracy of the $3d$ manifold of an isolated Mn ion into a lower energy, 3-fold generate t_{2g} level and a 2-fold degenerate, higher energy, e_g level. The splitting, often referred to as $10Dq$, is typically 1-2 eV in the manganites [36] and a schematic of the energy level diagram is shown in figure 2.3.

Mn^{3+} ions have four electrons in the the $3d$ level. Due to a strong Hund's coupling between the spins, the Mn ion adopts a high-spin $t^3_{2g\uparrow}e_{g\uparrow}$ configuration. Such a configuration is unstable to a Jahn-Teller distortion of the crystal lattice [37]. The t_{2g} levels consist of the set of atomic wavefunctions d_{xy}, d_{yz} and d_{zx} and are shown in figure 2.3. These wavefunctions have a high probability for electrons to be located between the oxygen anions. The e_g levels consist of the $d_{3r^2-z^2}$ and $d_{x^2-y^2}$ atomic wavefunctions which point towards the oxygen anions. As the electrons and the oxygen ions are both negatively charged, the system can reduce its

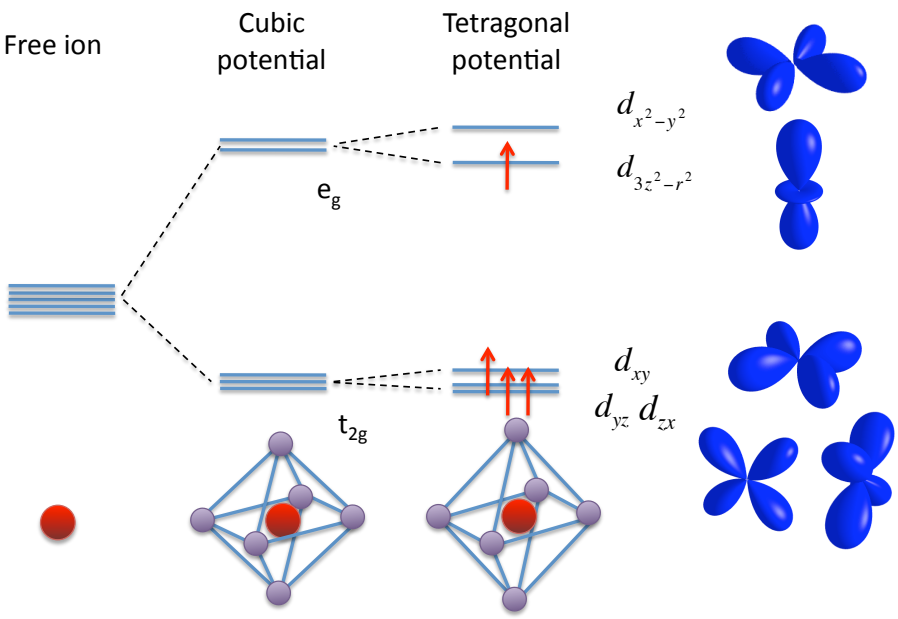

Figure 2.3: The electronic structure of the Mn ion within the crystal field.

total energy by distorting the crystal structure. If the distortion is along the z-direction, the distance between the oxygen ions and the electron in $d_{3r^2-z^2}$ level will be increased, decreasing the Coulomb energy between them at the expense of increasing the Coulomb energy between the electron in the $d_{x^2-y^2}$ level and the oxygen ions. For a Mn^{3+} ion the $d_{x^2-y^2}$ is un-occupied and the distortion is energetically favorable. However, the Mn^{4+} ion has no electrons in either the $d_{3r^2-z^2}$ or the $d_{x^2-y^2}$ levels and the distortion does not occur.

Manganites exhibit further deviations from the ideal perovskite structure and show $GdFeO_3$-like tilting of the oxygen octahedra. The amount of tilting depends on the radius of the A site ions with larger tilting occurring for smaller ions [38]. As a result the symmetry of many manganite crystals is further reduced from tetragonal to orthorhombic.

2.2.2 Properties of manganites

Perovskite manganites contain partially filled $3d$ levels which, due to strong correlation effects, are insulating with anti-ferromagnetic ordering at low temperatures. The interplay between the charge, orbital, spin and structural degrees of freedom results in a large number of macroscopically ordered phases. The robustness of each phase is particularly low and transitions to new phases have drastically different properties. This is a result of multiple phases all

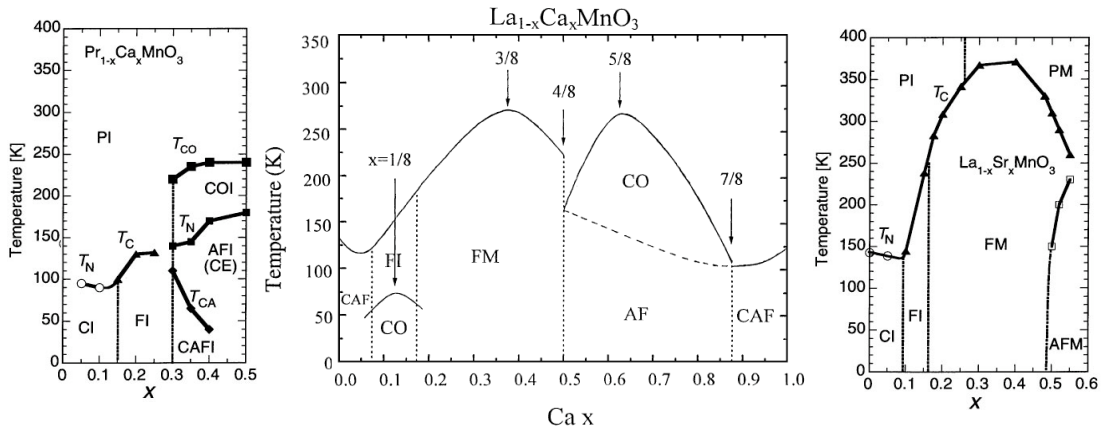

Figure 2.4: Phase diagrams for low ($Pr_{1-x}Ca_xMnO_3$) [39], intermediate ($La_{1-x}Ca_xMnO_3$) [36] and high bandwidth ($La_{1-x}Sr_xMnO_3$) [39] manganites. P- paramagnetic, F - ferromagnetic, AF - antiferromagnetic, I - insulator, M - metal, CO - charge ordered, CAF - canted anti-ferromagnetic

of which have similar free energies. As a result, several manganites show evidence of phase co-existence on nanometer length scales [36].

Chemical substitution can control the electronic population in the e_g levels, reducing the effects of the electron-electron interactions by adding holes to the system. Pressure can affect the crystal structure and modify the electronic bandwidth, or hopping parameter t, whilst magnetic fields can modify the preferred spin orientation and the conductivity of the material. Slight changes in these parameters can often lead to drastically different macroscopic properties and often result in transitions from insulating to metallic states.

Chemical substitution

Many properties of the manganites can be influenced by chemical doping. By changing the valency of the A-site ion the charge on the manganese ion can be controlled. Doped manganites are written in the form $A_{1-x}A'_xMnO_3$, consist of $(1-x)$ Mn^{3+} ions (4 electrons in the d level) and x Mn^{4+} (3 electrons in the d level).

The phase diagram for several manganites, with low, intermediate and high single electron bandwidths, are shown in figure 2.4. A large variety of phases with vastly different properties are achievable in the manganites, ranging from charge and orbitally ordered anti-ferromagnetic

insulators to ferromagnetic metals.

The conductive properties of the manganites are intricately related to their magnetic state. This was initially explained by Zenner, who suggested the 'double-exchange' mechanism for mixed-valence manganites [40]. Zener considered two manganese ions of difference valency connected by an oxygen ion. The two possible configurations for the state are: ψ_1 =$Mn^{3+}O^{2-}Mn^{4+}$ and ψ_2 =$Mn^{4+}O^{2-}Mn^{3+}$. As these states are degenerate in energy, the ground state of the system should be a linear combination of ψ_1 and ψ_2 and the e_g electron is free to move between the two sites. However, as the spin of the e_g electron is preserved as it moves between sites, the ground state can only be achieved if the t_{2g}-spins are aligned. As a result, the conductive state is connected with the ferromagnetic ordering. The name 'double-exchange' arises from the mechanism by which electrons are transfered between sites as, in the Zener model, an electron is transfered from the Mn^{3+} to the oxygen ion at the same time an electron, with the same spin, is transfered from the oxygen ion to the manganese ion.

As well as introducing holes into the e_g levels, chemical substitution results in mismatch between the radii of the two different A-site ions. This introduces a strain into the material. Smaller A site ions cannot fully occupy their lattice positions and pull oxygen ions from their ideal face centred positions causing a change in the Mn-O-Mn bond angle and length. This changes the electronic bandwidth.

The change in bond angle is often expressed in terms of the tolerance factor, Γ, which is defined as,

$$\Gamma = \frac{d_{A-\mathrm{O}}}{\sqrt{2}d_{\mathrm{Mn-O}}}, \tag{2.4}$$

where $d_{A-\mathrm{O}}$ is the distance between the A site ion and the nearest oxygen ion and $d_{\mathrm{Mn-O}}$ is the distance between the Mn ion and the nearest oxygen ion. For an ideal, undistorted, perovskite, $\Gamma = 1$.

The tolerance factor is monotonically connected to the hopping amplitude, t, of the e_g electrons. The hopping amplitude is a function of Mn-Mn separation as well as Mn-O-Mn bond angle. Although reducing the bond angle from 180° reduces the Mn-Mn separation, the gain is more than offset by a reduction in the overlap between the Mn-3d and O-2p wavefunctions which are responsible for t. The overlap is at a maximum for a 180° bond, and reduces to zero for a 90° bond were the wavefunctions are orthogonal [41]. Therefore the larger the miss-match in ionic radii, the lower the hoping amplitude, or electronic bandwidth

becomes, increasing the tendency to become insulating.

Different values of the tolerance factor result in three general classifications of doped manganites, those with: low, intermediate and high electronic bandwidths.

I High-bandwidth: The A-site ionic radii are well matched resulting in only a small change in bandwidth due to doping. The prototypical compound is $La_{1-x}Sr_xMnO_3$. These materials are normally metallic and have Curie temperatures above room temperature.

II Intermediate-bandwidth: Doping reduces the bandwidth of the electrons. This reducing the Cure temperature to below room temperature and insulator to ferromagnetic-metal phase transitions occur on cooling. $La_{1-x}Ca_xMnO_3$ are intermediate bandwidth manganites

III Low-bandwidth: The ionic mismatch is at its largest which sufficiently reduces the bandwidth so that no metallic state is accessible at any temperature or doping. $Pr_{1-x}Ca_xMnO_3$ is a well-studied example.

Colossal Magneto Resistance in low-bandwith manganites

The control of the transport properties of manganites has driven a lot of research in these materials. Most doped manganites exhibit a magneto-resistance effect, which reduces electrical resistance when the material is in a magnetic field.

The reduction in resistivity is most striking in the low-bandwidth manganite $Pr_{1-x}Ca_xMnO_3$. This material shows insulating behaviour at all temperatures and doping concentrations. However, when the material is in a magnetic field, the phase can be switched from a charge ordered insulating state into a metallic state. At $x = 0.3$, $Pr_{0.7}Ca_{0.3}MnO_3$ is particularly susceptible and a 7 T magnetic field can reduce the resistivity by approximately 10 orders of magnitude [35]. This is of particular interest because a metallic phase cannot be obtained via changes in temperature or doping in the low-bandwidth manganite and suggests that there is a 'hidden' magnetic phase which competes with the charge-ordered anti-ferromagnetic phase.

Hwang et al. [42] showed that an insulator to metal phase transition can also be achieved by compressing the same material. Again, the charge ordered insulating state, became a metallic state under the application of 10 kbar. In order to show that the two methods share a common origin, Hwang et al. also showed that the pressure required to induce the insulator-

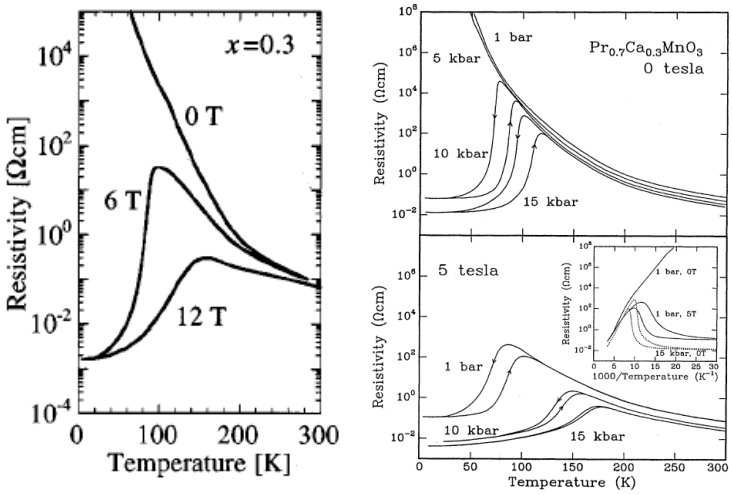

Figure 2.5: Left: Changes in resistivity as a function of temperature and magnetic field, reproduced from [35] . Right: Changes in resistivity as a function of pressure and temperature and magnetic field from [42]. Both measurements are taken on $Pr_{0.7}Ca_{0.3}MnO_3$.

metal phase transition was reduced when the material was in a magnetic field. These results are have been reproduced in figure 2.5 and these experiments demonstrate the importance and the strength of the complex coupling between the multiple degrees of freedom of the manganites.

The competition between charge-ordered anti-ferromagnetic state and the metallic state can also be switched by the application of electric fields [43] and by exposure to hard X-rays [44], both of which directly effect the charge sector of the material.

The manganites are of particular interest to ultrafast science as it has been shown that the insulator-metal phase transition can also be triggered by laser excitation [24] allowing the possibility of ultrafast control of the materials properties. Again, this transition is associated with a disruption of the charge-ordered state. However, recently it has been shown that this is not the only way to induce the phase transition dynamically. By using mid-IR light, IR-active phonon modes can be resonantly excited, and can also cause the phase transition [27, 45]. The dynamics of the photo-induced phase transitions will be discussed in more detail in chapter 6.

2.2.3 Models for the manganites

Goodenough-Kanamori rules

The Goodenough-Kanamori rules* can be used to explain the crystallographic, charge and orbital structure of many transition metal compounds [46]. The rules dictate the sign of the super-exchange interaction between cations that are bridged by oxygen anions and relate bond lengths to the type of bonding between the ions.

Goodenough coined the term 'semicovalent-bonding' in order to describe the bonds formed in transition metal compounds. The bonding in these compounds comes from the hybridization of the fully occupied oxygen $2p$-orbitals with the incomplete d-orbitals of the transition metal ion. Transition metal ions have strong Hund's coupling which prefers electronic configurations that maximize the spin state. Relative to the transition metal ion's spin, the oxygen $2p$-level can donate one spin which is aligned and another that is anti-aligned. Goodenough argued that the $2p$-electron with the aligned spin will spend more time on the transition metal ion than the electron with the anti-aligned spin. The resulting bond is then predominately formed with a single spin and is referred to a semicovalent bond.

This mechanism results in three types of bonding between two manganese ions that are connected by an oxygen ion. The length of each bond is dictated by the bonding strength.

I A fully covalent bond can form between two Mn ions if their spins align anti-ferromagnetically. This bond forms because each oxygen spin can reside next to an ion with an aligned spin, resulting in a strong bond and a short bond length.

II If the manganese ions are aligned ferromagnetically, a strong bond can only form between the oxygen and one of the neighbouring manganese ions. The second electron from the oxygen will be excluded from the anti-aligned manganese ion, resulting in the formation of a 'semi-covalent' bond that is weaker than the covalent bond and will have a larger bond length.

III If the manganese ions are not aligned, the oxygen electrons cannot form a strong bond with either of the manganese ions and the bonding will be predominantly ionic in nature resulting in the weakest of the three bonds and, therefore, the longest.

*These rules can also be referred to as the Goodenough-Kanamori-Anderson (GKA) rules.

Kanamori put the Goodenough rules on a more mathematical basis by considering the symmetry of the hybridized states [41]. The combined results can be used to predict the sign of the exchange integral, J, based on the occupancy of the manganese orbitals involved in the bonding. The rules can be summarized as follows:

- The exchange integral will be negative, i.e. prefer anti-ferromagnetic alignment, if a bond is formed between two half-filled orbitals or between two empty orbitals.
- The exchange integral will be positive, i.e. prefer ferromagnetic alignment, if the bond is between a half-filled orbital and an empty orbital or between a filled orbital and a half-filled orbital.

Single-orbital model

The manganites are complex materials, the physics of which cannot be fully captured by simple models. On the contrary to the early proposals by Goodenough, most of the later developments have focused on the electronic properties, rather than the bonding properties of the manganites. A general, but difficult to solve, Hamiltonian, which is believed to contain all the necessary physics of the manganites can be written as

$$H = H_t + H_{\mathrm{U}} + H_{\mathrm{H}} + H_{\mathrm{JT}} + H_{\mathrm{AF}}, \tag{2.5}$$

where H_t is the kinetic energy of the electrons, H_{U} is the electron-electron interaction, H_{H} is the Hund's coupling term between the spins of the e_g and t_{2g} levels on a manganese site, H_{JT} is the Jahn-Teller coupling between electrons and phonons and H_{AF} is the anti-ferromagnetic superexchange interaction between t_{2g} spins. The above Hamiltonian requires further approximations with regards to the nature and relative strengths of each term in order to be solvable. Most strategies start by reducing the complexity of the problem by only considering electron motion between the e_g levels. The electrons in the t_{2g} levels are treated as a localized, classical, spin-$\frac{3}{2}$ system, on top of which the e_g electrons move and interact.

If the Jahn-Teller distortion is considered large and static, the Hamiltonian can be considerably simplified by assuming that only the lower energy of the two e_g orbitals plays a role in the physics. In addition, although the electron-electron interaction energy is considered to be the largest term in the Hamiltonian it can be incorporated into the Hund's (H_{H}) term as, if there are two electrons on one site, one will have to have the opposite spin to the t_{2g} levels.

This electron will have to pay an energy penalty, J_{H}, in the same way two electrons would have to pay an energy U for double occupancy when electron-electron interactions are taken into account.

The reduced Hamiltonian can be simplified to

$$H = -\sum_{<i,j>,\sigma} t_{ij}(c^{\dagger}_{i,\sigma}c_{j,\sigma} + H.c.) - J_{\mathrm{H}} \sum_{<i,j>,\sigma} \boldsymbol{s}_i \cdot \boldsymbol{S}_i + J_{\mathrm{AF}} \sum_{<i,j>} \boldsymbol{S}_i \cdot \boldsymbol{S}_j, \tag{2.6}$$

with the remaining terms of the Hamiltonian written out explicitly. $c^{\dagger}_{i,\sigma}$ is the creation of an electron at a lattice site i with a spin σ projected along the z-axis and t_{ij} hopping amplitude of the electrons between sites and provides the kinetic energy. $\boldsymbol{s}$ is the spin state of the e_g electron and $\boldsymbol{S}$ is the classical spin of the combined t_{2g} electrons. All summations are taken over nearest neighbours only for simplicity.

Although this model fails to predict many of the properties of the manganites, it still provides a useful picture of the manganites. In particular, it explains how the metallic state and ferromagnetic alignment are connected.

The e_g electron spin aligns to that of the on site t_{2g} spin and defines a local z-direction. A spin-$\frac{1}{2}$ electron in the $x - z$ plane can be represented, in terms of the eigenvalues of the Pauli σ_z matrix, as

$$\boldsymbol{s} = \begin{pmatrix} \cos(\frac{\theta}{2}) \\ \sin(\frac{\theta}{2}) \end{pmatrix}, \tag{2.7}$$

where θ is the angle the spin makes with the z-axis.

Rotations of the spin are performed by applying the transformation

$$R = \begin{pmatrix} \cos(\frac{\theta}{2}) & \sin(\frac{\theta}{2}) \\ -\sin(\frac{\theta}{2}) & \cos(\frac{\theta}{2}) \end{pmatrix}. \tag{2.8}$$

Therefore, if the t_{2g} spin state at site 1 defines the global z-direction, the kinetic energy term can be re-written as,

$$H_t = -t(c^{\dagger}_{1,\uparrow}c_{2,\uparrow} + H.c.) = -t\cos(\frac{\theta}{2})(c^{\dagger}_{1,\uparrow}c'_{2,\uparrow} + H.c.). \tag{2.9}$$

Here the annihilation operator, $c_{2,\uparrow}$, which annihilates a spin up electron with respect to the global z direction, has been replaced by the operator c' which annihilates an electron with a spin projected along the direction defined by the local t_{2g} electrons, with $c_{2,\uparrow} =$

$R^{-1}c' = \cos(\frac{\theta}{2})c'_{2,\uparrow} - \sin(\frac{\theta}{2})c'_{2,\downarrow}$. The spin-down term has been dropped because the anti-aligned spin state is energetically unfavorable due to the large Hund's energy. As a result, an effective hopping energy $t_{\text{eff}} = t\cos(\frac{\theta}{2})$ arrises which is zero when the t_{2g} spins are anti-ferromagnetically aligned and is large when the spins are ferromagnetically aligned. Therefore, if $t > J_{AF}$ the system will be a ferromagnetic metal, however, if $t < J_{AF}$, the material will be an anti-ferromagnetic insulator.

This model gives a complete quantum mechanical description of the double exchange mechanism introduced by Zener and goes some way to explain how applying a magnetic field, which effects t_{eff} or applying pressure, which effects t, can trigger an insulator-metal phase transition. However, it cannot explain the observed ferromagnetic insulating states, or the anti-ferromagnetic metallic states found in some manganites and does not provide good quantitative solutions to the CMR effect.

The reason why manganites are so difficult to model is that each term in equation 2.5 competes on a similar energy scale so that they cannot be treated as successive perturbations. As a result, more terms are required in the models, and the complexity of the problem increases dramatically. Many of the interesting states of the manganites, such as the charge and orbitally ordered states require two orbital models before any long range ordering is possible, yet a reasonable quantitative theoretical description is still lacking.

Orbital ordering and orbitons

Charge and orbital ordering is a natural consequence of the Goodenough-Kanamori rules. Often, a long-range cooperative Jahn-Teller distortion will remove the degeneracy of the e_g levels and promote a specific orbital and orientation. The resulting orbital ordering plays a vital role in determining the subsequent magnetic ordering of the system (see chapter 5).

However, orbital ordering does not require coupling between the structure and the orbital and is a natural consequence of orbital degeneracy. This was first shown in Hamiltonian proposed by Kugel and Khomskii [47]. The model considers two degenerate e_g orbitals, represented as the components of a pesudo-spin-$\frac{1}{2}$ particle, τ, with eigenstates $|x\rangle = d_{x^2-y^2}$ and $|z\rangle = d_{3z^2-r^2}$. The model was used to predict that orbital ordering occurs in K_2CuF_4 [48].

Khaliullin and Oudovenko [49] recast the Hamilton of Kugel and Khomski into the form,

$$H = \sum_{\langle i,j \rangle} \hat{J}_{\alpha}^{ij} \left(\boldsymbol{S_i S_j} + \frac{1}{4} \right). \tag{2.10}$$

Where $\hat{J}$ is the exchange 'operator' applied between sites i and j along the crystallographic direction α. $\hat{J}$ is a function of the orbital operator $\hat{\tau}$. This form of the magnetic Hamiltonian shows that the exchange 'constant' experienced between spins is a function of the surrounding orbital order and connects the magnetic state to the orbital state.

Charge and orbital ordering has been observed in many manganites by resonant X-ray diffraction [50–54]. In these measurements the probing X-ray wavelength is tuned to a resonance in the material which depends on the occupied orbital. The small difference in scattering strength from the different atomic orbitals provides a contrast mechanism between manganese ions with different orbital occupations. This difference causes interference to produce new Bragg peaks in the diffraction pattern if the orbital occupancy is ordered throughout the crystal. In most of these materials a Jahn-Teller distortion and anti-ferromagnetic ordering occur at the same temperature and the relative strengths of the Jahn-Teller-phonon and spin contributions to the orbital ordering in the manganites remains an open question. Possible evidence for the observations of quantized disturbances of the orbital order, or orbitons, will be presented in chapter 6.

Chapter 3

Short pulse generation and the pump-probe technique

3.1 Introduction

The experimental work reported in this thesis makes use of short pulses of light spanning an energy range which covers 4 orders of magnitude, from the near-IR (∼0.7 eV) to X-ray wavelengths (∼7 keV). The commercial availability of stable, highly developed, short pulse (sub-50 fs) lasers has driven a rapid growth in ultrafast science. Ultrafast lasers are almost exclusively based on Ti:sapphire technology, which produces pulses with a central wavelengths around ∼800 nm. However, although the bandwidth is broad enough to produce short pulses the central wavelength cannot be tuned. Having the ability to tune the wavelength of the laser is often required in order to probe specific spectral features of materials.

This chapter will give an introduction to the experimental techniques used to to generate tuneable short pulses in different spectral regions. To create short pulses in the visible and the near-IR spectral regions, optical parametric amplifiers (OPAs) are used to amplify visible and IR light generated by self-phase modulation of 800 nm light in sapphire. The short pulse X-rays used in experiments described in this thesis are generated by 'slicing' the electron beam stored in a synchrotron storage ring with an intense Ti:sapphire laser. The sliced electrons can be used to generate femtosecond X-rays over the soft X-ray to hard X-ray spectral range.

The final section of this chapter gives an introduction to the 'pump-probe' technique which is used to initiate and measure the dynamics of the material, together with an explanation of

typical transients that are observed in such experiments.

3.2 Short pulse generation using optical parametric amplifiers

Light with a broad spectrum is required in order to generate short pulses of light in the time domain. This requirement is a result of the Fourier bandwidth theorem which relates the temporal duration, Δt, of a pulse to its spectral width, $\Delta\omega$ by $\Delta\omega\Delta t \geq \frac{1}{2}$. This section will outline the general methods for generating and amplifying broad-bandwidth radiation at optical and x-ray wavelengths.

3.2.1 Non-linear optics

Radiation from a Ti:Sapphire laser can be used to create tuneable broad-band radiation through the use of non-linear optics. For weak electric fields, the polarization, P, induced in a material is linearly dependent on the electric field strength E. However, for intense fields, the induced polarization can be expanded in a power series as

$$P = \chi^{(1)}E + \chi^{(2)}E^2 + \chi^{(3)}E^3 + \dots \tag{3.1}$$

where $\chi^{(n)}$ is the nth order susceptibility of the material.

A time dependent polarization emits electromagnetic radiation. If the electric field driving the polarization has the following temporal dependence,

$$E(t) \propto \cos(\omega t), \tag{3.2}$$

the linear term in equation 3.1 will result in radiation emitted at the same frequency. The second order polarization will have the following time dependence

$$P^{(2)}(t) \propto \cos^2(\omega t) = \frac{1}{2}(1 - \cos(2\omega t)). \tag{3.3}$$

Therefore, the second order non-linear polarization results in a field radiating at twice the frequency, or the second harmonic of the fundamental wavelength, and also generates a rectified, zero frequency, non-radiating field.

If the electric field consists of more than one frequency, such as

$$E(t) \propto \cos(\omega_1 t) + \cos(\omega_2 t), \tag{3.4}$$

then the non-linear response is

$$\begin{aligned} P^{(2)}(t) \propto (\cos(\omega_1 t) + \cos(\omega_2 t))^2 \propto \quad & c + \cos(2\omega_1 t) + \cos(2\omega_2 t) \\ & + \cos\left((\omega_1 + \omega_2)t\right) + \cos\left((\omega_1 - \omega_2)t\right). \end{aligned} \tag{3.5}$$

Therefore, as well as the rectified and second harmonic fields, fields at the sum frequency (SF) and difference frequency (DF) are also generated. Higher order processes will lead to further frequencies being generated in the material.

Broad-bandwidth radiation can be generated relatively easily via a process known as super-continuum generation (SCG) or 'white-light' generation. When an ultrashort pulse is focused into a transparent material, many non-linear optical processes effect the spatial, temporal and spectral properties of the beam. Self-phase modulation (SPM), is primarily responsible for the broadening of the spectrum. The intensity profile of the laser beam affects the refractive index of the material through the third order susceptibility, in a process referred to as the optical Kerr effect. This results in a time dependent refractive index, which modulates the frequency of the pulse to produce sidebands. Other effects include self focusing, multi-photon absorption and plasma formation, which effect the output beam properties in a nontrivial way [55].

By controlling the intensity and spatial profile of a laser beam in the transparent material a stable, single filament of 'white-light' (broad-bandwidth) can be generated. This can be compressed to produce short pulses with, for example prisms. However, the pulse energy generated is generally very low, usually a few pico Joules per nanometer of bandwidth [56]. Therefore, the 'white light' needs to be amplified before it can be used to initiate ultrafast dynamics.

When light enters a non-linear crystal it can be down-converted into two lower energy photons efficiently as long as energy and momentum conservation can be satisfied. If the input laser, referred to as the pump, has a frequency ω_p the down-converted signal and idler photons at frequencies ω_s and ω_i ($\omega_s > \omega_i$) have to satisfy the following relations

$$\hbar\omega_p = \hbar\omega_s + \hbar\omega_i, \tag{3.6}$$

$$\boldsymbol{k}_p = \boldsymbol{k}_s + \boldsymbol{k}_i. \tag{3.7}$$

Where $\boldsymbol{k}$ is the wavevector of the photon. This process can be seeded to stimulate the decay of a photon in the pump beam into one at the seed wavelength and a secondary photon at the

appropriate idler wavelength, amplifying the seed beam as well as creating an idler beam. If the crystal is pumped by an amplified beam the gain can be sufficiently high after one pass of a non-linear crystal to produce an intense beam. Amplification using this technique is called an optical parametric amplifier (OPA).

A major difficulty with using non-linear crystals is phase matching. Different frequencies have different velocities inside the non-linear crystal. This results in walk-off between the pump and signal beams and reduces the amount of gain possible. The phase matching condition (equation 3.7), for collinear beams, can be expressed as

$$n_p = \frac{n_s\omega_s + n_i\omega_i}{\omega_p}, \tag{3.8}$$

where n is the refractive index of the material. This can only be achieved in a uniaxial crystal as, for an isotropic transparent material $n_p > n_s > n_i$. Therefore, to achieve phase matching, the polarization of the pump beam must be different to that of the signal or idler, or both in a uniaxial crystal. Phase matching can then be achieved by directing the light along the appropriate crystallographic direction in order to satisfy equation 3.8. For such a configuration it is possible to show that the gain at the seed frequency, and also the idler, increases exponentially with crystal length [56].

The above considerations were for monochromatic beams. Short pulses, however, consist of a broad range of frequencies all of which need to be amplified. If the signal wavelength increases to $\omega_s + \Delta\omega$ the idler wavelength must decrease to $\omega_I - \Delta\omega$. For a fixed pump frequency, the phase mismatch can be expanded about the phased matched point to give

$$\Delta k = \frac{\partial k_s}{\partial w_s}\Delta\omega - \frac{\partial k_i}{\partial w_i}\Delta\omega = \left(\frac{1}{v_{gs}} - \frac{1}{v_{gi}}\right)\Delta\omega. \tag{3.9}$$

Where v_{gx} are the group velocities of the signal and idler pulses. The phase matching bandwidth, $\Delta\nu$ is inversely proportional to Δk and, therefore, is largest when the group velocities of the signal and idler beams are the same.

3.2.2 Short pulse generation at near-IR wavelengths*

Many insulators have gaps at near-IR wavelengths. Chapter 4 describes experiments on the organic Mott insulator (BEDT-TTF)-F_2TCNQ which has a Mott gap at 1.7 μm. This region

*The OPA described in this section was used in chapter 4 and is described in more detail in ref [57].

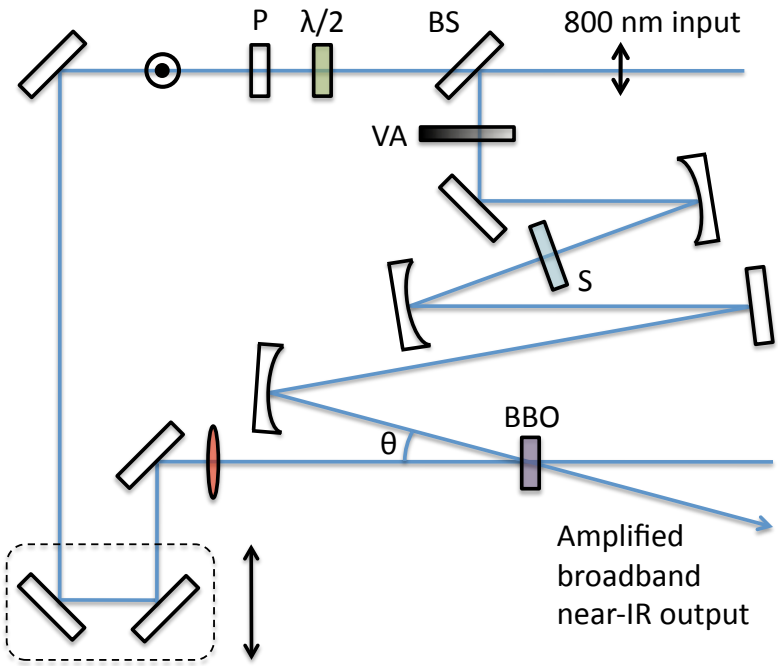

Figure 3.1: A Schematic of a near-IR OPA. P - Polarizer. $\lambda/2$ - Half wave plate. BS - beamsplitter. VA - Variable attenuator. S - sapphire crystal.

is particularly difficult to generate short pulses in as a single cycle of the electric field at 1.7 μm is approximately 5 fs.

To achieve a short pulse at such wavelengths, the output of a 800 nm Ti:saphhire laser was used as a pump for a broad-band optical parametric amplifier. A BBO non-linear crystal was cut for type I phase matching at the signal and idler degeneracy wavelength, 1.6 μm. At this wavelength, the bandwidth that can be phase-matched is limited by second order effects in equation 3.9 and depends on the derivatives of the group velocities, the group velocity delay or GVD. In BBO the GVD is zero for wavelengths at 1.45 μm, which is sufficiently close to the signal wavelength to enables a very broad spectral range to be phase matched.

A schematic for a near-IR OPA is shown in figure 3.1. The system is driven by 80 μJ, 150 fs pulses from a 1 kHz Ti:sapphire amplifier at 800 nm. Approximately 2 μJ is used to generate white light in a 3 mm sapphire crystal, the properties of which are controlled by adjusting the intensity of the 800 nm by using a variable attenuator and the position of the sapphire in the focus of the 800 nm beam. This generates broad-band radiation from 450 nm to over 2 μm.

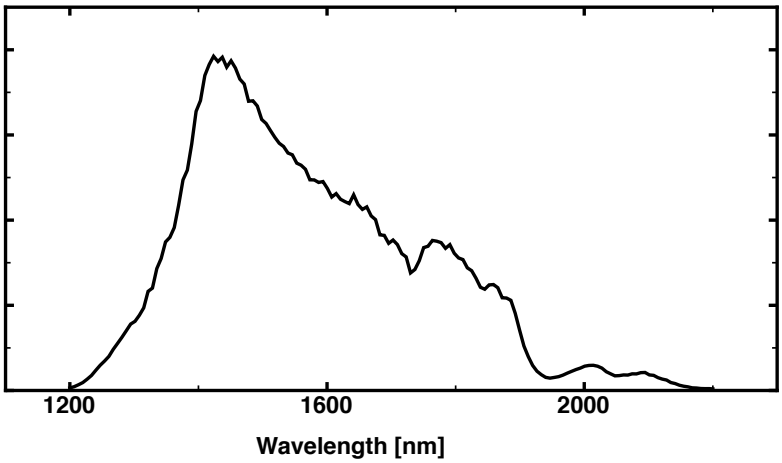

Figure 3.2: The amplified spectrum of the near-IR OPA

The white light is collimated before being refocused into the BBO crystal. The polarization of the 800 nm pump beam is rotated by 90° with a half-wave plate and a polarizer is used to reduce any residual horizontally polarized light. The light then bounces off two mirrors on a delay stage, which is adjusted to give temporal overlap between the pump and seed beam, before being focused into the BBO crystal. The pump and seed beams enter with a small angle, $\theta \approx 1°$, in order to separate the amplified beam from the pump beam.

The amplified spectrum is shown in figure 3.2. The spectrum was measured by a spectrometer equipped with an extended array of cooled InGaAs diodes. The amplified spectrum shows almost one octave of bandwidth ranging from 1.2 μm to 2.2 μm.

The amplified near-IR pulse still has a long temporal duration. This is because broad-bandwidth pulses are significantly effected by dispersion [58]. When light propagates through a material, or air, different frequencies of light experience a difference refractive index. As a result, each frequency will travel at a different speed through the material causing the pulse increasing its temporal duration.

The dispersion of the near-IR OPA is a complex function of the wavelength and cannot be compensated for using usual methods, such as prisms, gratings, or chirped mirrors. Therefore, adaptive optics have to be used which can compensate for an arbitrary dispersion. The compression is achieved by using a zero-dispersion $4f$-compressor with a deformable mirror placed in the Fourier plane. The size of the amplified beam is reduced by a telescope to less than 1 mm and is dispersed by a Brewster cut, SF56, prism. The light is collected by a curved

mirror which one focal distance (f=500 mm) away from the prism and reflects the light onto deformable mirror which is placed in the Fourier plane, one focal length away. The light is then reflected back through the prism and separated from the incoming beam by tilting the deformable mirror to provide a small vertical displacement of the beam after it has exited the prism.

The compressed beam's temporal properties are measured using the second harmonic generation frequency resolved optical gating (SHG-FROG [59]) technique in a 50 μm BBO crystal. The technique generates two replica pulses using a beamsplitter. Each pulse travels a separate path, before being focused and overlapped at a small angle in a non-linear crystal. When the two pulses are spatially and temporally overlapped in the crystal, a third pulse, at the sum-frequency of two input pulses, with a k-vector that is the sum of input k-vectors, is generated. The sum-frequency signal is spectrally resolved in a spectrometer.

By scanning the relative delay between the paths, the generation time of each second harmonic frequency can be measured. For an pulse that has optimal temporal compression, i.e. no chirp, all frequencies arrive at the same time. However, if the pulse is chirped, different frequencies will be generated at different delays. By measuring a FROG spectrum, the chirp of a pulse can be measured. From this, the change in path length, or phase, of each frequency component can be calculated in order for them to arrive at the same time. This phase is converted to a deformation of the deformable mirror, and when applied, the pulse is compressed. The accuracy of this technique is only limited by how faithfully the deformable mirror can reproduce the required distortion.

Using this technique, the near-IR pulse was compressed to 9.1 fs with an energy of proximately 200 nJ. The FROG spectrum and retrieved temporal duration of the intensity profile of the pulse are shown in figure 3.3.

3.2.3 Short pulse generation at visible wavelengths†

The visible spectral region is important for many molecular materials and several areas of condensed matter, such as the manganites. Generation of pulses in this spectral region requires

†The NOPA described in this section is the one built for the purposes of the $LaMnO_3$ experiment described in chapter 5. It is based on the NOPA design described in [60] at the Politecnico di Milano, which was used in the time resolved experiments on $Pr_{1-x}Ca_xMnO_3$ described in chapter 6.

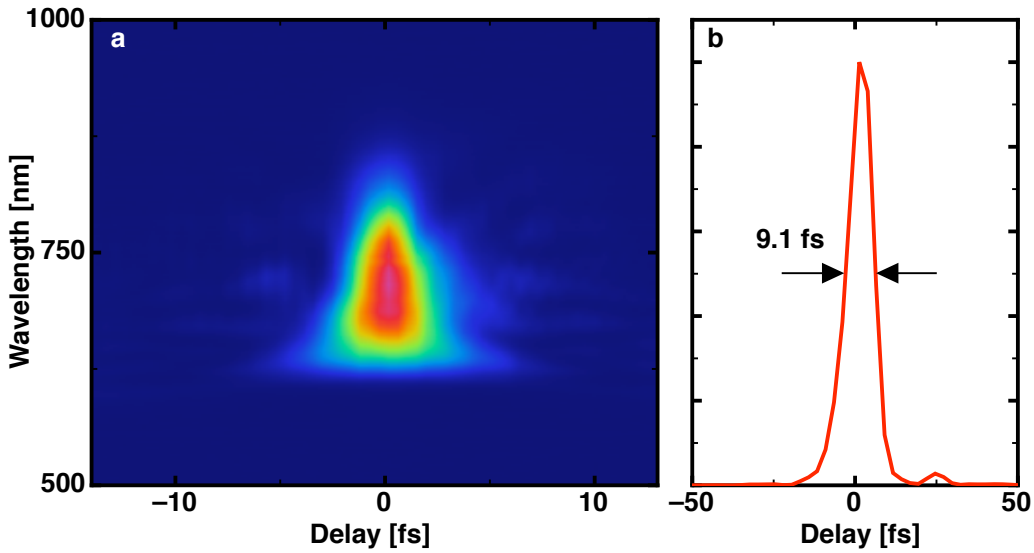

Figure 3.3: a. The second harmonic FROG trace. b. Reconstructed intensity profile of the compressed near-IR pulse

a different strategy to those in the near-IR.

The higher energy of the visible photons requires the non-linear BBO crystal to be pumped with the second harmonic of 800 mn. As the crystal cannot be cut at the 800 nm degeneracy point, according to equation 3.9, the amplified bandwidth will be narrow due to the group velocity mismatch. However, the bandwidth can be extended by adopting a non-colinear geometry. If α is the angle between the signal and pump beam and Ω is the angle between signal and idler beams, equation 3.7 becomes

$$k_p \cos\alpha = k_s + k_i \cos\Omega, \tag{3.10}$$

$$k_p \sin\alpha = k_i \sin\Omega. \tag{3.11}$$

Expanded each equation to first order as before gives,

$$\Delta k_{\parallel} = \frac{\partial k_s}{\partial \omega_s}\Delta\omega - \frac{\partial k_i}{\partial \omega_i}\cos\Omega\Delta\omega + k_i \sin\Omega\frac{\partial\Omega}{\partial\omega_i}\Delta\omega, \tag{3.12}$$

$$\Delta k_{\perp} = \frac{\partial k_i}{\partial \omega_i}\sin\Omega\Delta\omega + k_i \cos\Omega\frac{\partial\Omega}{\partial\omega_i}\Delta\omega. \tag{3.13}$$

For phase matching $\Delta k_{\parallel} = \Delta k_{\perp} = 0$, therefore, by multiplying equation 3.12 by $\sin\Omega$ and equation 3.13 by $\cos\Omega$ and subtracting gives the phase matching condition

$$v_{gs} = v_{gi}\cos\Omega. \tag{3.14}$$

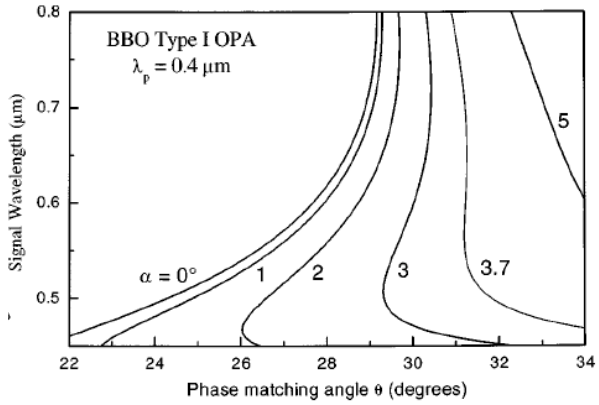

Figure 3.4: Phase matching angle of the BBO crystal for different pump-signal angles, taken from ref [56].

The phase matching condition corresponds to the group velocities in the propagation direction being matched.

If the pump-signal angle α is held constant the idler wavelengths will be spectrally dispersed from the OPA. Figure 3.4 shows the phase matching angle of the BBO crystal for different values of α. At $\alpha = 3.7°$ the curve is almost a vertical line, suggesting that a broad range of wavelengths (500-800 nm) are phase matched when the BBO crystal is cut at $\theta = 32°$.

The optical layout of the non-collinear optical parametric amplifier (NOPA) is very similar to the near-IR OPA. The pump wavelength is generated using BBO cut for type I phase matching, which produces the second harmonic (400 nm) with a perpendicular polarization to the fundamental wavelength, therefore no polarization rotation is needed. The residual 800 nm is removed from the beam using dielectric mirrors which have a high reflectivity at 400 nm only. White light is generated in sapphire and focused into the second BBO crystal, cut at $\theta = 32°$, for type I phase matching between seed and pump. The white light makes an angle of approximately 6° to the pump beam so that, on refraction into the crystal, the the angle $\alpha = 3.7°$ is achieved. A photograph of a NOPA built for the purposes of this thesis, and used to collect the data in chapter 5 is shown in figure 3.5.

Several amplified spectra are shown in figure 3.6 demonstrating the tuning ability and bandwidth available. The dispersion of the visible spectral region is less complex than that of the near-IR and can be easily compressed. This is achieved by the use of chirped mirrors which are optical mirrors that consist of a series of layered coatings. The coatings are designed to

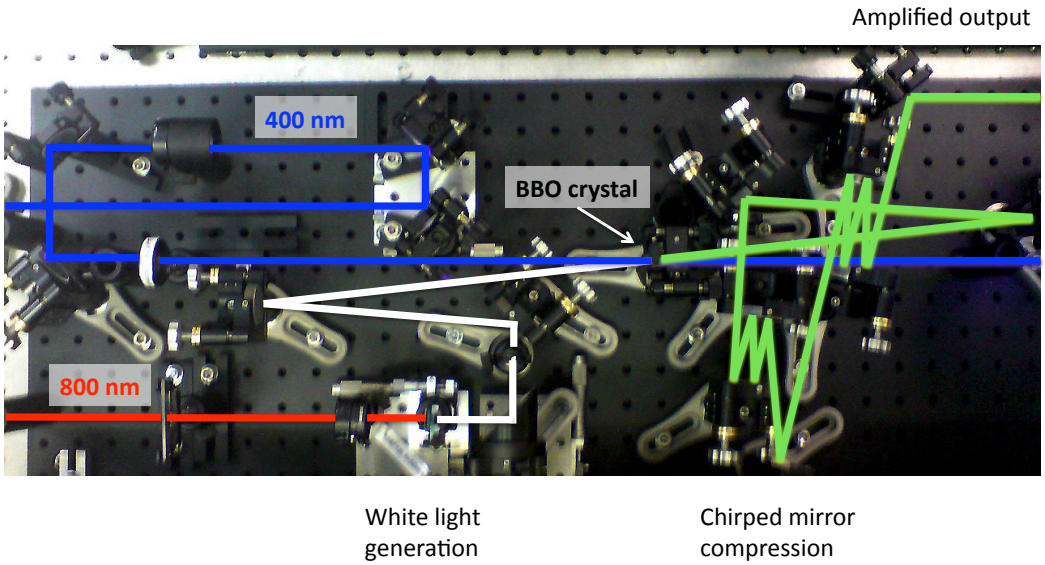

Figure 3.5: A photograph of the a NOPA built for the purposes of this thesis, and used to collect the data in chapter 5

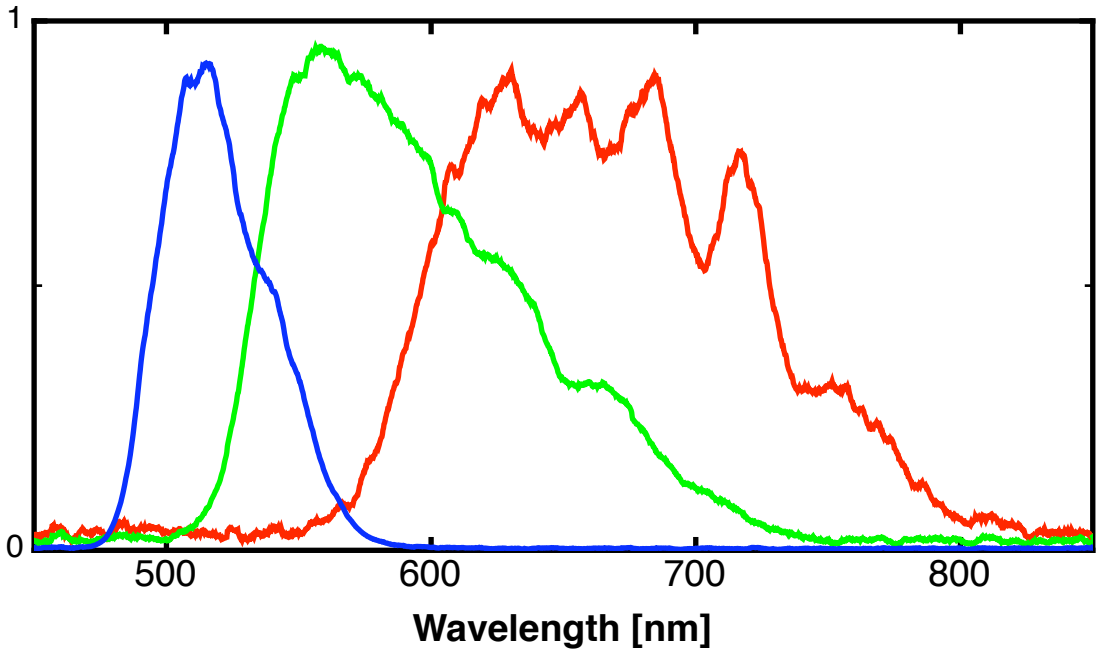

Figure 3.6: Various spectra produced by the visible NOPA

allow different colours to penetrate a different distance into the material and are designed to reduce the positive dispersion introduced by most materials. After 18 bounces off the chirped mirrors the pulse length of the visible pulse is reduced to less than 10 fs. The use of chirped mirrors simplifies the compression of the pulse, when compared to using prism, as the third order effects of the prisms are particularly difficult to compensate for in the visible spectral region [56, 61].

The pulse length is obtained from an intensity auto-correlation measurement made by two photon absorption in SiC diode. SiC has a band gap of 3.28 eV and is, therefore, insensitive to single photo absorption at visible wavelengths. Two-photon absorption can make the transition, therefore, the current generated in the diode is proportional to the intensity of the electric field. If two copies of the same pulse are overlapped on the SiC diode the photo-voltaic current generated is proportional to,

$$V(t) \propto \int_{-\infty}^{\infty} I(\tau)I(t-\tau)d\tau, \tag{3.15}$$

where the constant term is due to the two photon signal generated by each pulse and the cross term gives the intensity autocorrelation.

Unlike a FROG measurement, the signal cannot be spectrally resolved so the chirp of the pulse cannot be calculated. Therefore, in order to calculate the duration of the pulse, a form of the intensity profile has to be assumed. When a gaussian input pulse is assumed, the measured autocorrelation is also gaussian with a width which is $\sqrt{2}$ times bigger than the input pulse. Figure 3.7 shows the intensity autocorrelation of the visible NOPA. The autocorrelation is fitted with a gaussian of the form $Ae^{-t^2/2\sigma^2}$ and a value of $\sigma = 4.5$ fs is obtained which corresponds to a full width half maximum for the individual pulse of 7.5 fs.

3.3 Femtosecond X-rays generated using the slicing technique

Several techniques have been used to produce femtosecond bunches of X-ray radiation including, relativistic Thompson scattering [62], laser-produced plasmas [63–65] and slicing of an electron beam [6]. Free electron lasers (FELs) are a new source of high-brightness, coherent and short-pulse X-ray radiation. However, they are large scale machines and, at the time of writing, X-ray FELs are still being developed.

Laser plasma sources provide a high photon flux and have been used in many time resolved

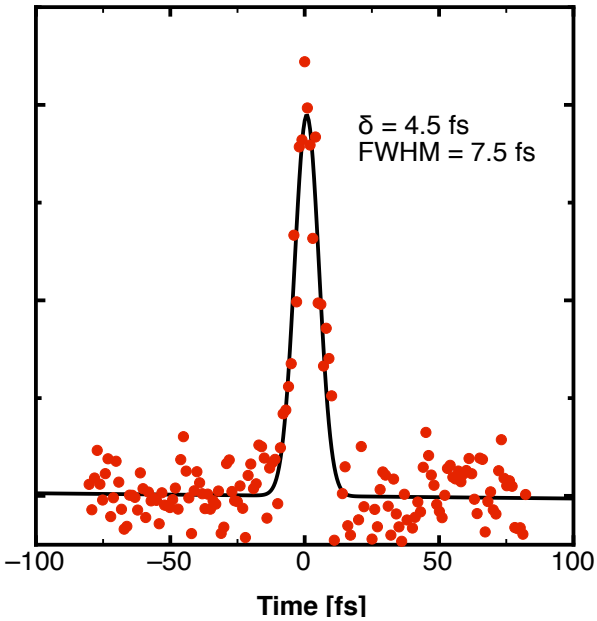

Figure 3.7: Intensity autocorrelation of the visible NOPA pulse.

experiments with pulse durations of a few hundred femtoseconds or less [66]. X-ray pulses are created by focusing an intense laser beam onto a solid target. The absorbed energy creates a high density plasma in the material. The free electrons are accelerated by the laser field and collide with ions in the plasma. The collisions are at high enough energies to eject electrons from the core levels of the ions. Transitions within the ion then lead to emission of line radiation at hard x-ray energies. The pulse duration of the X-rays is dictated by the pulse duration of the laser and the thermalization time of the plasma with the surrounding material. The latter can be very rapid and allows the production of very short X-ray pulses. Although the generated X-ray flux can be high ($\approx 10^{10}$ photons s^{-1} from copper), the wavelength is set by the atomic transitions of the material, which cannot be easily tuned.

This thesis reports on experiments performed using femtosecond X-rays generated using the slicing technique at the advanced light source (ALS) at the Lawrence Berkeley National Laboratory and the following gives an explanation of the technique. Slicing has the advantage that it is currently the only technique which can produce X-rays continuously tuneable from soft (200 eV) to hard (several keV) energies, making them a useful tool in X-ray spectroscopy and X-ray diffraction.

The slicing technique generates femtosecond X-rays by modulating the energy of an elec-

tron beam in the storage ring of a synchrotron with a femtosecond laser pulse. In a synchrotron, the storage ring supports a microwave field that traps and accelerates bunches of electrons in a circular orbit at speeds close to the speed of light. At several points throughout the ring there are strong magnetic devices called radiators or insertion devices which are used the alter the direction of the electron causing it to emit X-ray radiation. The three main insertion devices used to generate X-rays are bend magnets, wigglers and undulators. Bend magnets apply a large magnetic field perpendicular to the electron beam, causing the beam to deflect along an arc. The change in direction causes the electrons to emit broad bandwidth X-ray radiation along the tangental direction.

Wigglers and undulators consist of a two rows of permanent magnets separated by a gap of several millimeters. Along each row of magnets, the magnetic field orientation alternates over a length λ_w. As the electron bunch travels between the two rows of magnets, the magnetic field causes the electron bunch to oscillate. Wigglers emit high intensity, broad-bandwidth radiation as a result of the high amplitude oscillations made by the electron bunch. Undulators emit narrow-bandwith radiation due to the harmonic motion of the electrons. The spontaneous radiation emitted by a wiggler has a central wavelength given by [67]

$$\lambda_s = \frac{\lambda_w}{2\gamma^2}\left(1 + \frac{K^2}{2}\right). \tag{3.16}$$

Where γ is the Lorentz factor of the electrons and K is the deflection parameter.

If the emission wavelength and spatial mode of the wiggler radiation and laser are matched, the electron bunch will resonantly interact with the electric field of the laser [68]. Wavelength matching can be achieved by varying the gap of the wiggler, which changes the deflection parameter K, so that it overlaps with the output of a Ti:Sapphire amplifier. The total electric field in the cavity is the vector sum of the electric fields of the laser and wiggler. The total field energy stored in the cavity is the integral of the total electric field over the emitted solid angle and frequency range,

$$A = \int\int |\boldsymbol{E_T}|^2 dS d\omega = A_w + A_L + 2\sqrt{A_l A_w \Delta\omega_L/\Delta\omega_w}\cos\phi. \tag{3.17}$$

Where A_w and A_L are the energy density of the wiggler and laser electric fields with bandwidths $\Delta\omega_w$ and $\Delta\omega_L$ ($\Delta\omega_w < \Delta\omega_L$) respectively and ϕ is the phase of the electric field when the electron bunch enters the wiggler. The phase can be controlled by varying the delay

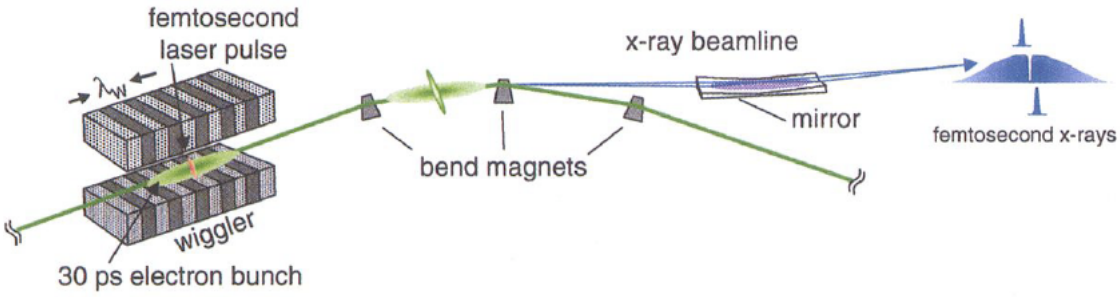

Figure 3.8: The experimental setup used to generated the first femtosecond bunches of electrons from the slicing technique. Taken from ref [6].

between the arrival of the electrons and laser radiation in order to maximize the interaction strength.

Equation 3.17 shows that the maximum energy, ΔE, that can be transfered from the radiation field into accelerating the electron bunch is

$$(\Delta E)^2 = 4A_l A_w \Delta\omega_L / \Delta\omega_w. \tag{3.18}$$

This creates sidebands in the energy domain of the electron beam, beyond the energy spread, σ, of the fundamental beam, which is typically 3 MeV. The 'sliced' electrons will have a temporal profile of order the slicing laser beam and can be physically separated from the main bunch by passing the beam through a bend magnet. As a result of the energy difference the higher-energy sliced beam is deflected less than the unsliced beam. The sliced electrons are then passed through an insertion device to generate a femtosecond bunch of X-rays that is spatially separated from the main beam and can be isolated with the use of apertures. The emitted X-ray wavelength depends on the properties of the insertion device used. If an undulator is used, high intensity radiation can be generated over a broadly tuneable range.

Schoenlein et al. were the first to demonstrate the slicing technique at the ALS [6]. A diagram of the setup used is shown in figure 3.8. A 100 fs laser, with 400 μJ pulse energy at 800 nm was used to slice the 1.5 GeV electron beam at 1 kHz. Slicing the electron bunch produced a shift in energy of 6 MeV, or $\sim 4\sigma$, from the central energy of the unsliced beam, with an r.m.s width σ. The insertion device used to generate the femtosecond X-rays was a second bend magnet. Even with a 4σ displacement, there are still unsliced electrons in the

wings of the electron profile which radiate picosecond-long X-rays. The ratio of femtosecond X-rays to the picosecond bunch depends on the energy and spatial profile of the electron beam. By turning the slicing laser on and off the slicing ratio of 10:1 was measured at the ALS.

Residual visible radiation generated by the electron bunch was used to perform a cross-correlation measurement of the X-ray pulse duration together with the 800 nm used to slice the X-ray beam and was found to be approximately 200 fs. The number of sliced photons generated depends on the radiation device and wavelength of the X-rays. Schoenlein estimates that $\sim 10^7$ photons s^{-1} per 0.1% bandwidth can be generated by an undulator at 2 keV, which is three orders of magnitude lower than plasma based sources.

One advantage of the slicing technique over devices which are based on the self amplification of spontaneous emission (SASE), such as unseeded FELs and linear accelerators is that there is absolute synchronization between the laser and the femtosecond x-rays. This is vital for the measurement of dynamics that require exact knowledge of the arrival time of the x-rays and eliminates the need for complex experiments to determine the jitter between electronically synchronized lasers and x-ray sources [9].

3.4 Pump-probe

The most common experimental technique used to study ultrafast dynamics is the pump-probe measurement. In these experiments, a strong 'pump' laser beam initiates some dynamics in the material. The response of the material is measured at some time, Δt, later a weaker 'probe' laser which samples the properties of the excited region. By varying the time delay between the pump and the probe the dynamical change in the materials properties can be inferred by measuring the changes to the probe beam.

The relative arrival time of the pump and probe is usually controlled by varying the path traversed by one of the laser beams. This can be realized by mounting a retro-reflective mirror onto a motorized translation stage. If the mirror is moved a distance x, the additional path length traversed by the laser beam, $2x$ induces a delay $\tau = 2x/c$, where c is the speed of light. Therefore, in order to change the delay between two laser beams by 10 fs, the distance travelled by one beam has to be increased by 1.5 μm.

Laser based pump-probe measurements usually measure changes to the probe intensity

which in turn gives the changes in reflectivity or transmission of the sample depending on the experimental geometry. Data from the latter is often easier to interpret as it is directly related to the absorption of the material, whereas the reflectivity has a more complex dependence on the the fundamental properties of the material. However, transmission experiments can only be performed on thin transmissive materials in order to limit the effects of material dispersion on the time resolution of the measurement.

Degenerate pump-probe measurements derive the probe pulse from a replica of the pump pulse. The probe beam is created by taking a small portion of the laser beam from a reflection off a beam splitter. This setup has the advantage that the path differences between pump and probe beams can be relatively small, making it easier to find the temporal overlap between the two beams. A degenerate pump-probe setup is used in the experiments in chapter 4.

Two-colour pump-probe measurements use a probe which is at a different wavelength to the pump pulse. In molecular systems this is particularly useful in looking at how pumping one transition affects transitions at different wavelengths. An advantage of the two colour technique is that pump light that is scattered into the detector can be significantly reduced by the use of band pass filters which can dramatically reduce the noise and background of the detected signal. A difficulty with two-colour pump-probe measurements arises from the difference in path lengths between the two beams. If the two colours are generated by two independent NOPAs, as used in chapters 5 and 6, the path difference can be very large and finding the temporal overlap of the two beams can be difficult.

When a material is probed with X-rays there are significant additional challenges. These are described in detail in chapter 7 and appendix A.

3.4.1 Transient reflectivity and coherent phonon generation

The effects of an intense pulse of light on the reflectivity of a solid is non-trivial, consisting of many different processes, which occur over a range of timescales. In general, the energy in the pump pulse goes into exciting the electronic sub-system, either exciting the electrons across a gap in a semi-conductor or higher up the band in a metal. This usually results in a prompt change in reflectivity. Subsequent changes in reflectivity are the result of how this energy is redistributed throughout the material. The initial electron distribution is non-thermal and thermalizes through electron-electron scattering and occurs on a timescale, τ_{e-e}.

The electronic timescale varies from a few femtoseconds to several hundred femtoseconds depending on the electron distribution and the screening of the electric fields. [69].

The electrons can also thermalize with the lattice via electron-phonon scattering, which occurs on a timescale, τ_{e-ph}. This timescale typically spans $\sim$100 fs to several picoseconds. Longer timescale processes can correspond to electron-hole recombination and heat diffusion from the excited region. This results in several timescales observed in the recovery of the reflectivity signal. As discussed in chapter 1, if a photo-induced phase transition occurs the changes in reflectivity can often exhibit bottleneck timescales, indicating the timescale over which the phase transition occurs [29].

In addition to the incoherent processes describe above, which often lead to signals which decay exponentially with time, large amplitude oscillations are often observed. The frequency of the oscillation match those measured in Raman scattering measurements which shows that the oscillations are due to vibrations of the crystal lattice. The oscillations can only be observed when the material is excited by a laser pulse which is short compared to the period of the oscillation indicating that a large number of phonons are excited coherently.

The oscillations can be observed in both absorbing and transparent materials. Early analysis suggested the driving force behind the oscillations in transparent materials was different to that in absorbing materials, as the former exhibited a sine-like dependence, whereas oscillations in absorbing materials exhibit a cosine-like dependence.

In transparent materials, the mechanism was described in terms of impulsive stimulated Raman scattering (ISRS) [70]. In Raman scattering, light at frequency ω_L is inelastically scattered by the emission or absorption of a phonon of frequency Ω via a transition to a virtual level as shown in figure 3.9. The lower energy photon is called the stokes photon and is scattered to a frequency $\omega_S = \omega_L - \Omega$. The higher energy photon is called the anti-stokes photon and has an energy $\omega_a = \omega_L + \Omega$. The process can be stimulated if the laser pulse contains a bandwith $\Delta\omega > \Omega$, as both the fundamental and shifted photons will be present in the beam. If such a pulse is temporally compressed close to the Fourier limit, the resulting pulse duration will be less than the period of the oscillation. Therefore, a high intensity pulse can excite a large number of phonons coherently.

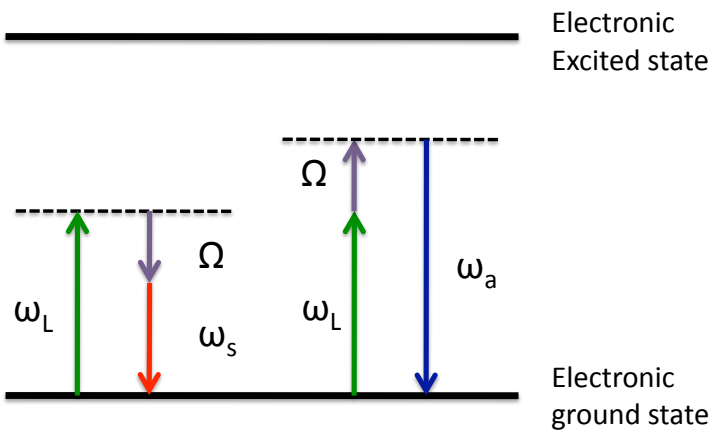

Figure 3.9: Raman scattering by of light by phonons. Light can be inelastically scattered by the creation of phonon and the emission of a lower energy, stokes photon, or by the absorption of a phonon and the emission of a higher frequency anti-stokes phonon. Non-resonant Raman scattering occurs when transitions are to virtual levels.

The polarization induced by such a pulse in a transparent is given by given by

$$P_i = \sum_j \chi_{ij} E_j, \tag{3.19}$$

and the energy stored in the polarized material is

$$W = \frac{1}{2} \langle \boldsymbol{P}.\boldsymbol{E} \rangle = \left\langle \sum_{i,j} \chi_{ij} E_i E_j \right\rangle. \tag{3.20}$$

Therefore, the force of the phonon-mode Q is

$$F_Q = \frac{dW}{dQ} = \left\langle \sum_{i,j} \frac{d\chi_{ij}}{dQ} E_i E_j \right\rangle. \tag{3.21}$$

For a beam with a gaussian temporal distribution the force will be, $F_Q \propto e^{-t^2/\tau^2}$, where τ is a measure of the pulse duration.

The response of the phonon mode can be modeled by the classical equation

$$\rho(\ddot{Q} + 2\gamma\dot{Q} + \Omega^2 Q) = F_Q, \tag{3.22}$$

where ρ is the reduced mass of the normal mode, and γ is the damping rate. Therefore, if the pulse duration is short ($\tau \to 0$), the force F will be impulsive and the phonon will oscillate

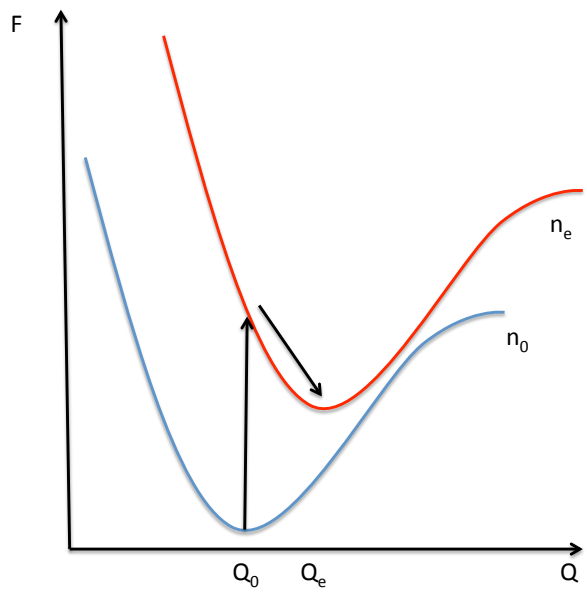

Figure 3.10: Change in free energy, F, due to the excitation of carriers across a band gap. The excitation causes a shift in the equilibrium position of the phonon coordinate causing the system to oscillate until the equilibrium value is reached.

like $\sin(\Omega t)$. In addition, as the force is dependent on the susceptibility, χ, it will retain the Raman symmetry of the crystal and all Raman modes should be excitable.

In absorbing materials, the mechanism of displacive excitation of coherent phonons (DECP) was suggested as the origin for the oscillations [71]. The phonon mode equilibrium coordinate, Q_0, is a function of the free energy of the system, which depends on the electronic distribution in the material. The absorption of photons changes the electron distribution in the material, which in turn modifies the free energy. The sudden change to the free energy surface can change the equilibrium position of the phonon modes, and possibly the frequencies. As a result, the phonon is in an excited state and experiences a force causing it to oscillate back to the new equilibrium position as demonstrated in figure 3.10.

For a two band semiconductor, the number of electrons in the conduction band n can be written as,

$$\dot{n} = P(t) - \beta n, \tag{3.23}$$

where $P(t) = \epsilon_p g(t)$ is the pumping rate, $g(t)$ is the normalized lineshape of the pump pulse and ϵ_p is proportional to the pump energy.

If the equilibrium phonon coordinate has a linear dependence on the electron density in the upper band then,

$$Q_0(t) = \kappa n(t), \tag{3.24}$$

and the phonon amplitude Q, about the 'equilibrium' position Q_0 is

$$\ddot{Q}(t) + 2\gamma\dot{Q}(t) = -\Omega^2(Q(t) - Q_0(t)).. \tag{3.25}$$

By substituting the solution $n(t) = \epsilon_p \int_{-\infty}^{\infty} g(t-\tau)e^{-\beta\tau}$ of equation 3.23 into equations 3.24 and 3.25, a solution of the form

$$Q(t) \propto \int_{-\infty}^{\infty} g(t-\tau)\left[e^{-\beta\tau} - e^{-\gamma\tau}\left(\cos(\omega' t) - \frac{\beta'}{\omega'}\sin(\omega' t)\right)\right] d\tau, \tag{3.26}$$

is found with $\beta' = \beta - \gamma$ and $\omega' = \sqrt{\omega_0^2 - \gamma^2}$.

Therefore, in the impulsive ($g(t) \to \delta(t)$) and weak damping ($\omega_0 \gg \gamma$) limit, the phonon will oscillate as $Q(t) \propto \cos(\omega_0 t) - \frac{\beta}{\omega_0}\sin(\omega_o t)$ on top of a decaying background. In most cases, the lifetime of excited state is much greater than the period of the phonon, i.e. $\beta \ll \omega_0$ and the oscillations be predominantly cosine-like.

The difference in phase between the ISRS and DECP is a direct result of the difference in the applied force. In ISRS the force on the phonon system is proptional to e^{-t^2/τ^2} which is impulsive as the force tends to a delta function for short pulses. In the DECP mechanism the force is proportional to $\int_{-\infty}^{\infty} e^{-t^2/\tau^2}$ which is said to be displacive as the force tends to a step function for short pulses.

The excitation of electrons across the gap should be symmetric for isotropic systems, therefore only phonon modes of A symmetry should be excited as these modes do not change the symmetry of the system. However, Garret et al. measured oscillations at both the the A_g and E_g frequencies in Sb and showed that the ratio of the two modes and polarization dependence was the same as the Raman mechanism [72].

Recently, Stevens et al. demonstrated that the DECP mechansim was, in fact, a resonant case of Raman scattering [73]. By considering the Hamiltonian (with $\hbar = 1$)

$$\hat{H} = \frac{1}{2}\hat{P}^2 + \frac{\omega_0^2}{2}\hat{Q}^2 + \hat{H_e}^2 - \hat{\Xi}\hat{Q} - \hat{\boldsymbol{\Delta}} \cdot \boldsymbol{E}, \tag{3.27}$$

Where $\hat{Q}$ and $\hat{P}$ and the phonon amplitude and conjugate momentum operators respectively. $\hat{H_E}$ is the Hamiltonian of the electronic sub system, $\hat{\Xi}\hat{Q}$ represents the electron-phonon coupling and $\hat{\boldsymbol{\Delta}} \cdot \boldsymbol{E}$ represents the coupling between the electric field and the electronic sub-system.

From equation 3.27, the equation of motion for the phonon amplitude can be derived,

$$\frac{d^2 \left\langle \hat{Q} \right\rangle}{dt^2} + \omega_0^2 \left\langle \hat{Q} \right\rangle = \left\langle \hat{\Xi} \right\rangle . \tag{3.28}$$

By calculating $\left\langle \hat{\Xi} \right\rangle$ Stevens et al. were able to show that the force on the phonon mode depended on the symmetry of the Raman tensor and the polarization of the electric field. When the absorption is low, the force on the phonon mode is impulsive and proportional to $d\Re(\epsilon)/d\omega$, whereas when the material is absorbing the force is displacive (cosine-like) and proportional to $\Im(\epsilon)$.

In laser-laser pump-probe experiments, the effects of the phonon modes are only observed indirectly through their effects on the reflectivity or transmissivity. However, phonon modes caused by displacive excitation [22] and impulsive excitation [74] have been observed in laser pump, X-ray probe measurements, which enables a full reconstruction of the ionic motions associated with the phonon mode.

Chapter 4

Photoinduced dynamics of a 1D Mott insulator

4.1 Melting the Mott state with light

In analogy with the effects of chemical doping, photo-excitation can have dramatic effects on materials with strongly-correlated electrons, inducing large changes in the electronic [24], magnetic [75] and optical properties of the material [23]. Mott insulating materials with quasi-one dimensional structures are of particular interest. The low dimensionality reduces the electronic bandwidth allowing the Coulomb interaction to dominate the physics, giving rise to new phenomena not found in higher dimensional materials [76, 77].

Iwai et al. were amongst the first to report on the photo-induced dynamics in a one dimensional material [78]. Iwai investigated the response of the charge-transfer insulating compound $[Ni(chxn)_2Br]Br_2$, which forms one dimensional hybridization states between Ni and Br ions. The strong electron-electron interactions open a charge transfer gap of 1.3 eV between the Br $4p$-level and the Mott split Ni $3d$-level.

$[Ni(chxn)_2Br]Br_2$ was excited above the charge transfer gap at 1.5 eV and the reflectivity probed over the range 0.1-2 eV. For an excitation fluence corresponding to the photo-excitation of 50% of the Ni ions, a prompt increase in reflectivity, as high as 200%, was observed at low photon energies, together with a 50% reduction in the reflectivity at the charge transfer resonance. The behaviour was interpreted as the formation of a metallic state, with a Drude response at low energies and the collapse of the charge transfer resonance. Analysis of the

reflectivity change with reduced pump fluence suggested that when less-than one Ni ion in ten was excited, the Mott state was maintained. In this case, a Drude response at low photon energies was not observed and, instead, there was an increase in reflectivity in the gapped region which was attributed to the formation of a polaronic state.

The formation of a photo-induced metallic state in a two-dimensional system with Mott insulating character was studied by Perfetti et al. by measuring the time dependent change in the photoemission spectra of $1T$-TaS_2 [10, 79]. The transient photoemission spectra revealed the energy distribution of the electrons in the vicinity of the Fermi-level of the material. In the ground sate the lower Hubbard band was resolved and no spectral weight was found at the Fermi-level. Photo-excitation resulted in the transfer of spectral weight from the lower Hubbard band to the Fermi-level, indicating the formation of the metallic state. The formation of the metallic state occurred within the time-resolution of the measurement ($\approx$ 50 fs) and the mechanism behind the transition was attributed to the increase in the electronic temperature.

Both of these studies were performed in materials with large electron-phonon couping. Due to the Peierls effect, this occurs in most low dimensional materials. However, (BEDT-TTF)-F_2TCNQ is an exception and exhibits very low electron-phonon coupling, enabling purely electronic effects to be observed. Pump-probe reflection spectroscopy of (BEDT-TTF)-F_2TCNQ [80] shows long-term dynamics similar to those reported in the charge-transfer compound. At an excitation density of one (BEDT-TTF) molecule in ten, the reflectivity at the Mott gap was reduced by 40% and an increase in spectral weight at low photon energies was observed, again indicative of a Drude response. However, unlike $[Ni(chxn)_2Br]Br_2$, the gapped polaronic state was not observed at low excitation densities.

Time dependent simulations of photo-excited Mott insulators have been performed by Takahashi et al. [81]. The results of the simulations agree well with experimental observations. At low photo-doping densities, Takahashi et al. showed that there is a coexistence of the Mott insulator and free carriers. However, at photo-doping densities above $\approx 10\%$ the Mott gap is destroyed and a metallic state is formed.

In all experiments to date, the time resolution of the measurements has been restricted to 100 fs or longer, which is insufficient to probe the dynamics of the formation of the metallic state. This chapter reports on measurements of the collapse of the Mott insulating state

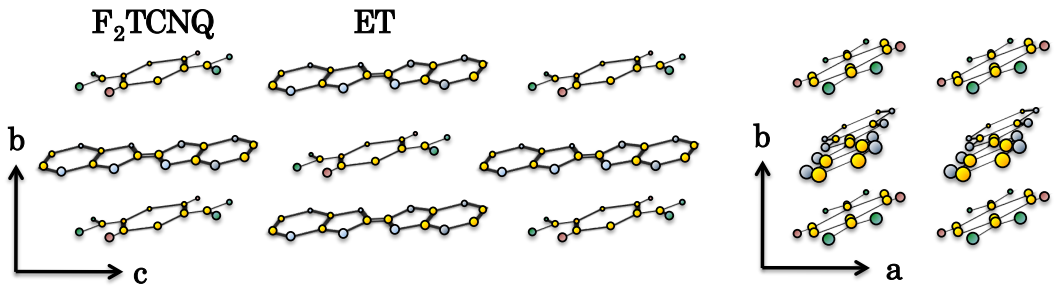

Figure 4.1: A representation of the BEDT-TTF F_2TCNQ crystal structure in the *bc* and *ba* planes

in (BEDT-TTF)-F_2TCNQ with sub-10 fs spectrally resolved pump-probe spectroscopy. The properties of this material, which are described in the following section, make it an ideal choice to study the ultrafast dynamics of insulator-metal transition in one-dimension.

4.2 BEDT-TTF F_2TCNQ

(BEDT-TTF)-F_2TCNQ or ET-F_2TCNQ is a one dimensional organic Mott insulator. F_2TCNQ is an acceptor molecule and ET is a donor molecule. They crystallize to form a 'mixed-stack' ionic crystal with a half-filled electronic band. The crystal structure is shown in figure 4.1. The crystal is orthorhombic with the P2/m space group symmetry. The dimensions of the unit cell are $a = 5.79$ Å, $b = 8.201$ Å and $c = 1186.34$ Å. ET and F_2TCNQ molecules are alternatively stacked directly on top of each other along the b-axis and have a greater intermoleculular separation than most other charge transfer solids [82]. The molecules are arranged side-by-side along the c-axis. Along the a-axis, the donors and acceptors lie in single chains with the distances between ET molecules being shorter than their van der Waals radius. Analysis of the carbon double bond length in the ET molecules shows that the charge transfer between ET and F_2TCNQ is complete, i.e. the donor charge completely localized on the acceptor molecule.

One dimensional half-filled systems are susceptible to a Peierls distortion (see chapter 1), which splits the conduction band, resulting in an insulating material. However, ET-F_2TCNQ shows no evidence for lattice dimerization in the X-ray diffraction data, optical properties or magnetic susceptibility over a wide temperature range.

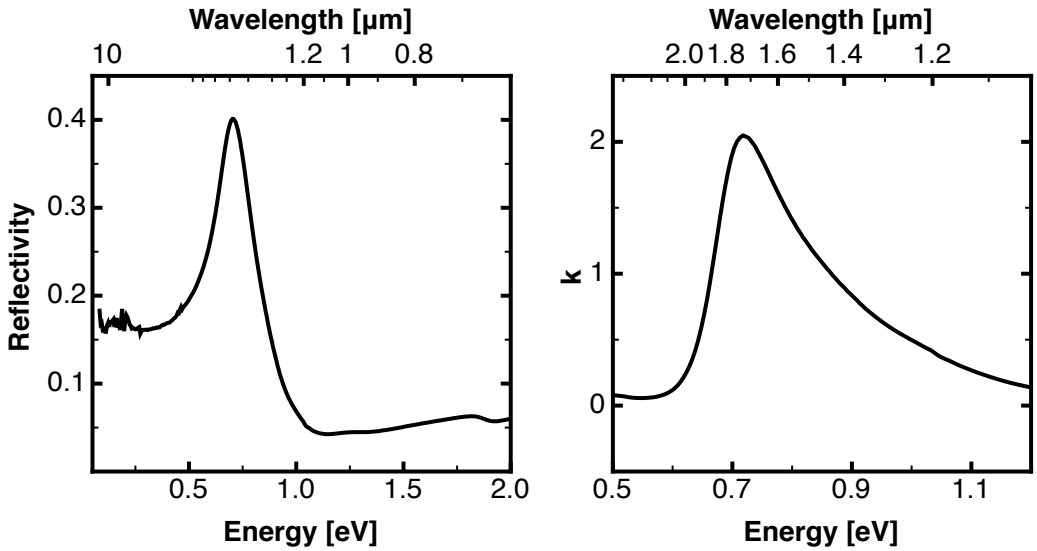

Figure 4.2: The reflectivity and imaginary part of the refractive index for ET-F_2TCNQ

ET-F_2TCNQ also has low magnetic coupling constant, with an anti-ferromagnetic state being formed at $T_N = 30\,K$. Again, the spin degree of freedom is separated from the lattice and no spin-Peierls distortion is observed. These effects allow ET-F_2TCNQ to be considered a pure electronic insulator.

The one dimensional nature of the material is apparent from reflectivity measurements, which show a strong polarization dependence. Figure 4.2 shows the reflectivity of light polarized along the a-axis*, together with the imaginary part of the refractive index which was obtained by manipulating the Kramers-Kronig transformation of the reflectivity data. A large spike in the reflectivity is observed at 0.7 eV which is assigned to the Mott transition ET^+ $ET^+ \rightarrow ET^{2+}$ ET^0, due to the proximity of the ET molecules and the strong localization of the charges on F_2TCNQ sites.

From temperature dependent measurements of the reflectivity, Yakushi et al. determined the value of $U = 1.4$ eV for the TCNQ molecule [83]. As the gap at 0.7 eV corresponds to transitions between ET sites, the value for U on the ET molecule is expected to be significantly lower. However using the value of U=1.4 eV and a gap energy of 0.7 eV in equation 2.3 puts an upper limit on the electron transfer integral $t < 175$ meV. This value can be converted to a characteristic timescale, $T > 2$ fs, using the Heisenberg energy-time uncertainty principle (equation 1.2), for electrons to move between ions.

*Reflectivity values were provided courtesy of Prof. Okamoto, Tokyo University.

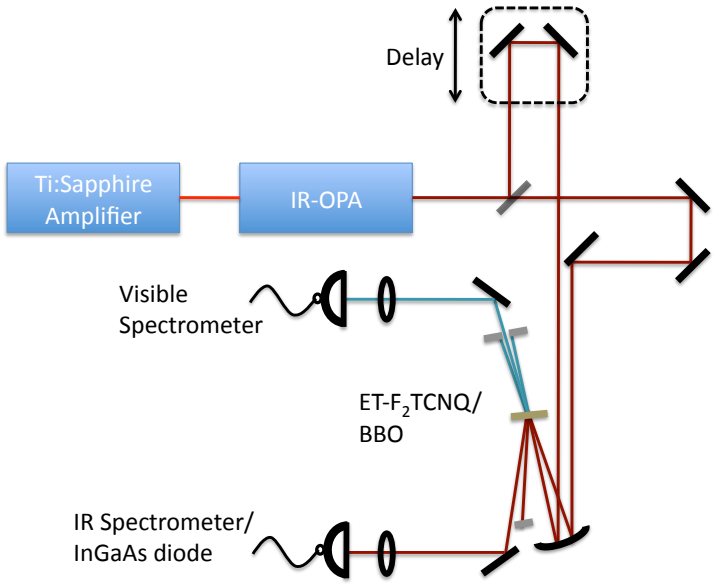

Figure 4.3: Optical setup for the ET-F_2TCNQ experiments

4.3 Photo-induced melting of the Mott state measured on a characteristic timescale

4.3.1 Experimental setup

The 0.7 eV (1.7 μm) gap of ET-F_2TCNQ represents significant challenges for probing the response of the material on a timescale that is commensurate with the fundamental processes which control the materials properties. Therefore a novel IR-OPA, which produced sub-10 fs pulses centred at 1.7 μm, was used. The details of the spectra and pulse duration are given in chapter 3.

The 200 nJ output pulse energy of the OPA was split to generate two beams in a degenerate pump-probe setup. The two beams were redirected to arrive parallel to each other at a curved mirror, and separated by 2 mm. The sample was placed in the focus of the curved mirror, where the two beams were overlapped. The light arrived at the sample surface at a near normal angle of incidence and the change in reflectivity of the probe beam was measured. The reflected pump beam was physically blocked from entering the detector and the good surface quality minimized pump scatter. The experimental setup is shown in figure 4.3.

The pump and probe beams were focused to a 60 μm spot, which gave a maximum pump

fluence at the sample surface of $3.5\,\mathrm{mJ\,cm^{-2}}$. Both pump and probe were σ-polarized and the sample rotated so that the polarization was parallel to the a-axis of the crystal in order to excite and measure the Mott gap. No time-resolved signal could be observed when the sample was rotated by 90° and pumping was perpendicular to the a-axis.

The change in reflectivity was measured using two techniques. The power dependence measurements were taken using an InGaAs diode and a lock-in amplifier. The spectrally resolved reflectivity was measured with a optical multi-channel analyzer. The measured reflection, $R_m(t,\lambda)$, at time t and wavelength λ is the product of the reflectivity of the ET-F_2TCNQ sample $R(t,\lambda)$ and the spectral profile of the incoming probe pulse $S(\lambda)$. Reflectivity spectra were taken with a 1 second integration time, and multiple time traces were acquired in order to average the data. The relative change in reflectivity could be calculated in the following way,

$$\frac{R_m(t,\lambda) - R_m((t<0),\lambda)}{R_m((t<0),\lambda)} = \frac{S(\lambda)(R(t,\lambda) - R_0(\lambda))}{S(\lambda)R_0(\lambda)} = \frac{\Delta R(t,\lambda)}{R_0}, \tag{4.1}$$

where $R_m(t<t_0,\lambda)$ is the average measured reflection before the pump pulse has arrived. The absolute time-dependent reflectivity can be obtained by using the measured values of the reflectivity shown in figure 4.2.

The ET-F_2TCNQ sample could be removed and replaced by a BBO crystal. This enabled the cross-correlation between pump and probe pulses to be measured at the sample position without modifying the beam paths. This enabled the pulse duration at the sample and time-zero delay to be accurately determined.

4.3.2 Long timescale dynamics

In order to compare the results presented in this thesis to those of Okamoto et al; it is useful to calculate the number of excited ET molecules. The spatial part of the propagation of a electromagnetic plane wave, E, entering a material along the x direction with a complex refractive index $\tilde{n} = n + ik$, can be described by

$$E(x) = E_0 e^{i\frac{2\pi\tilde{n}}{\lambda}x} = E_0 e^{-\frac{2\pi k}{\lambda}x} e^{i\frac{2\pi n}{\lambda}x}, \tag{4.2}$$

Where E_0 is the amplitude of the electric field on entering the material with a wavelength λ.

The real, decaying, exponential gives the attenuation of the wave as it travels through the media. The penetration depth is defined as the point at which the intensity of the electric field

has dropped by e^{-1} from its initial value. Therefore, the penetration depth can be calculated using

$$l_p = \frac{\lambda}{4\pi k}. \tag{4.3}$$

For a wave with a wavelength of 1.7 μm, corresponding to the peak in the Mott transition, $k = 2.01$ and penetration depth is $l_p = 67\,\text{nm}$.

The energy per photon at 1.7 μm is $E = hc/\lambda = 1.16 \times 10^{-19}\,\text{J}$, therefore, the number of photons arriving at the surface of the sample N_s when the laser fluence is $3.5\,\text{mJ}\,\text{cm}^{-2}$ is $N_s = 3 \times 10^{16}\,\text{cm}^{-2}$. A fraction, $R = 0.39$ at 1.7 μm, of which are reflected. As the calculation is a rough estimate, it is assumed that, out of the remaining $(1 - R)$ photons, $(1 - e^{-1})$ are absorbed uniformly over the penetration depth, l_p, to obtain the number of photons absorbed in the given volume, N_{abs}. This gives

$$N_{\text{abs}} = (1 - R)(1 - e^{-1})N_{\text{in}}/l_p = 1.7 \times 10^{21}\,\text{photons}\,\text{cm}^{-3}.$$

The volume of the ET-F_2TCNQ unit cell is $1192\,\text{Å}^3 = 1.2 \times 10^{-21}\,\text{cm}^3$ and contains 4 ET molecules. Therefore pumping at 1.7 μm with a pump fluence of $3.5\,\text{mJ}\,\text{cm}^{-2}$ pump corresponds to an excitation of 50% of the ET molecules.

The power dependence was measured by reducing the pump power with 100 μm-thick neutral density filters, which reduced the intensity at each wavelength by a constant amount without causing any significant dispersion of the pump-pulse. The transient changes in reflectivity are shown in Figure 4.4 on a log scale. The data can be fitted by a bi-exponential decay of the form,

$$\frac{\Delta R(t)}{R} = A_1 e^{-t/\tau_1} + A_2 e^{-t/\tau_2} + C,\ t > 0. \tag{4.4}$$

The three terms in equations 4.4 can be attributed to electron-electron, electron-phonon and phonon-phonon thermalization by their temporal dependence. Table 4.1 summarizes the fitted parameter values for each of the measured pump fluence. The mean electron-electron equilibrium timescale was measured to be $\tau_1 = 250 \pm 30\,\text{fs}$, which slightly increased as a function of pump fluence, showing a small screening of the Coloumb repulsion in the highly excited state [69]. The electron-phonon coupling was constant over the measured range with a mean time constant $\tau_2 = 1.5 \pm 0.1\,\text{ps}$, in good agreement with those reported by in Ref [80].

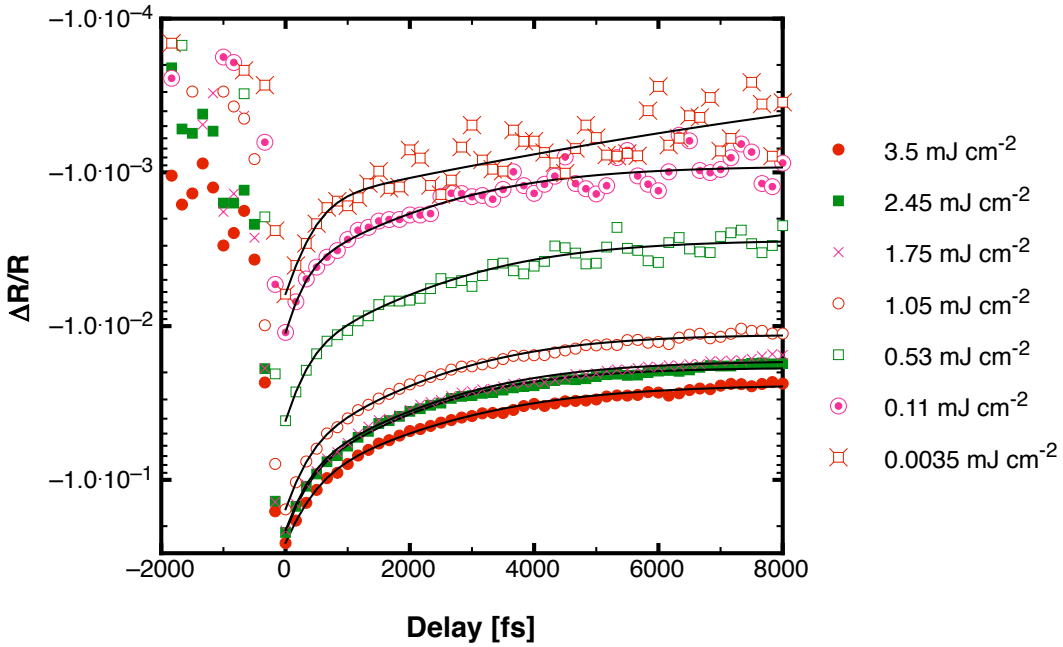

Figure 4.4: Intensity dependence of the change in reflectivity at the Mott gap. Solid lines are fits to the data using equation 4.4.

Pump Power mJ cm^{-2}	C	A_1	τ_1 fs	A_2	τ_2 fs
3.5	-0.0243(5)	-0.147(4)	300(12)	-0.086(4)	1660(90)
2.45	-0.01854(4)	-0.120(4)	240(11)	-0.080(4)	1376(61)
1.75	-0.01682(4)	-0.123(4)	251(11)	-0.073(3)	1490(74)
1.05	-0.0114(2)	-0.091(2)	245(10)	-0.053(2)	1447(56)
0.53	-0.0028(1)	-0.026(1)	231(20)	-0.013(1)	1618(140)
0.11	-0.0009(1)	-0.0066(4)	207(20)	-0.0035(4)	1530(200)
0.0035	-0.0002(4)	-0.0046(3)	278(40)	-0.0014(2)	4000(3000)

Table 4.1: Summary of the parameters used to fit the intensity dependence of the transient reflectivity of ET-F_2TCNQ using equation 4.4.

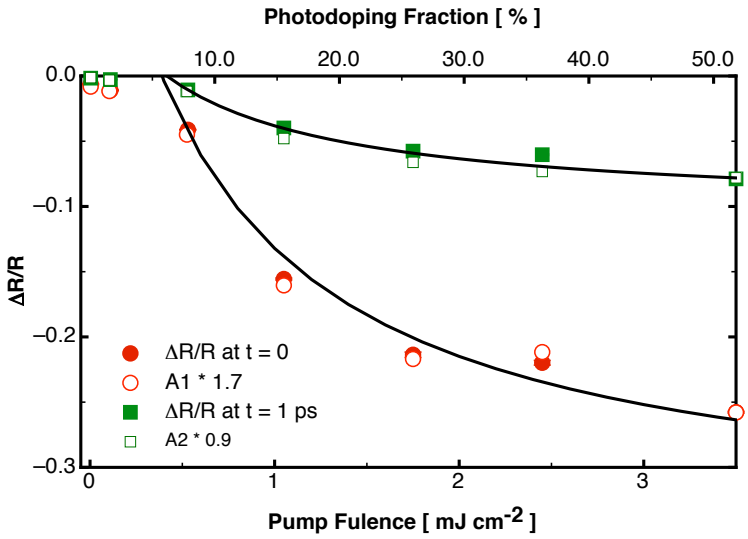

Figure 4.5: Threshold and saturation plots of Mott-insulator to metal photo-induced phase transition of the A_1 and A_2 parameters as a function of pump power, compared to the reflectivity at two delays. Both parameters show an initial linear decrease in intensity, followed by saturation behaviour above a critical fluence $I_c = 0.58\,\mathrm{mJ\,cm^{-2}}$ and saturating when the pump fluence is over $1\,\mathrm{mJ\,cm^{-1}}$.

The time taken to reach equilibrium between the different and the phonon modes could not be resolved within the 8 ps of the measured signal and is represented by the constant C.

The amplitude of the signal is found to vary non-linearly with pump power. At low pump fluence, A_1 and A_2, which represent the fast and the slow dynamics respectively, responded in a linear fashion, however, for higher pump intensities the signal grows rapidly and saturates. This power dependence is indicative of a photo-induced phase transition [21, 84] and indicates the formation of the metallic state. Figure 4.5 plots the parameters A_1 and A_2 as a function of pump power compared to the reflectivity at t=0 and at 1 ps delay. The dashed lines are fits to the saturation equation,

$$A(I) = \alpha(1 + (1 - \frac{I - I_c}{I_s - I_c})^{-1}),$$

where I is the pump fluence, I_c is the critical pump fluence, i.e. the fluence at which the non-linear response takes effect and I_s is the saturation pump fluence.

As both parameters show the same power dependence, the Mott state is reduced very rapidly, within the resolution of the coarse measurements. The critical pump fluence was

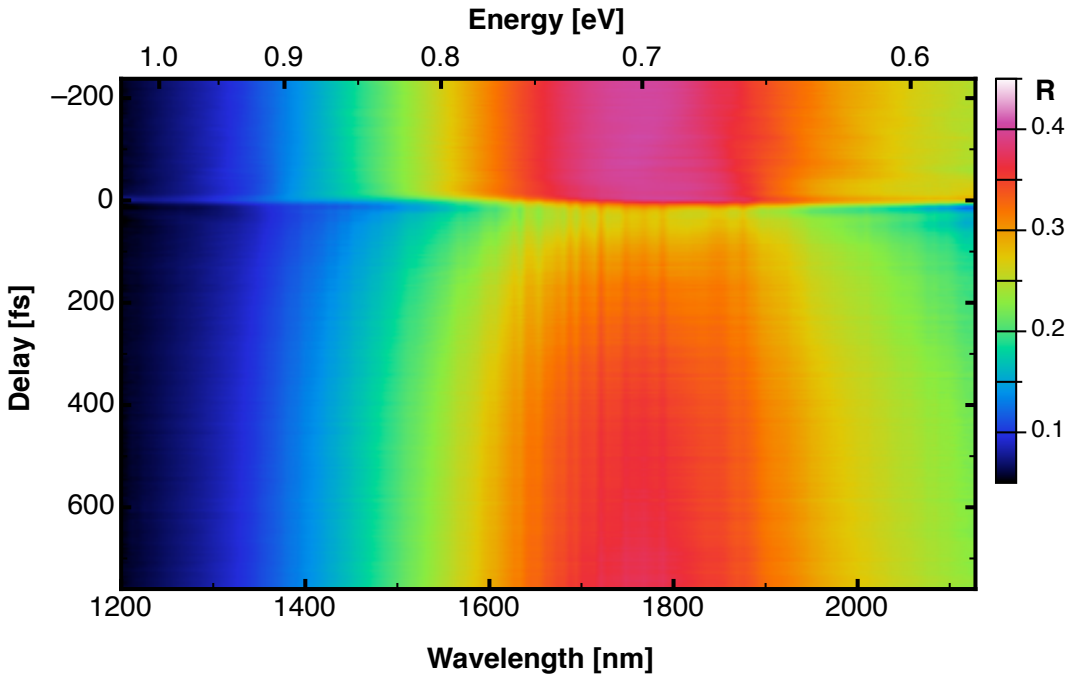

Figure 4.6: A false colour plot of the transient change in reflectivity at the Mott transition as a function of delay and probe wavelength.

found to be $0.58\,\mathrm{mJ\,cm^{-2}}$ which corresponds to photo-excitation of approximately 8% of the ET molecules. The signal saturates with a pump fluence of $1\,\mathrm{mJ\,cm^{-2}}$ corresponding to the excitation of 14% of the ET molecules. This value is in good agreement with theoretical and experimental expectations [80, 81].

4.3.3 Response of the Mott gap

In order to probe the response of the Mott gap in more detail, the change in reflectivity was measured as a function of wavelength and with a high temporal and spectral resolution (figure 4.6). Measuring the change in reflectivity with full spectral resolution allows greater insight into the processes that occur during the collapse of the Mott gap. The response of the Mott gap can be summarized as: a prompt drop in reflectivity at all wavelengths, a shift in spectral weight and a gradual recovery of the ground state.

The spectral response can be integrated over the measured wavelengths in order to retrieve the change in reflectivity as measured in section 4.3.2; this is shown in figure 4.7 together with the response at two wavelengths. The change in reflectivity at different wavelengths represents

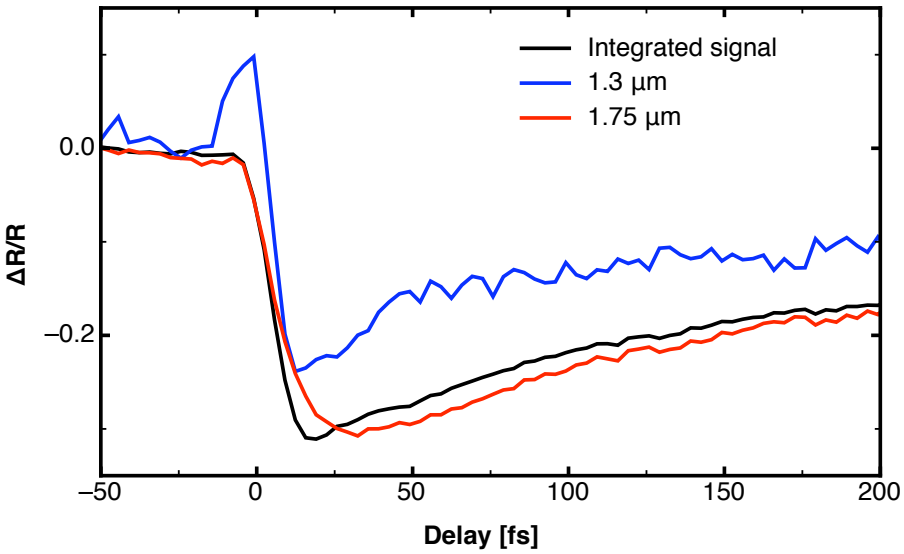

Figure 4.7: The transient response of the Mott gap when the frequency resolved signal is spectrally integrated and for two wavelengths, 1.3 μm (0.96 eV) corresponding to the blue edge of the Mott gap and 1.75 μm corresponding to the peak of the Mott gap.

different dynamics which are lost when the signal is integrated. The signal at 1.3 μm, 0.96 eV, corresponds to the blue edge of the Mott gap. This wavelength is particularly sensitive to changes due to shifts in the gap energy. It shows a very fast dynamic during the presence of the pump pulse, consisting of a rapid increase and then decrease of the reflectivity, suggesting a possible shifting or broadening/narrowing of the Mott gap during the laser pulse. The data at 1.75 μm, which corresponds to the peak of the Mott gap, follows the integrated signal more closely. As the relative change in the reflectivity at 1.3 μm and 1.75 μm are not the same magnitude, the collapse of the Mott gap is not just to a simple reduction in oscillator strength.

The line shape of the reflectivity can be obtained by taking line-outs of figure 4.6. Four line-outs at different pump-probe delays are shown in figure 4.8. These spectra reveal that, at zero time delay, i.ein the presence of the pump pulse, the peak of the reflectivity is red-shifted by 27 nm or 11 meV towards lower energies. The gap then rapidly collapses and shifts back towards higher energies. As the Mott gap recovers, a secondary shoulder on the low energy side of the Mott gap can be seen to emerge and fade.

Figure 4.9a shows an enlarged region of the transient reflectivity plotted in figure 4.6.

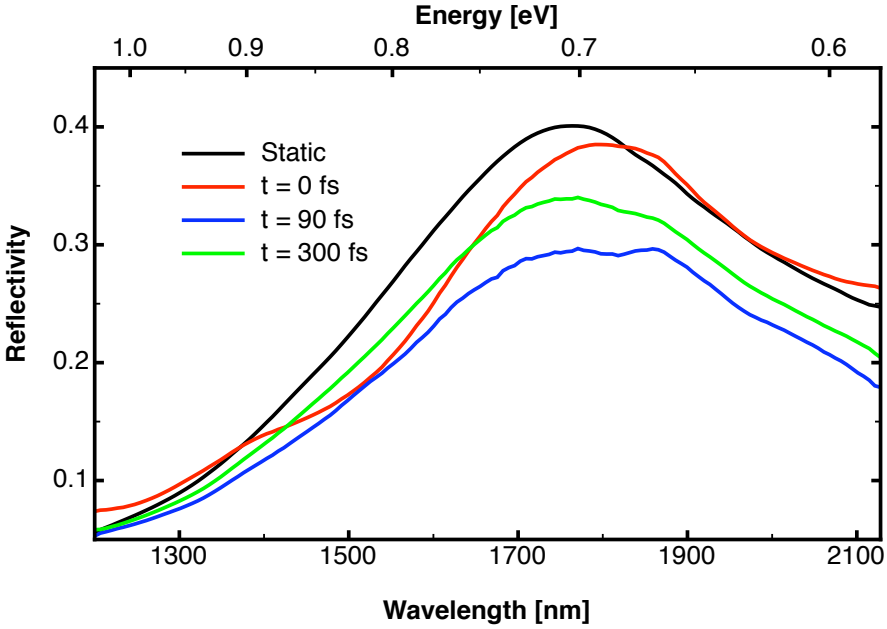

Figure 4.8: Static and transient reflectivity spectra of the Mott gap, at 0, 90 and 300 fs delays.

The data has been normalized for each time step in order to emphasize the intensity of the secondary peak. The secondary peak occurs at approximately 1860 nm (0.67 eV) in the reflectivity spectrum and is roughly constant during the relaxation process.

Figure 4.9b shows the time dependence of the width of the Mott peak[†]. Whilst the laser is in the material, there is a significant narrowing of the Mott gap, which rapidly relaxes after the pump pulse leaves the material and results in a 20 nm, 0.1 meV, broader peak, and decays to back to the original width with a decay constant of 110 fs.

Figure 4.9c plots the wavelength at which the reflectivity reaches half the maximum value from the blue edge of the peak. This is a measure of the shift of the reflection peak. Again, when the pump pulse is in the material there is a large red-shift in the peak position (lower energy). After the pulse has left the material, the peak has blue shifted by 15 nm before a rapid recovery to the equilibrium position.

[†]The width is measured by subtracting the wavelength at which the reflectivity is at half the maximum value, on the high energy side of the spectrum, from the peak reflectivity wavelength. The full width cannot be measured as the reflection peak is asymmetric and there is insufficient probing intensity to measure the lower energy region of the spectrum.

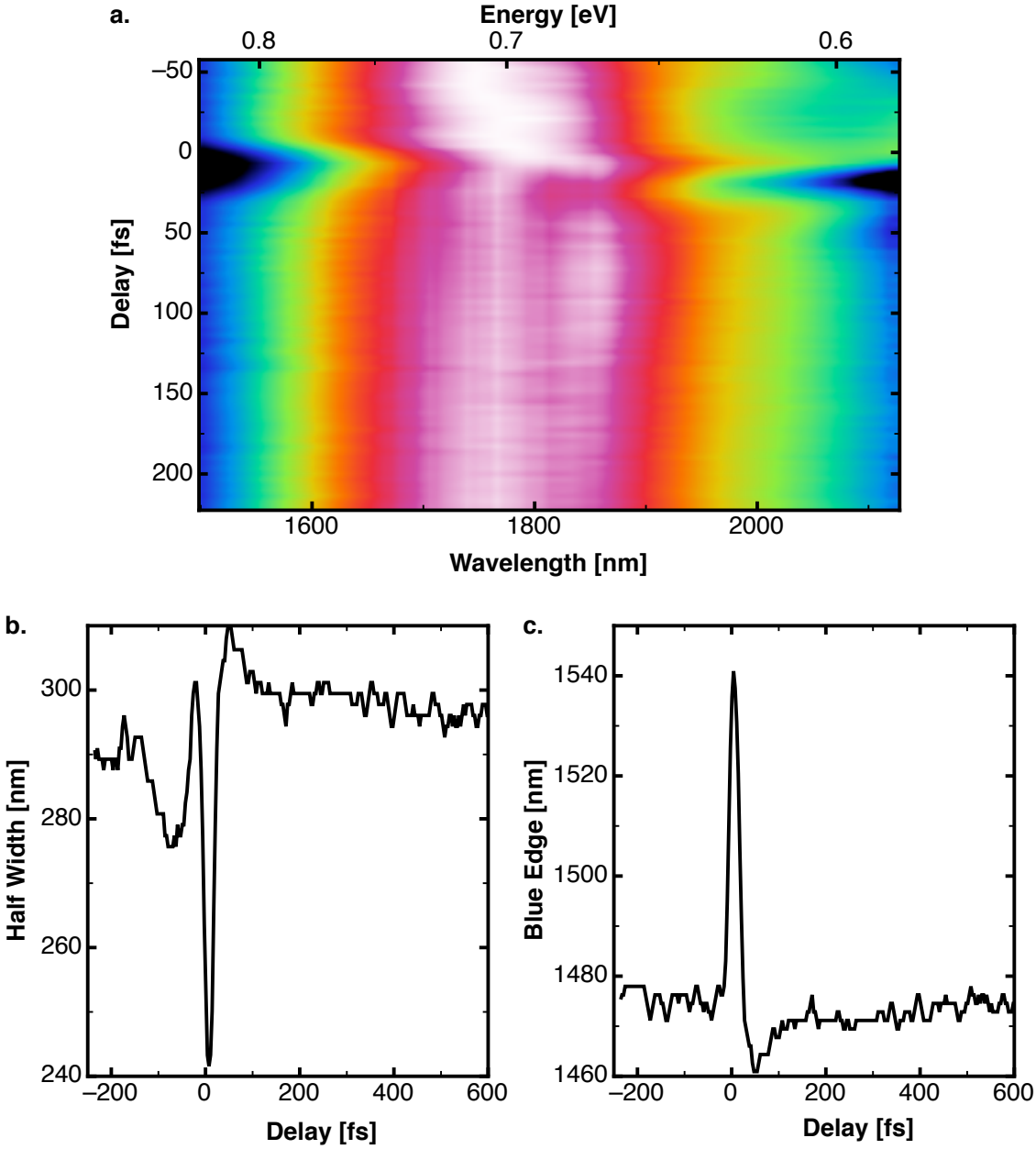

Figure 4.9: a. false colour plot of the transient change in reflectivity at the Mott gap as a function of delay and probe wavelength. The measured signal has been normalized to the maximum value at each delay. b. The half-width of the Mott gap. c. The position of the rising edge of the Mott gap.

[eV]	A	ω_0	γ
1	0.653	3.686	0.669
2	0.703	0.737	0.456
3	0.765	0.675	0.103
4	4.405	3.479	3.771

Table 4.2: Fitting parameters for the dielectric function of ET-F_2TCNQ

4.4 Fitting the optical properties of the Mott gap

Interpretation of the reflectivity is made difficult because it is a non-linear function of more fundamental material properties, such as the dielectric function and optical conductivity. The reflectance of a material at normal incidence is given by Fresnel formula as,

$$R(\omega) = \left| \frac{1 - \sqrt{\epsilon_r(\omega)}}{1 + \sqrt{\epsilon_r(\omega)}} \right|^2 , \tag{4.5}$$

where $\epsilon_r(\omega)$ is the complex dielectric function of the material.

For a set of N uncoupled harmonic oscillators, the complex dielectric function can be expressed as a sum of Lorentzian line shapes [85],

$$\frac{\epsilon_r(\omega)}{\epsilon_0} = 1 + \sum_i^N \frac{A_i^2}{\omega_{0i}^2 - \omega^2 - i\gamma_i\omega}, \tag{4.6}$$

where A_i is the oscillator strength, ω_{0i} is the natural frequency of the resonance and γ_i is the damping constant.

Equations 4.5 and 4.6 were used to fit the static reflectivity over a wide range of energies (0.4-4.9 eV). In order to provide a good fit, four independent oscillators were required and the fitted parameters are shown in table 4.2. The measured and fitted reflectivity are shown in figure 4.10a, together with the real part of the calculated complex dielectric function in figure 4.10b. The optical conductivity, which is defined as $\sigma(\omega) \propto \omega\Im(\epsilon_r(\omega))$, is shown in figure 4.10c.

From table 4.2 there is a clear resonance corresponding to the Mott gap at 0.675 eV (Oscillator 3). This oscillator has a large amplitude the smallest damping constant, and is the oscillator primarily responsible for the large, sharp, peak in the reflectivity. As the excitation occurs at the Mott gap, it is assumed that the pump pulse affects this oscillator

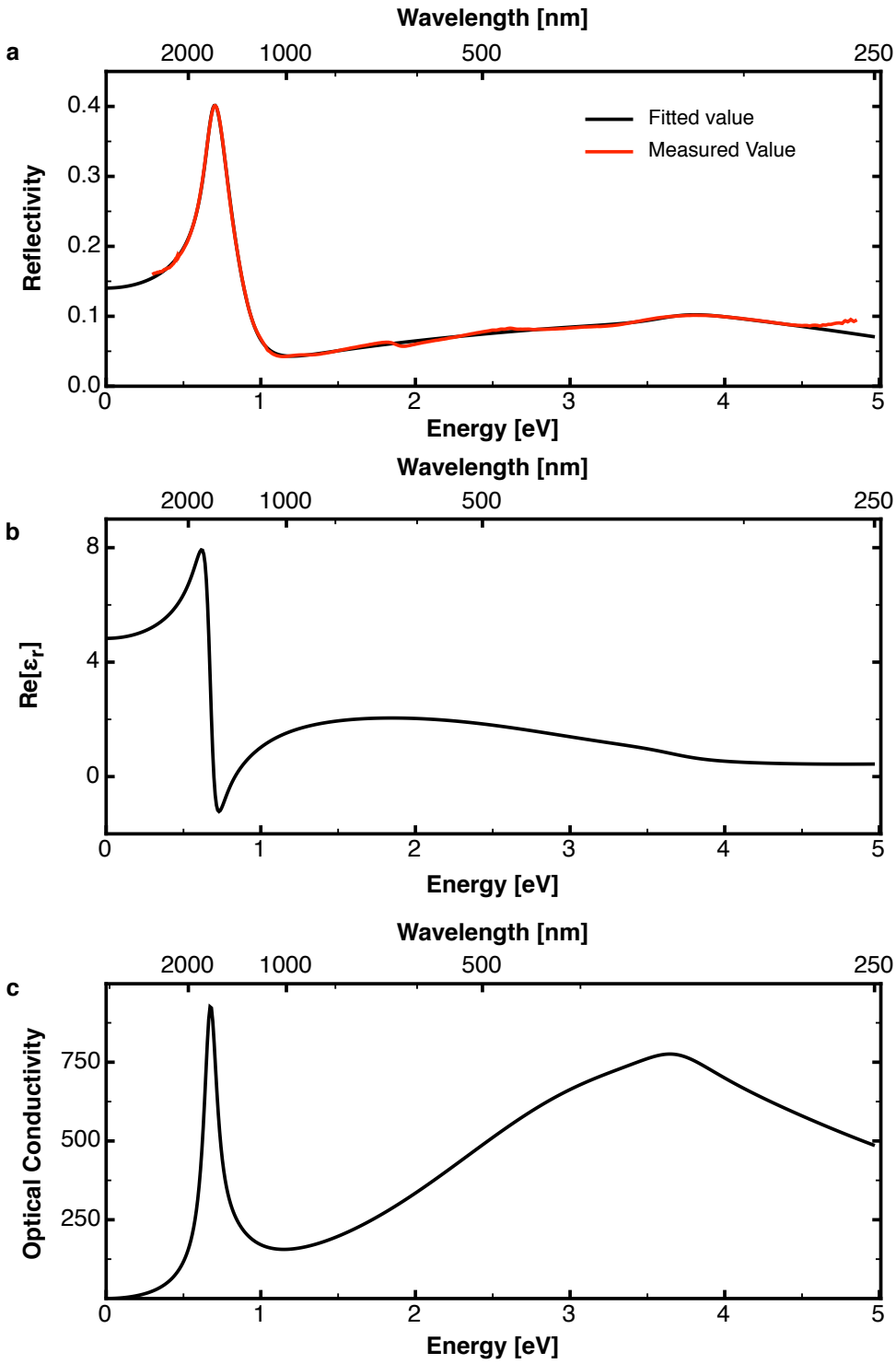

Figure 4.10: The reflectivity and other optical properties of ET-F_2TCNQ. a. The static reflectivity and the fitted reflectivity from equations 4.5 and 4.6. b. The real dielectric constant. c. The optical conductivity

the most. Therefore, in order to fit the time dependent part of the reflectivity over the range 1200 nm-2100 nm, the 'Mott peak', with parameters A_3, ω_{03} and γ_3, are allowed to vary as a function of time, whilst the other peaks are assumed to be unaffected. It is not possible to include time dependent effects at higher and lower photon energy, due to the limited range of the measured spectrum and it is assumed that the changes induced at lower and higher spectra regions only have a small contribution to the signal at the Mott gap.

From figure 4.9 it is clear that, after photo-excitation, two peaks exist in the reflectivity spectrum. Therefore, to simulate the time dependent reflectivity correctly, an additional 'excited-state peak' was required. The fitted reflectivity, for two temporally varying, independent oscillators, is shown in figure 4.11a. The relative error of the fit, which is defined as $R_{\text{fit}}/R_{\text{measured}} - 1$, is shown in figure 4.11b. The biggest error is found at the fringes of the measured spectrum and at time zero, where coherence effects between the pump and probe contribute to the signal which are not included in the fit. In general the fit is very good, with the average relative error $<0.5\%$.

The time dependence of the Mott peak and the excited-state peak parameters are plotted in figure 4.12. The fitting confirms the conclusions drawn from the qualitative analysis of the reflectivity data shown in figure 4.9. The resonant frequency of the gap, shows a prompt red shift to lower energies while the pulse is in the material, before moving to a blue-shifted state from which the equilibrium recovers. The damping rate, γ, of the Mott gap also increases after photo-excitation, which is responsible for the observed increase in the half-width.

The decrease in amplitude, or loss in spectral weight, of the Mott gap can be explained by a reduction in the number of localized electrons that are responsible for providing the response at this frequency. The spectral weight that these electrons provide is mostly likely transfered to the DC and low frequency conductivity which is not measured here. The increase in damping rate is also expected as there can be more collisions between the localized and delocalized electrons. The observed shifts in the resonant frequency of the Mott transition have a more subtle origin and will be discussed in light of the quantum mechanical model discussed in the next section.

The secondary peak emerges very rapidly and appears to remain stable, with a constant amplitude, for approximately 200 fs before beginning to decay slowly. The resonance is very narrow, experiencing a damping rate that is half of the Mott peak.

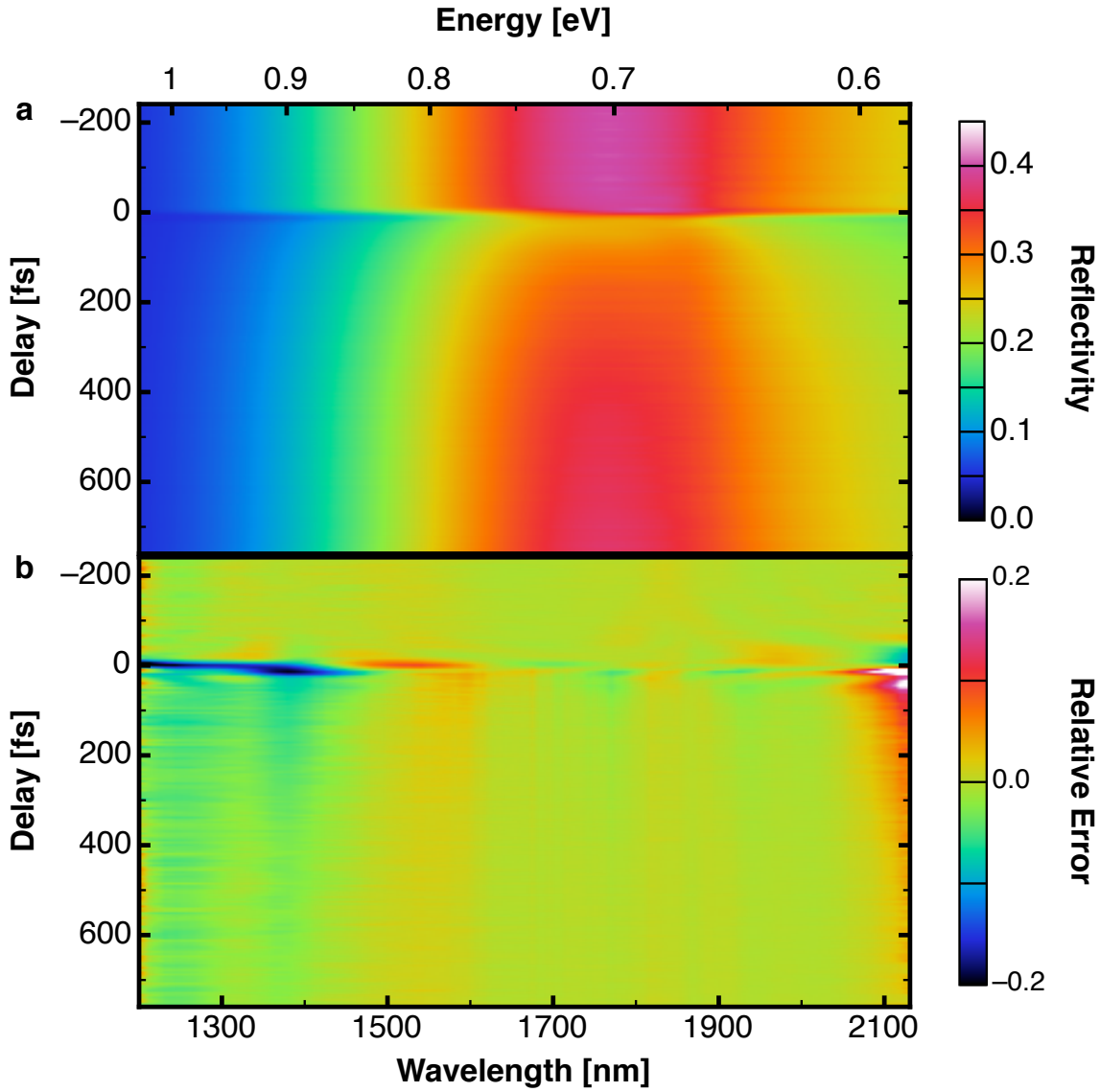

Figure 4.11: a. Time dependent fitting of the reflectivity. b. Relative error of the fit

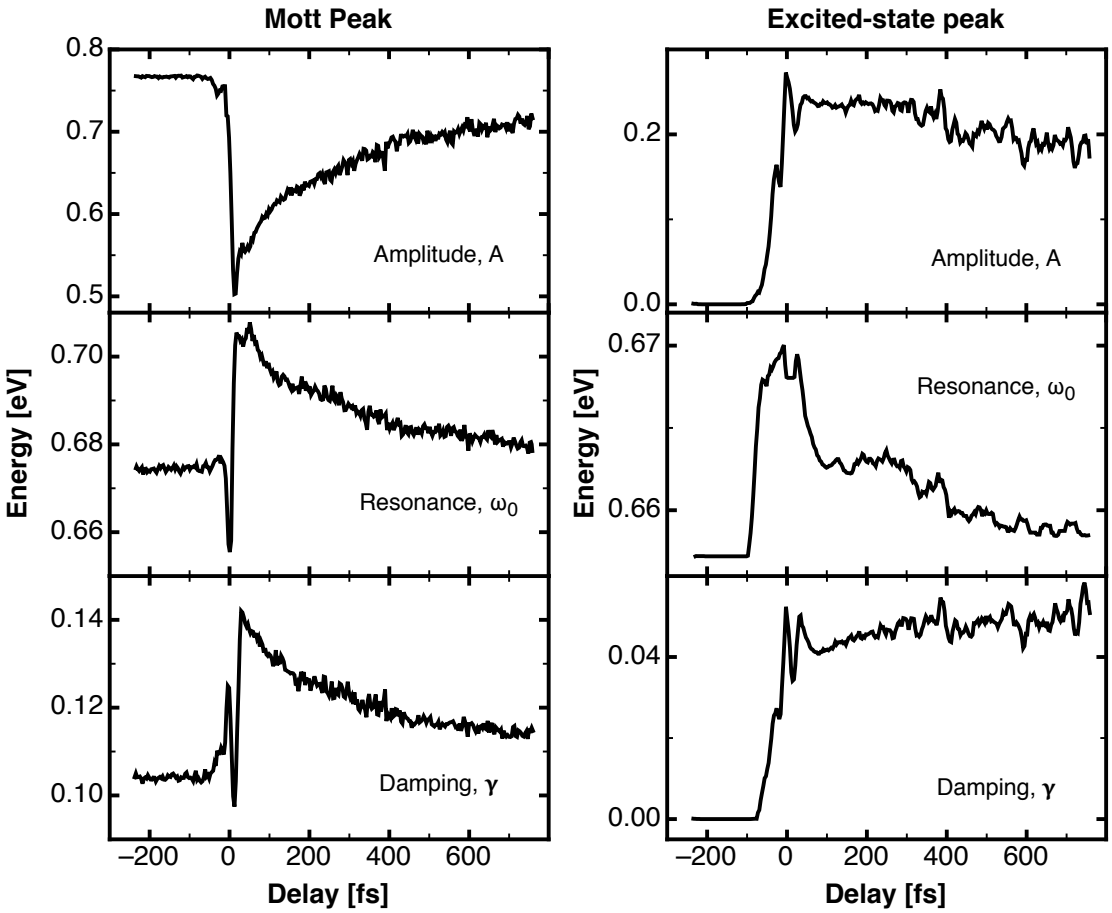

Figure 4.12: Time evolution of the Mott gap and the excited-state peak.

4.4.1 Quantum simulation of the Mott dynamics

The one dimensional nature of the ET-F_2TCNQ means that exact techniques can be used to solve the Hubbard Hamiltonian[‡]. The Hubbard Hamiltonian for a 1D material with nearest neighbour electron-hopping, t, onsite U and nearest neighbour electron-electron interaction, V, is,

$$H = -t \sum_{l,\sigma} \left(c^{\dagger}_{l,\sigma} c_{l+1,\sigma} + c^{\dagger}_{l+1,\sigma} c_{l,\sigma} \right) + U \sum_{l} n_{l,\uparrow} n_{l,\downarrow} + V \sum_{l} n_l n_{l+1}, \tag{4.7}$$

where $c^{\dagger}_{l,\sigma}$ is the creation operator for an electron at site l with spin σ, $n_{l,\sigma} = c^{\dagger}_{l,\sigma} c_{l,\sigma}$ is the number of electrons with spin σ at lattice site l and $n_l = n_{l\uparrow} + n_{l,\downarrow}$. The V term represents an attractive interaction between a site with two electrons and a site with no electrons and a repulsive interaction between two sites with two electrons, or two holes, each

The optical conductivity for angular frequencies $\omega > 0$ is defined as [86],

$$\sigma(\omega) = \frac{\pi e^2}{a} \sum_{\nu \neq 0} \frac{|\langle \psi_0 | j | \psi_\nu \rangle|^2}{\omega_\nu - \omega_0} \delta(\omega - \omega_\nu + \omega_0), \tag{4.8}$$

where e is the charge of the electron and a is the lattice spacing. $|\psi_\nu\rangle$ are the eigenfunctions of equation 4.7 with eigenvales ω_ν. j is the current operator, which is defined as $j = it \sum_{l,\sigma} (c^{\dagger}_{l,\sigma} c_{l+1,\sigma} - c^{\dagger}_{l+1,\sigma} c_{l,\sigma})$.

Therefore, by solving equations 4.7 and 4.8, the optical conductivity can be calculated for the ground state of the system. By varying U, t and V the model can be fitted to the ground state optical conductivity of ET-F_2TCNQ shown in figure 4.10.

The simulations considered here are for a 1D Mott insulator with 10 lattice sites. Even with this reduction in complexity, equation 4.7 cannot be solved directly. Instead, an initial state that matches the materials properties at room temperature was considered. At room temperature, the initial state was postulated to be

$$\rho_0 = \frac{1}{2^N} \sum_{\sigma_T} |\psi_{\sigma_T}\rangle \langle \psi_{\sigma_T}|, \tag{4.9}$$

where $N = 10$ is the number of lattice sites and $|\psi_{\sigma_T}\rangle$ are the set of wavefunctions corresponding to one electron localized on each lattice site with the total spin state σ_T. This state corresponds to the localized Mott insulator with no correlations between the spin degree of freedom. As $T_N = 30\,\mathrm{K}$ in ET-F_2TCNQ, this is a good approximation to the actual ground state.

[‡]Simulations were performed by Dr. Steven Clark, Clarendon Laboratory, Oxford University.

The optical conductivity is not calculated from equation 4.8 directly, instead the current-current correlation function,

$$c_{jj}(\tau) = \mathrm{tr}[\rho j(\tau) j(0)]\theta(\tau), \tag{4.10}$$

is calculated, where $j(\tau) = \exp(iH\tau) j \exp(-iH\tau)$ and $\theta(\tau)$ is the step function. The current-current correlation function is related to the optical conductivity by [87]

$$\sigma(\omega) = \frac{e^2}{a} \frac{\Re\{c_{jj}(\omega)\}}{\omega}, \tag{4.11}$$

where $c_{jj}(\omega)$ is the Fourier transform of $c_{jj}(\tau)$. This form is, computationally, significantly easier to solve.

As equation 4.7 is for an idealized material of point-like lattice sites, high energy excitations, such as molecular vibrations, are not included. Therefore it is unable to calculate the high energy optical conductivity of the material. In order for a fairer comparison, the simulated optical conductivity is compared to the 'reduced' optical conductivity, σ_R.

The optical conductivity is related to the complex dielectric function by $\sigma \propto \omega \Im(\epsilon_r)$. Therefore, by restricting ϵ_r to contain only the resonance responsible for the Mott gap (oscillator 3 in table 4.2) and the excited-state resonance, the reduced optical conductivity, can be obtained.

The result of the fit is shown in the upper left plot of figure 4.13, which shows the static reduced optical conductivity and the result of the simulated optical conductivity. The best fit was found for $U = 0.82\,\mathrm{eV}$, $V = 101\,\mathrm{meV}$ and $t = 51\,\mathrm{meV}$. The V term in equation 4.7 was found to be necessary to reproduce the required line-shape of the optical conductivity.

The dynamics of the optical conductivity are simulated by considering the types of states excited by the laser, and not by modeling the interaction of an electric field on the ground state directly. When the pump laser excites the material, electrons are transfered across the Mott gap. As these electrons are initially created by a spatially coherent laser, they will retain that coherence. Therefore, the excited state appearing at the earliest times considered is one in which a single electron is excited to a neighbouring lattice site and is delocalized (i.e. in a coherent superposition) across all lattice sites, whist the unexcited electrons remain in a spin-mixed background. This state is represented as

$$\rho_D = \frac{1}{2(N-1)} \sum_{l=1}^{N-1} \sum_{\sigma} \left(c^{\dagger}_{l,\sigma} c_{l+1,\sigma} + c^{\dagger}_{l+1,\sigma} c_{l,\sigma} \right) \rho_0. \tag{4.12}$$

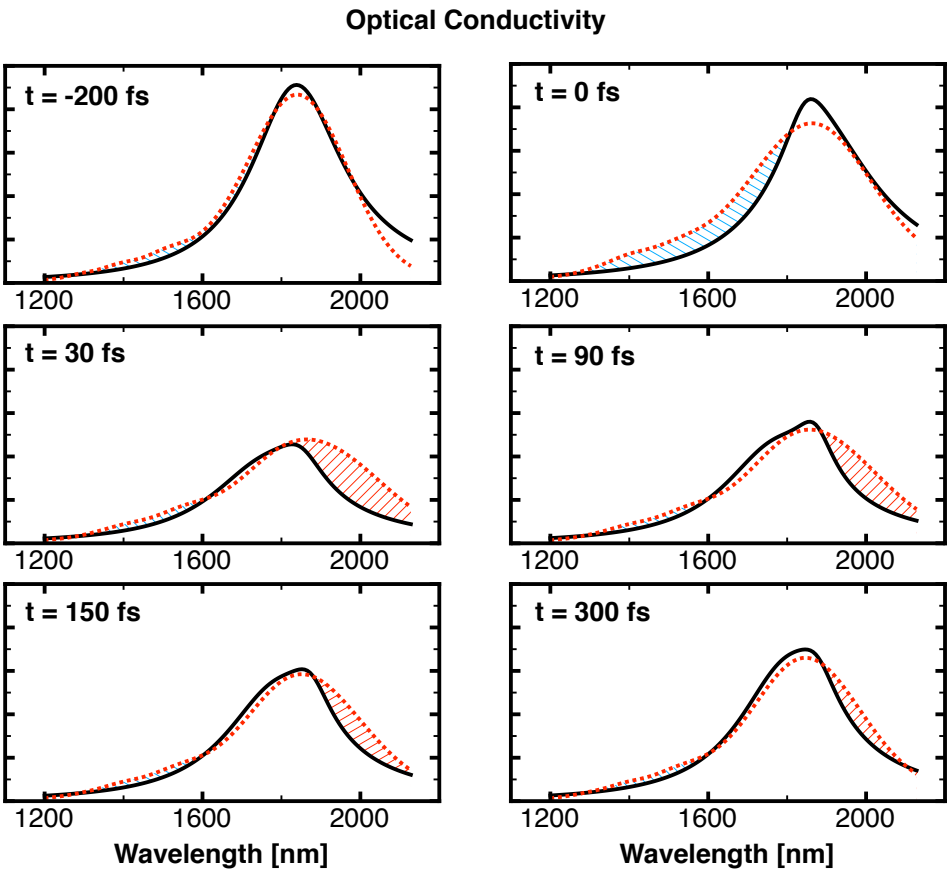

Figure 4.13: The optical conductivity of the Mott gap as a function of time. Black solid lines are the reduced optical conductivity σ_R. Red dotted lines are the simulated optical conductivity obtained from the Hubbard Hamiltonian in equation 4.7.

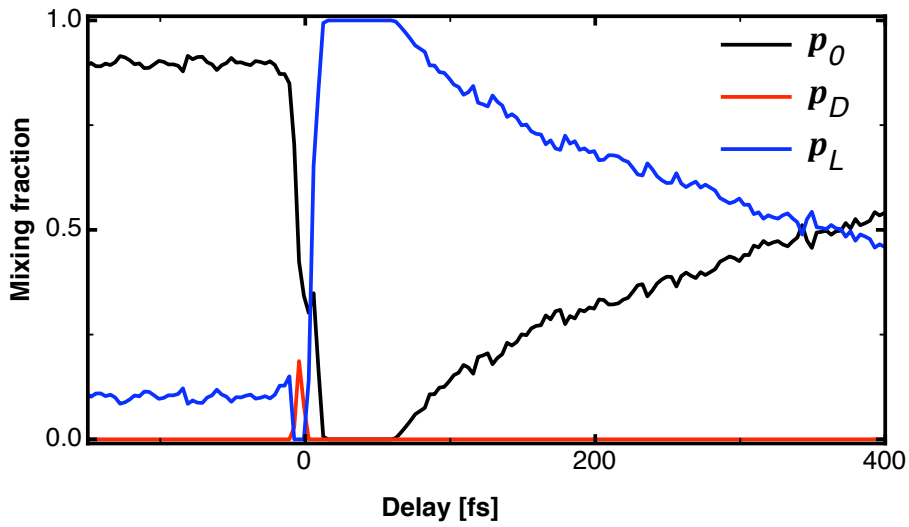

Figure 4.14: The time dependence of the probabilities of state ρ.

The coherence in the solid state will be rapidly lost due to scattering events, reducing the state to a electron and hole located on a specific site. Therefore, after some time, the state will be reduced to a statistical mix of single localized electron hole pairs. This state is represented as

$$\rho_L = \frac{1}{2}\sum_{\sigma}\left(c^{\dagger}_{l,\sigma}c_{l+1,\sigma} + c^{\dagger}_{l+1,\sigma}c_{l,\sigma}\right)\rho_0. \tag{4.13}$$

The optical conductivities associated with ρ_D and ρ_L can be calculated using equation 4.11.

The state of the system as a function of time is modeled as

$$\rho(t) = p_0(t)\rho_0 + p_D(t)\rho_D + p_L(t)\rho_L, \tag{4.14}$$

where $p_0 + p_D + p_L = 1$, are the fraction of the material in the three states. This results in an optical conductivity that is a mixture arising from the three considered states.

Figure 4.13 compares the reduced optical conductivity to the calculated value at several times. The general features are captured remarkably well by the model, suggesting that the the choice of states are an accurate representation of the system. The model captures the redshift observed when the laser pulse is in the material, followed by the rapid decrease in spectral weight and subsequent recovery. In general, at early times the simulated line shape of the resonance is much broader that the measured quantity, suggesting the effects of additional phenomena that are not included in this model.

Further insight can be obtained by examining the time evolution of the state $\rho(t)$. Figure 4.14 shows the amount of each state present in ET-F_2TCNQ as a function of time. ρ_D shows a sharp spike at $t = 0$, suggesting that the coherent state is only maintained whist the laser is in the material and it is this state that is responsible for the red-shift in the optical conductivity. There is also a large drop in the fully localized state, which is replaced by the localized electron-hole state. This state is responsible for the large decrease in spectral weight at the Mott gap.

The features at early time delays are not captured as well, specifically the width of the optical conductivity, its blue shift at later times, and the emergence of a narrow secondary resonance feature. These are most likely due to states that have not been considered. For example, the electron and hole pairs are bound to adjacent lattice sites, which would not be the case in the metallic state, where they would be free to move throughout the material. In addition, the high photo-excitation densities studied here could also result in interactions between pairs of electron-hole pairs, as only one electron is excited, these effects will not feature in this model, but could be responsible for the formation of new resonances.

4.5 Summary

This chapter has investigated the photo-induced insulator-metal phase transition in the one dimensional Mott insulator ET-F_2TCNQ. The phase transition shows non-linear changes in the optical properties when approximately 10 % of ET molecules are excited. By measuring the changes in reflectivity of the Mott gap with both high temporal and spectral resolution, the quantum response of the material could be observed and modeled.

After photo-excitation, a drastic decrease in spectral weight at the Mott gap resonance is observed, together with a dynamical shift and a broadening. In addition, a secondary resonance appears at lower photon energies. The main dynamics could be replicated by a quantum mechanical model that considered three states. The ground state of the system, a delocalized electron-hole pair, created from the coherence of the laser pulse, and an incoherent localized electron-hole pair. The red-shift of the Mott gap was attributed to the delocalized state, whereas the decrease in spectral weight was associated with the formation of the electron-hole pairs.

Extending these measurements to even shorter timescales could reveal the timescale on

which the coherence between the initial photo-excited state and the localized state is lost.

Chapter 5

Magneto-elastic dynamics of $LaMnO_3$

5.1 Introduction

To date, ultrafast measurements of manganites have focused on the doped compounds. Doped manganites often exhibit photo-induced phase transitions such as insulator-metal [24, 88], melting of charge and orbital order [89] and photo-induced ferromagnetism [75]. However, neither the ground state properties or the mechanisms behind the photo-induced phase transitions are understood well.

In order to gain insight into the photo-induced dynamics in manganites, this chapter investigates the response of $LaMnO_3$, the parent compound for many manganites. The static properties of $LaMnO_3$, such as the structure and optical properties, have been extensively studied and are relatively well characterized. $LaMnO_3$ retains the strong couplings between the multiple order parameters found in the doped manganites, whilst removing the additional complications associated with mixed-valence manganese ions and inhomogeneity associated with phase separation. Therefore, the physics controlling the photo-raction of $LaMnO_3$ will be applicable to the doped manganites.

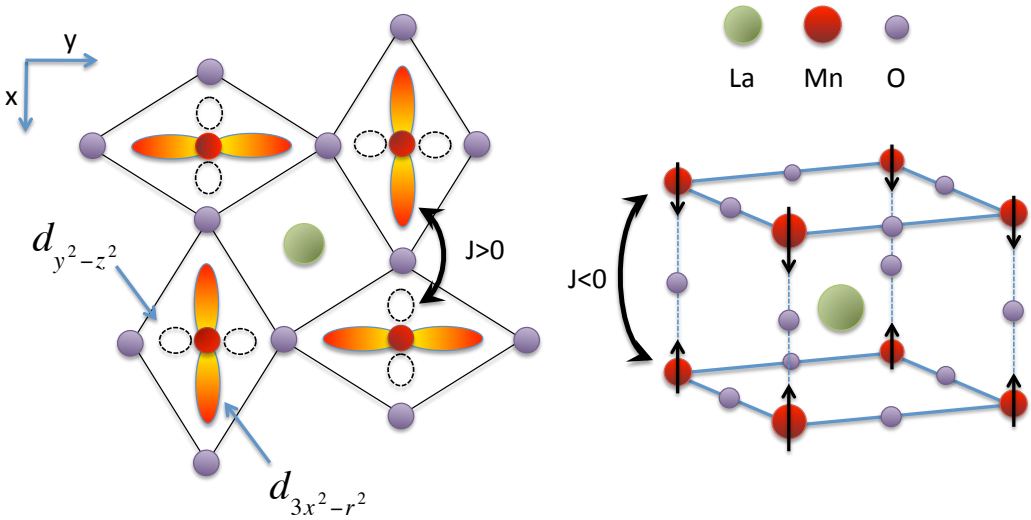

Figure 5.1: The orbital and structural ordering in $LaMnO_3$ with ferromagnetic ordering in the ab plane (left) and anti-ferromagnetic ordering along the c axis (right). The image is orientated such that the crystal's a and b axes are along the x and y directions respectively.

5.2 Static properties of $LaMnO_3$

$LaMnO_3$ is a half-filled Mott insulator with a cubic perovskite structure. At $T_{JT} \approx 780\,K$ a cooperative static Jahn-Teller distortion of the oxygen octahedra within the ab-planes lifts the degeneracy of the e_g levels. This gives rise to a staggered orbital and structural pattern in which the direction along which the Jahn-Teller distortion and orbital points alternates, resulting in an ordered array of Mn-O short and Mn-O long bonds as shown in the left of figure 5.1. Below $T_N = 140\,K$, $LaMnO_3$ undergoes a second order phase transition to an A-type anti-ferromagnet, which consists of ferromagnetically aligned spins in the ab-plane, which are anti-ferromagnetically coupled along the c-axis (figure 5.1 right) [90, 91].

The magnetic and structural properties of $LaMnO_3$ can be understood with the Goodenough-Kanamori (GK) rules, introduced in chapter 2. The Jahn-Teller distortion reduces the degeneracy of the e_g levels, giving rise to a lower energy, occupied, $d_{3x^2-r^2}/d_{3y^2-r^2}$ level and an unoccupied, higher energy, $d_{y^2-z^2}/d_{z^2-x^2}$ level. The alternating Jahn-Teller distortion results in half-filled $d_{3x^2-r^2}/d_{3y^2-r^2}$ orbitals overlapping, via the oxygen $2p$ states, with an unoccupied $d_{z^2-x^2}/d_{y^2-z^2}$ orbitals. According to the GK rules, this type of bond gives rise to a ferromagnetic exchange ($J > 0$) between the manganese ions in the ab-plane.

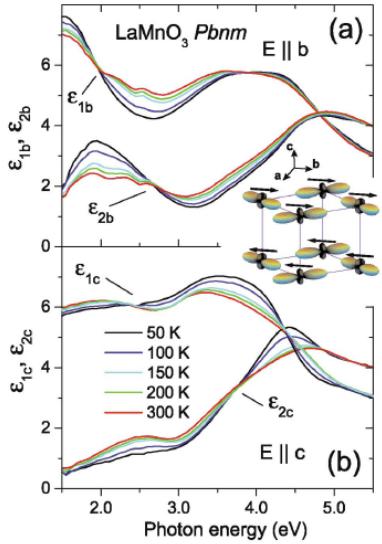

Figure 5.2: The dielectric function of $LaMnO_3$ measured using ellipsometry from 1.5-5.6 eV, taken from ref [92]

Along the c-axis, the dominant bonding is between the t_{2g} orbitals via the oxygen states. As the t_{2g} levels are all half-filled, the exchange interaction between manganese ions in this direction is anti-ferromagnetic ($J < 0$).

5.2.1 Optical Properties

The effects of the orbital and structural ordering can be observed in the temperature dependence of the optical properties of $LaMnO_3$. Large changes in spectral weight are observed on cooling below the Néel temperature, consistent with spin and orbital ordering predicted by the GK rules [93]. The dielectric function as a function of temperature and photon energy for $LaMnO_3$, measured by Kovaleva et al. [92] using the ellipsometry technique, is shown in figure 5.2. From the temperature dependence of the imaginary part of the dielectric function, Kovaleva et al. were able to show that the peak in absorption at $\approx 2\,\mathrm{eV}$, for light polarized along the a/b-axis corresponds to a transition across the Mott gap, i.e. the inter-site transition $2(\mathrm{Mn}^{3+} : t_{2g}^3 e_g^1) \rightarrow \mathrm{Mn}^{4+} : t_{2g}^3, \mathrm{Mn}^{2+} : t_{2g}^3 e_g^2$. The broad peak around 4-5 eV corresponds to the charge transfer (CT) gap, which consists of electronic transitions between the oxygen and manganese ions. The assignment is in agreement with other experimental and theoretical considerations [94, 95].

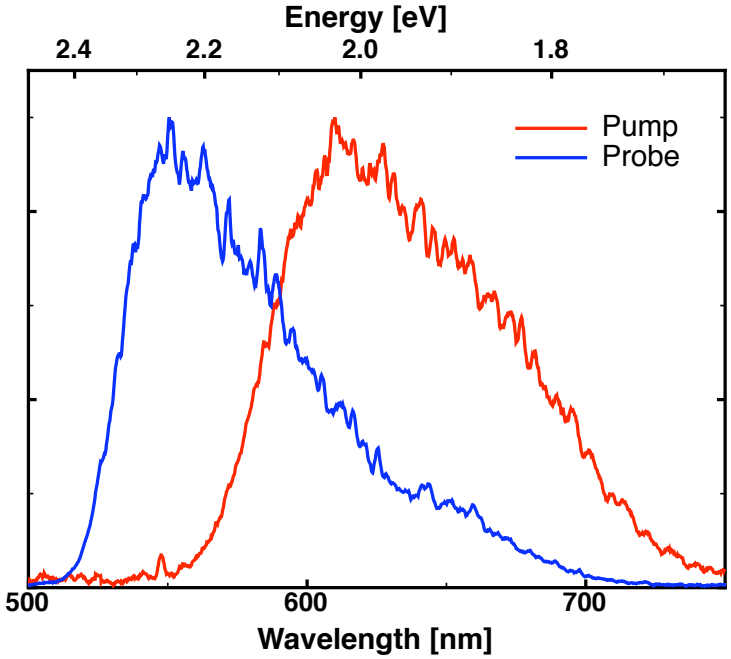

Figure 5.3: The normalized pump and probe spectra produced by two independent non-colinear optical parametric amplifiers.

5.3 Experimental setup

Pump-probe experiments were performed using two visible non-colinear optical parametric amplifiers (NOPAs) which provided short pulses in the spectral region spanned by the Mott gap. The NOPAs were pumped with the second harmonic of an 800 nm (1.55 eV) titanium sapphire laser to generate broad band laser light in the visible region of the spectrum with a 1 kHz repetition rate as described in chapter 3.

The NOPAs were tuned such that the pump laser spectrum was centred at 2 eV, the peak of the Mott transition. The probe energy was detuned to a slightly higher energy of 2.2 eV and the polarization was rotated 90° with respect to the pump beam by a polarization rotating periscope. These actions were taken to reduce interference effects and coherent artifacts induced by interactions between the pump and probe beams when temporally overlapped on the sample. The normalized spectra of both pump and probe beams are shown in Figure 5.3.

The output of both NOPAs was compressed by 18 bounces off doubly chirped mirrors to a duration of approximately 10 fs. The pulse length was measured by an intensity cross correlation detected by two photo absorption in a SiC diode at the position of the sample

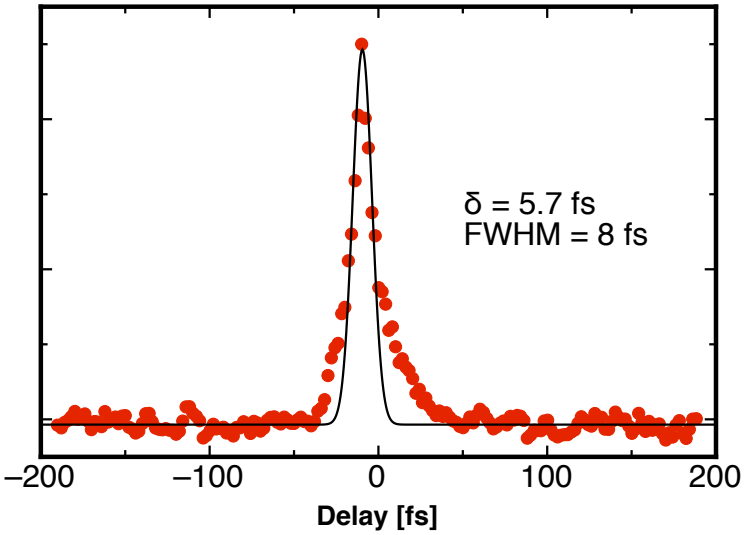

Figure 5.4: Normalized cross correlation between pump and probe with a gaussian fit revealing a time resolution of less than 10 fs.

and is shown in figure 5.4. This measurement defines the time zero position for subsequent measurements. Assuming an identical Gaussian profile to each pulse, the full width half maximum (FWHM) of each pulse is 8 fs.

The experimental layout is sketched in figure 5.5. The pump beam was chopped by a mechanical chopper for lock-in detection of the signal. The beams were focused onto the sample by the same 90° off axis parabola with a 10 cm focal length. This resulted in a spot size of 60 μm at the sample surface as determined by a knife edge measurement. The pump power was 0.8 mW, giving a pump fluence of 6 mJ cm^{-2} at the sample surface.

The $LaMnO_3$ sample was grown using the floating zone technique [96]. The sample was approximately 1 cm in diameter and cut in the *ab*-plane. It was mounted in a liquid nitrogen flow cryostat. The optical entrance was via a 100 μm thick, 10 mm diameter fused silica window. The window was included in the cross-correlation measurement and does not affect the pulse duration. The sample was rotated so that the reflected beam left the cryostat by a larger exit window in order to make the collection and collimation of the reflected beam easier. This resulted in an angle of incidence of $\approx 20°$ relative to the sample normal. The pump beam was *p*-polarized and the probe beam was *s* polarized in order to probe excitations within the *ab*-plane. The reflected beam passed through a polarizer to reduce any scatter from

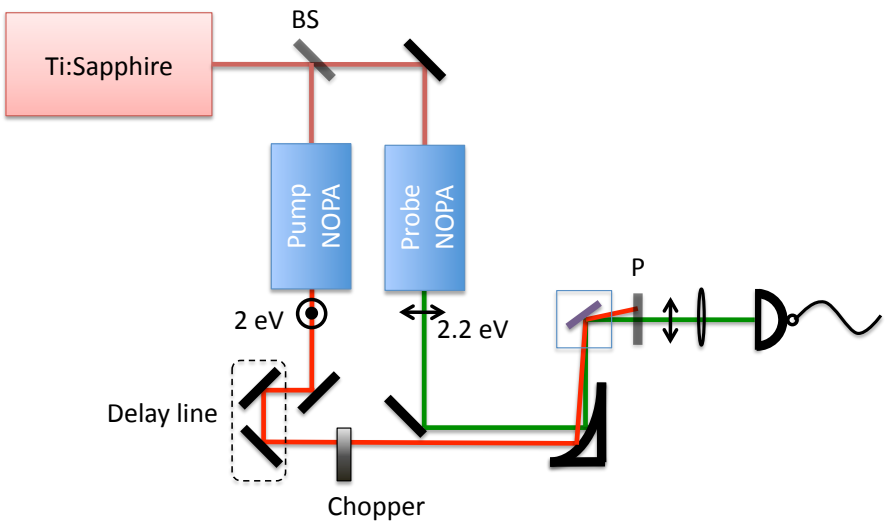

Figure 5.5: Sketch of experimental layout of the pump probe experiment in $LaMnO_3$. BS - beam splitter, P - polarizer. The blue square represents the cryostat containing the $LaMnO_3$ sample.

the pump beam and was focused onto a low bandwidth silicon diode.

5.4 Experimental results

Pump-probe changes in reflectivity were measured as a function of temperature from 80-300 K. Two transient relative change in reflectivity are shown in figure 5.6 measured above (red squares) and below (blue circles) the Néel temperature (T_N=140 K). Both signals consists of a sharp drop in the reflectivity, which decays incoherently back to the equilibrium value, on top of which are large amplitude coherent oscillations.

The slowly decaying, incoherent, background can be fitted with a function of the form,

$$\frac{\Delta R_{inc}(t)}{R} = -\mathrm{erf}(t) \sum_{i=1,2} A_i \exp(-t/\tau_i). \tag{5.1}$$

Where $\mathrm{erf}(t) = \frac{1}{2} + \frac{1}{\sqrt{\pi}} \int_0^t \exp(-t'^2/2\sigma^2)dt'$, represents the rising edge of the signal by the integral of a gaussian of width, σ. The width is set by the pump-probe cross-correlation measurement and is given in figure 5.4 as 5.7 fs. A_i is the amplitude of the incoherent signal at $t = 0$ with a decay constant τ_i. The best fit to the data is found when a bi-exponental decay is used and the fits obtained are shown by the dashed lines in figure 5.6. Figure 5.6

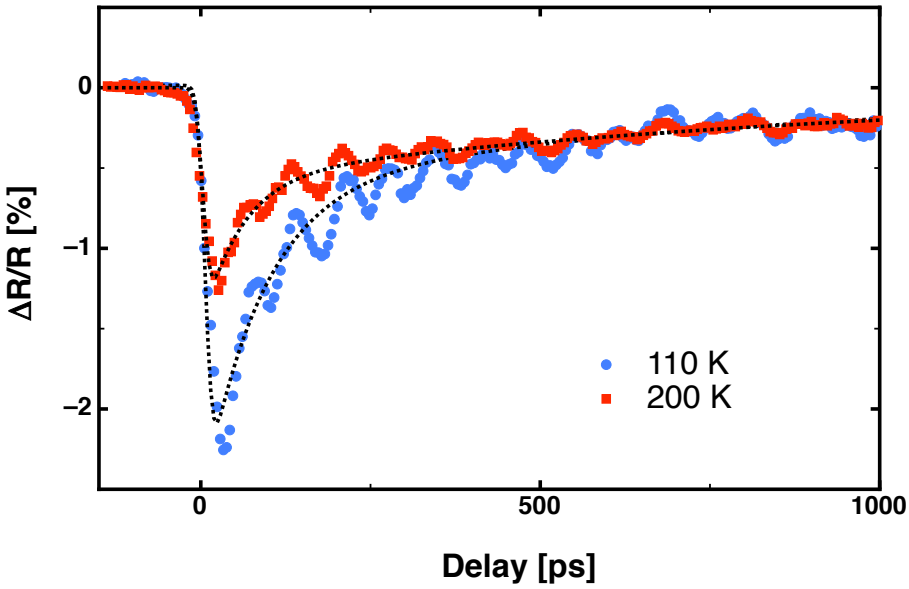

Figure 5.6: Pump-probe changes in reflectivity in $LaMnO_3$ above and below the Néel temperature ($T_N = 140\,\mathrm{K}$) The dotted lines are the fits according to equation 5.1.

clearly shows that the initial, fast dynamics ($i = 1$) are significantly influenced by the initial temperature of the material, whereas the longer term ($t > 500\,\mathrm{fs}$, $i = 2$) slow dynamics are independent of the initial temperature.

Figure 5.7 shows the temperature dependence of the amplitude (A_1) and the decay time (τ_1) of the fast dynamics. Both the amplitude and decay time of the incoherent signal show linear decrease with increasing initial temperature. The dependence of the first decay term on the initial lattice temperature suggests that it can be assigned to electron-phonon thermalization. The electron-phonon thermalization rate $\tau_{\mathrm{el-ph}}$ has an inverse dependance on the number of phonons with which electrons can scatter from. Therefore, increasing the lattice temperature will decrease the thermalization time. For semi-conductors, the amplitude of the electron-phonon scattering signal also depends linearly on the lattice temperature, consistent with the measured temperature dependence of A_1 [97]

The slow dynamics were found to be temperature independent on the timescales measured here. The best fit parameters were $A_2 = (3.4 \pm 0.6) \times 10^{-3}$ and $\tau_2 = 1000 \pm 200\,\mathrm{fs}$. The long decay time of 1 ps means that the slow dynamics are approximately constant on this timescale, which makes temperature effects difficult to observe, however the these dynamics are most

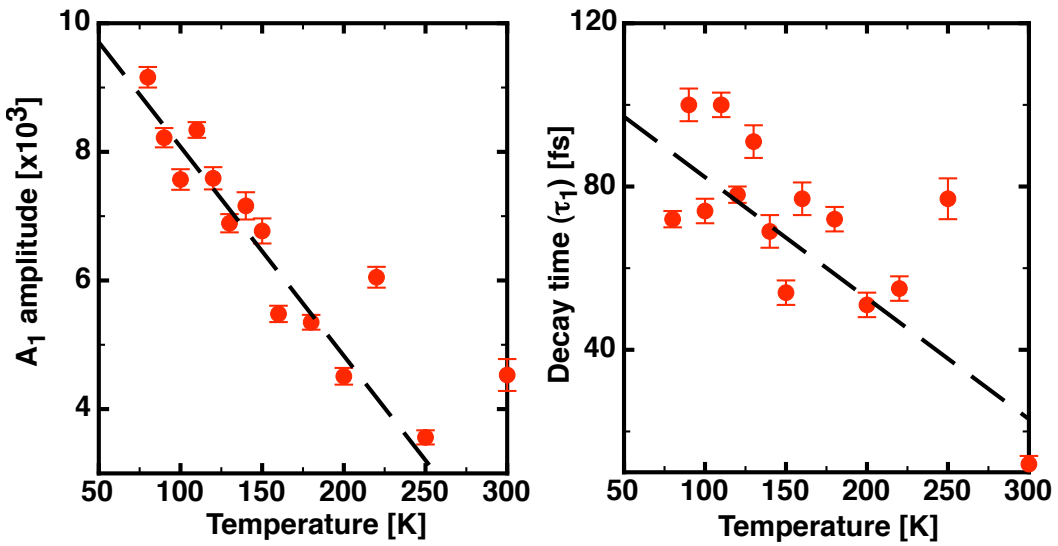

Figure 5.7: The temperature dependance of the electron-phonon thermalization (A_1 and τ_1 parameters from equation 5.1).

likely attributable to electron-hole recombination.

Neither the amplitude nor the decay of either the fast or the slow dynamics shows any discernible discontinuity at the Néel temperature, suggesting that the electron-phonon coupling and electron-hole recombination in $LaMnO_3$ is unaffected by the appearance of magnetic ordering.

The incoherent background can be subtracted from the measured signal to leave the residual coherent oscillations which are shown in figure 5.8. The amplitude of the oscillation increases significantly on cooling. This is most apparent in the Fourier transform of the data, which is shown in figure 5.9. The two predominate frequencies observed are a high frequency 14.9 THz (61.5 meV, 497 cm^{-1}) mode and a lower frequency 8.8 THz (36.3 meV, 293 cm^{-1}) mode. These frequencies remain constant for all temperatures measured.

The observed frequencies are in very good agreement with those measured by Raman scattering. Iliev et al. [98] measured broad peaks in the Raman spectra at 284 cm^{-1} and 493 cm^{-1} and assigned the low energy mode to an out-of-phase rotation of the oxygen octahedra, and the higher energy mode to an out-of-phase bending of the oxygen octahedra.

Krüger et al. [99] used resonant Raman scattering to resolve the scattered spectra in more detail. The same lower energy mode at 284 cm^{-1} was observed. However, the resonance

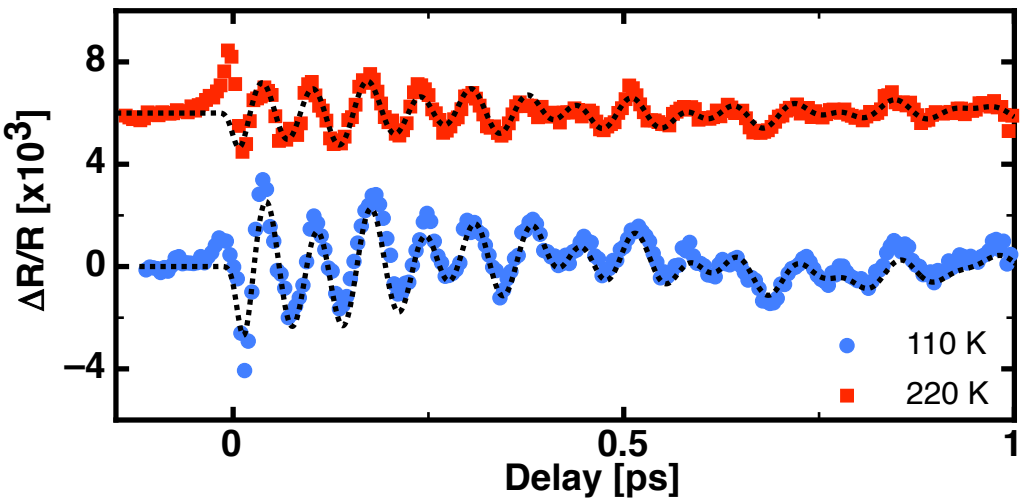

Figure 5.8: The coherent oscillations in the transient reflectivity in $LaMnO_3$ after subtracting the incoherent decay. The high termperature results have been vertically displaced for clarity. Dashed lines are fits obtained using equation 5.2

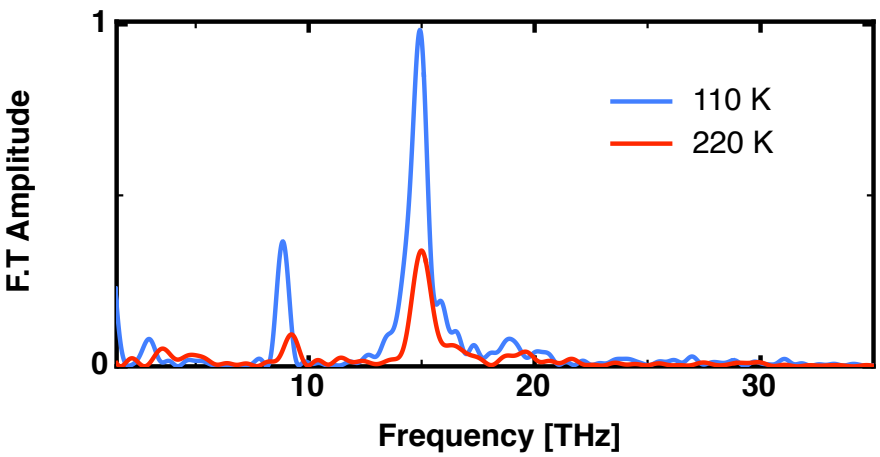

Figure 5.9: Fourier transform of the residual oscillations in $LaMnO_3$ at below (110 K) and above (220 K) the Néel temperature.

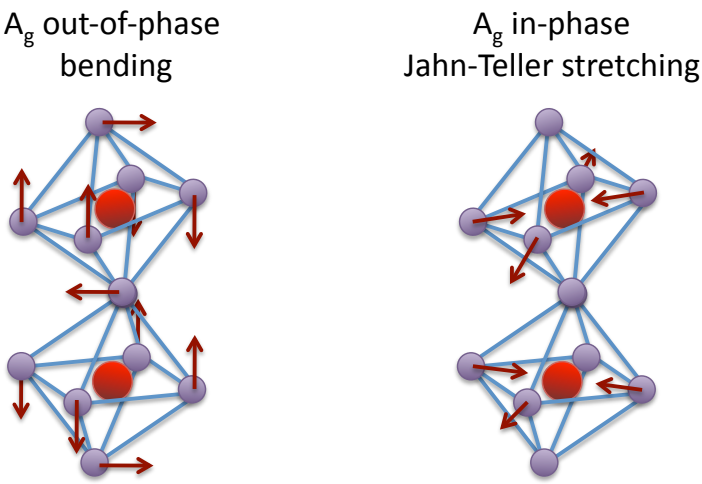

Figure 5.10: Ionic motions associated with the normal-mode displacements observed in the transient reflectivity of $LaMnO_3$.

enhanced specific the cross sections and two high energy peak were observed, consisting of a peak at 448 cm^{-1}, which was assigned to the out-of-phase bending mode, and a higher energy mode at 496 cm^{-1}. The higher frequency 496 cm^{-1} mode matches the frequency observed the reflectivity. Krüger assigned this mode to the in-phase Jahn-Teller distortion of the oxygen octahedra. The ionic motions associated with the modes observed in the reflectivity data are are shown in figure 5.10.

The frequencies obtained from the Fourier transform can be used to fit the oscillations as a function of temperature with,

$$\frac{\Delta R_{osc}}{R} = -\mathrm{erf}(t) \sum_{i=1,2} B_i \exp(-\Gamma_i t) \cos(2\pi f_i), \tag{5.2}$$

where f_1 and f_2 are fixed at the high (14.9 THz) and low (8.8 THz) frequency modes. B_i and Γ_i are the amplitude and damping rates of the modes respectively. No phase shift from a cosine-like oscillation was required to improve the fit of either lattice vibration. The phase of the oscillation is determined by the ratio of the real and imaginary parts of the Raman tensor at the pump wavelength [73]. As the pump beam covers the resonance feature in the absorption (figure 5.2), the imaginary part of the Raman tensor is much stronger than the real part, resulting in a purely displacive excitation of the lattice. Additionally, the fit agrees well for all times indicating that the phonon-mode frequencies are not softened by the laser pulse and remain constant.

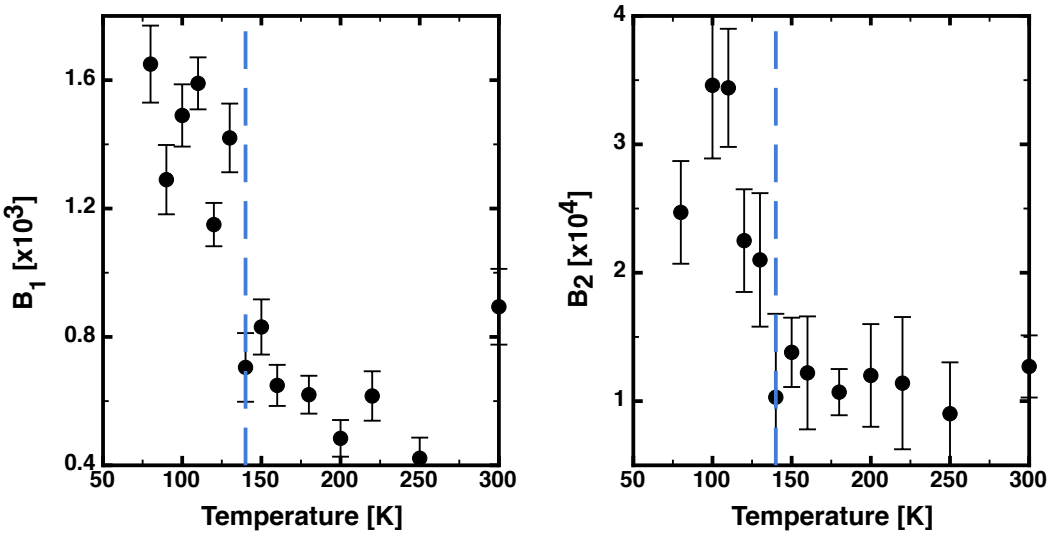

Figure 5.11: The temperature dependence of the amplitude of the phonon modes. The dashed blue line is at T_N.

The temperature dependence of the B_i modes are shown in figure 5.11. Both modes show very little variation in amplitude on cooling until the temperature is reduced below the Néel temperature, at which point there is a sharp increase in the amplitude of both modes. The ratio between both modes stays constant across the antiferromagnetic phase transition temperature suggesting that the mechanism behind the enhanced signal has the same origin.

According to the displacive excitation of coherent phonon (DECP) mechanism (see chapter 3), the amplitude of the induced oscillations, B, is given by $B \propto \Im(\epsilon)\Xi^2$, where ϵ is the dielectric function and Ξ is the deformation potential. The imaginary part of the dielectric function, as a function of temperature, has been measured by Kovaleva [92] (figure 5.2) for light polarized in the *ab*-plane. The measured value for the dielectric function at 1.9 eV, corresponding to the peak in the pump spectrum, are plotted in figure 5.12, normalized to the value at 200 K. Also plotted is the amplitude of the high frequency oscillation, which has been scaled to the high temperature absorption data.

The oscillation amplitude follows the changes in the absorption until the temperature is reduced to the Néel temperature suggesting that the deformation potential remains constant. However, on cooling below T_N, the oscillation amplitude increases sharply and no longer follows the temperature dependence of the absorption. This suggests that phase transition

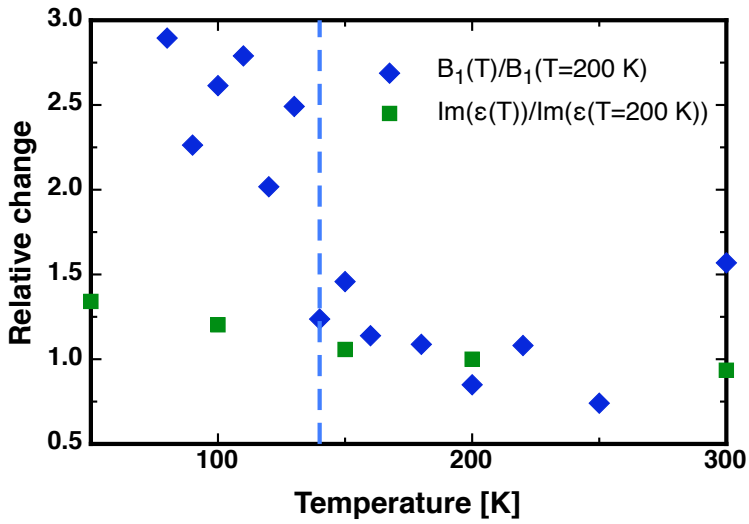

Figure 5.12: A comparison between the change in absorption at 1.9 eV as measured by Kovaleva [92] and the change in the amplitude of the coherent lattice vibration as a function of temperature. The imaginary part of the dielectric constant has been normalized to the value at 200 K. The oscillation amplitude, B_1, has been normalized to the mean of the values at 180, 200 and 220 K.

results in a significant change in the deformation potential experienced by the lattice after optical excitation. Figure 5.12 suggests that the deformation potential changes by a factor of 2 in the anti-ferromagnetic phase, suggesting that a strong coupling between the lattice and magnetic state develops.

The temperature dependence of the damping rate for each mode is shown in figure 5.13. On cooling from 300 K, the damping rate of the phonon mode decreases. However, at T_N, the temperature dependence changes dramatically and the damping rate increases with further cooling.

There are two mechanisms which are responsible for the damping rate of phonons, dephasing due to elastic scattering from impurities and population loss due to inelastic scattering of phonons. For high quality single crystals the dephasing term is small and can be neglected and the dominant damping mechanism is due to inelastic scattering of the phonons.

Phonons scatter from each other due to the anharmonic potential of the crystal field. The damping rate, Γ_0, of a phonon at the center of the Brillouin zone with an angular frequency

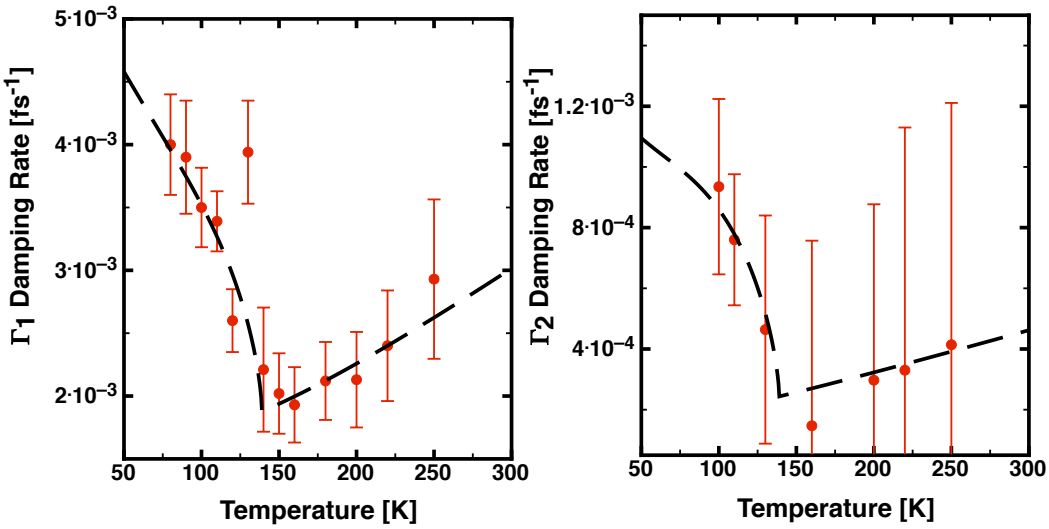

Figure 5.13: Damping rates of the lattice vibrations as a function of temperature. Dashed lines are the fits of equation 5.7 to the experimental data.

ω_0 can be written as [100],

$$\Gamma_0 \propto \sum_{i,j,q} |V(0,q,-q)|^2 \{[1 + n(\omega_{iq}) + n(\omega_{j-q})]\, \delta(\omega_0 - \omega_{iq} - \omega_{j-q}) \\ +2[n(\omega_{iq}) - n(\omega_{jq})]\delta(\omega_0 + \omega_{iq} - \omega_{jq})\}, \tag{5.3}$$

where V is the cubic anharmonic potential, $n(\omega_{iq})$ is the occupation of the phonon state with frequency ω in branch i and with wave vector q. The first term is the inelastic scattering of a phonon at the zone-center into two lower energy phonons with equal but opposite momentum. The second term corresponds to the frequency up-conversion of the optic phonon at the zone-center with an additional phonon. As the coherently generated phonons are at a high energy, the second term in equation 5.3 can be neglected as there are a significantly lower number of higher energy phonon modes available when compared to the number of low frequency modes.

The first term generates phonons with an energy $\omega_{iq} + \omega_{j-q} = \omega_0$. Scattering can occur between phonons on the same branch ($i = j$) resulting in the overtone scattering channel, or between branches ($i \neq j$) in the combination scattering channel. An accurate description of the damping rate should take into account the scattering due to both channels, which requires a detailed knowledge of the phonon dispersion relation across the entire Brillouin zone. However, as the energies of the excited phonons are large, it can be assumed that the

combination channel will provide the majority of the signal which result in the generation of high energy acoustic phonons. These phonons are close to the zone boundary and, as a result, have a large density of states. With this approximation, the damping rate of excited lattice vibrations can be described as,

$$\Gamma_{\mathrm{ph}}(T) = \Gamma^0_{\mathrm{ph}}\left(1 + 2n(\omega_0/2)\right) = \Gamma^0_{\mathrm{ph}}\left(1 + \frac{2}{\exp\left(\frac{hf_0}{2kT}\right) - 1}\right), \tag{5.4}$$

where Γ^0_{ph} is the damping rate at $T = 0$ and f_0 is the frequency of the mode and the occupation number is given by the Bose-Einstein distribution function.

In addition to scattering between phonons, phonons can also scatter with magnons through the spin-orbit interaction. The description is very similar to that of equation 5.4, with both the energy and momentum of the phonon being conserved in the decay into two magnons. However, the number of magnons available in the system is set by the magnetic order parameter and the damping due to magnon scattering is given by,

$$\Gamma_{\mathrm{M}}(T) = \Gamma^0_{\mathrm{M}}\left(1 + \frac{2}{\exp\left(\frac{hf_0}{2kT}\right) - 1}\right) M(T), \tag{5.5}$$

where, $M(T)$ is the order parameter of the anti-ferromagnetic phase transition. For temperatures close to but below the Néel temperature $M(T)$ can be written as,

$$M(T) = \left(1 - \frac{T}{T_N}\right)^{2\beta}, \tag{5.6}$$

where β is the critical exponent of the anti-ferromagnetic phase transition. The critical exponent has been measured by neutron scattering with a small discrepancy values ranging from 0.28 to 0.34 [101, 102].

The total damping rate of the phonon mode is the sum of equations 5.4 and 5.5,

$$\Gamma(T) = \Gamma_{\mathrm{ph}}(T) + \Gamma_{\mathrm{M}}(T). \tag{5.7}$$

Equation 5.7 was used to fit the experimental data in figure 5.13 and the fitting parameters are displayed in table 5.1. The quality of the fit in the high temperature region justifies the assumption that the predominant decay mechanism for high energy optic phonons is to acoustic phonons of equal energy. During the fitting procedure, β was held constant and fits were performed with $\beta = 0.28$ and $\beta = 0.34$, with the latter value gaving the best fit to the experimental data.

	$LaMnO_3$		Gd[a]	Tb[a]	Bi[b]	GaAs[c]	InP[c]
f(THz)	8.8	14.9	3	3	2.79	8.85	10.5
Γ^0_{ph} (ps^{-1})	0.16(2)	1.7(1)	0.075(9)	0.075(9)	0.015	0.11	0.025
Γ^0_{M} (ps^{-1})	1.2(1)	4.1(7)	0.16(2)	1.03(2)	-	-	-

Table 5.1: Phonon damping rates in $LaMnO_3$ with the critical exponent was fixed at $\beta = 0.34$, compared to damping rates in other materials. [a]Ref. [103], [b] [104], [c] [100].

To date, relatively few phonon damping rates have been measured in the time domain, with most restricted to materials with simpler crystal structures and with slower optical phonons, and even fewer have investigated the effects of phonon-magnon scattering. Melnikov et al. [103] used the second harmonic generated at the surface of magnetic Gd and Tb thin films to measure the damping rate of a 3 THz mode. The energy of the modes are significantly lower than either mode in $LaMnO_3$ and, as a result, the damping rate is significantly lower. Hase et al. [104] measured the damping rate of non-magnetic Bi, using the same technique presented here and obtained Γ =0.015 ps^{-1} for a 2.79 THz mode, again significantly lower than in $LaMnO_3$. Vallée [100] used coherent anti-Stokes Raman scattering (CARS) to measure the damping rate of LO phones in GaAs and InP. The damping rate of the 8.85 THz phonon of GaAs is very close to that of the 8.8 THz mode in $LaMnO_3$. Detailed band structure calculations showed that the high rate is due to a large density of states available in the decay pathway, whereas InP has a different band structure which restricts the decay of the phonons.

It is interesting that $LaMnO_3$ has a large magnon-phonon coupling. Scattering between magnons and phonons occurs because the two quasi-particles are coupled via the spin orbit interaction. The coupling strength dictates the rate of scattering and is proportional to $\lambda \boldsymbol{L} \cdot \boldsymbol{S}$, where λ is the spin-orbit coupling constant, $\boldsymbol{L}$ is the total orbital angular momentum and $\boldsymbol{S}$ total spin of the system. In the absence of spin-orbit coupling, and other perturbations, the obital angular momentum of Mn^{3+} ion in a cubic field is quenched ($\boldsymbol{L} = 0$). The spin-orbit interaction reduces the effect of the crystal field and reintroduces a finite orbital angular momentum. As the damping rate in $LaMnO_3$ is high, it can be concluded that spin-orbit coupling must be a relatively strong effect. Evidence for a large spin-orbit interaction is also observed in measurements of the single ion anisotropy [105] and from magneto-restriction [102]

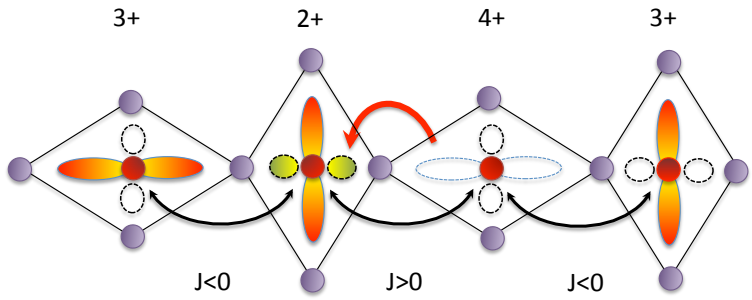

Figure 5.14: The excited state of $LaMnO_3$ after a charge transfer excitation within the *ab*-plane

5.4.1 Origin of the magneto-elastic interaction

The excitation and subsequent decay of coherent phonons in $LaMnO_3$ is well described by the DECP mechanism and phonon-phonon and magnon-phonon scattering. However, greater physical insight and a qualitative explanation of the origin of the magneto-elastic coupling can be obtained by applying the Goodenough-Kanamori rules to the photo-excited state of $LaMnO_3$. With a 2 eV pump pulse, electrons are excited across the Mott gap to create Mn^{2+} and Mn^{4+} sites as shown in figure 5.14. Both the Mn^{2+} and the Mn^{4+} configurations are Jahn-Teller inactive. Therefore, these lattice sites will prefer to relax the local Jahn-Teller distortion. As the excitation is prompt on time timescale of the atomic motions, the relaxation will generate large-amplitude high-frequency oscillation at the Jahn-Teller stretching mode frequency.

In addition to the reduction of the Jahn-Teller distortion, the excited state will exhibit a different exchange coupling between neighboring ions. On applying the GK rules to the excited state the exchange integral between the two excited ions remains the same (i.e. ferromagnetic) as the bond is now between a half-full $d_{y^2-z^2}$ orbital and an empty $d_{3y^2-r^2}$ orbital. However, adjacent ions will experience exchange between two half-full and two empty $d_{y^2-z^2}$ and $d_{3y^2-r^2}$ orbitals, both of which give rise to an anti-ferromagnetic exchange coupling. This view is also consistent with the Kugel and Khomskii model introduced in chapter 2, where photo-excitation disrupts the local orbital ordering resulting in a change in the (orbital dependent) exchange 'constant'.

As discussed in chapter 2, Goodenough showed that the length of the bond is related to

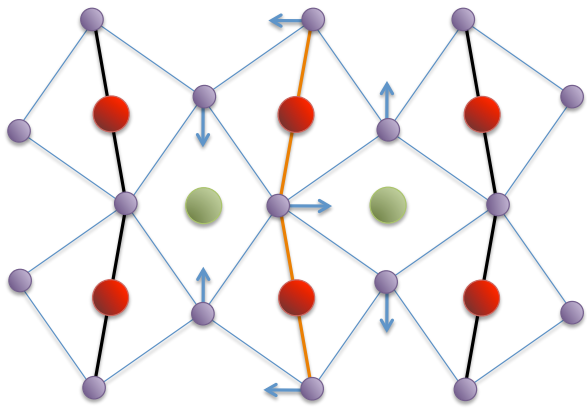

Figure 5.15: The photo-excited (orange) semi-covalent bond experiences a change in sign of the exchange integral. As a result there is a force to reduce the Mn-O-Mn bond length. The induced displacements map onto the out-of-phase rotation of the 8.8 THz mode.

the type of exchange coupling across it. The anti-ferromagnetic, fully covalent bond prefers a symmetric, shorter-length bond than that formed by semicovalent ferromagnetic bond. In order to reduce the Mn-O-Mn bond length, the lattice can reduce the Mn-O-Mn bond angle. The atomic motion associated with this relaxation maps onto the low frequency 8.8 THz mode as shown in figure 5.15. The same is true for the Jahn-Teller stretching mode, which relaxes the long-short bond ordering resulting in a more symmetric bond.

Below the Néel temperature these effects become more pronounced as they are of magnetic origin. The long range ordering will enhance the restorative force experienced by the excited state as the effects will not be reduced by thermal fluctuations experienced in the non-magnetic phase.

5.5 Summary

By exciting $LaMnO_3$ at the Mott gap with sub-10 fs pulses of light, large amplitude coherent oscillations can be excited, corresponding to the A_g out of phase bending (8.8 THz) and A_g Jahn-Teller stretching (14.9 THz) of the oxygen octahedra. The amplitude and damping rate of the oscillations shown a strong dependence on the magnetic phase of the system, with both the amplitudes and the damping rates increasing dramatically below the Néel temperature. This increase is attributed to coupling between the lattice and the magnetic state, the origin

of which can be described by applying the Goodenough-Kanamori rules to the excited state of the system and showing how photo-excitation can modify the local exchange interaction.

These results highlight the mechanisms by which light can couple to the electronic, structural and magnetic state of a complex solid. These results show how the many degrees of freedom in the manganites are coupled together. This coupling offers an explanation of how, both exciting a manganite with light [24], and by selectively exciting a lattice mode [27], can induce similar responses.

Chapter 6

Dynamics of the Insulator-Metal phase transition in $Pr_{0.7}Ca_{0.3}MnO_3$

6.1 Photo-induced Insulator-Metal phase transition

As described in chapter 2, the low bandwidth manganite $Pr_{1-x}Ca_xMnO_3$ has attracted considerable attention due to the existence of a 'hidden' metallic phase which cannot be accessed via chemical doping or temperature. However, a metallic transition can be induced by the application of a magnetic field [35], electric field [43], X-ray irradiation [44], and the application of pressure [42]. These effects are particularly strong at $x = 0.3$.

Interest in the manganites from an ultrafast perspective started when the insulator-to-metal phase transition was shown to occur in $Pr_{0.7}Ca_{0.3}MnO_3$ after excitation by a laser. Miyano et al. [24] measured the time-resolved voltage drop across two gold contacts deposited on a sample of $Pr_{0.7}Ca_{0.3}MnO_3$ separation by $50\,\mu$m after irradiation with the output of a 5 ns optical parametric oscillator. The applied voltage and laser intensity were varied and the dynamics were observed on a digital oscilloscope.

When a low voltage was applied between the gold contact, the laser induced a current pulse which was observed as a voltage drop on the oscilloscope. The decay time of the voltage drop was observed to increases with increasing laser pump power. Above a threshold pump fluence, a permanent metallic state could be formed. The insulating state would only recover after the bias voltage was removed. The permanent phase transition required a lower pump power for lower photon energies or for higher applied bias voltages. The transition would

occur for temperatures up to 90 K, above which the static resistance of the material is too low to maintain the bias voltage.

Fiebig et al. [106] were able to demonstrate that resistivity of $Pr_{0.7}Ca_{0.3}MnO_3$ dropped by more than 8 orders of magnitude. The associated change in reflectivity was large enough for the photo-excited region to be imaged by a CCD. It was observed that the excited region formed a single filament between the two electrodes, the width of which could be controlled by the changing the voltage applied across the contacts. By measuring the action spectra* of the insulator-to-metal phase transition [107], Fiebig concluded that the photo-induced phase transition consisted of two steps and the mechanism by which the phase transition occurred was fundamentally different to the mechanism driving the magnetic field induced change. Fiebig argued that the magnetic field induced phase transition was due to amplification of the double exchange mechanism, where the applied magnetic field forces the ferromagnetic alignment of the t_{2g} spins which increases the electron transfer integral t. Whereas, photo excitation directly disrupts the charge ordering in the material. The excited electrons screen the coulomb repulsion and form metallic domains. These domains are stabilized by the applied electric field, which forces their coellecanae into a metallic filament which is stable within the anti-ferromangetic charge-ordered background.

Measurements of the change in reflectivity from the electrical field-stablized photo-induced phase transition show similarities to those observed under a transition induced by a magnetic field [108]. The reflectivity spectra, after a magnetic field-induced transition, shows an increase in reflectivity at low energies (< 0.5 eV), indicative of a Drude response and a decrease was observed at higher energies. The biggest drop in reflectivity was around 1.2 eV which corresponds to the charge transfer resonance in $Pr_{0.7}Ca_{0.3}MnO_3$. The reflectivity change after photo-excitation exhibited the same trend, however, for 1.8 eV photons and above, an increase in reflectivity is observed, the magnitude of which was similar to the maximum drop in reflectivity at 1.2 eV. The mechanism causing the increase in reflectivity is currently unknown, but is likely to be due to difference in the transition pathways, with the field-induced transition remaining in thermodynamic equilibrium, whereas the photo-induced transition occurs due to non-equilbrium dynamics. In addition, the photo-induced phase is surrounded

*The action spectra is the wavelength dependence of the threshold fluence for the insulator-metal phase transition to occur.

by anti-ferromagnetic, charge ordered material and is likely to be under significant structural strain, which will also effect the optical response.

6.2 The insulator-to-metal phase transition on the ultrafast timescale.

As the insulator-to-metal phase transition can be triggered by laser excitation, there is the possibility for the phase transition to occur on an ultrafast time scale. However, the experiments described previously measure the dynamics occurring over several nanoseconds. Experiments to measure the transient change in reflectivity were performed with pulses of order 150 fs [109]. However, as seen in chapter 5, short, sub-10 fs pulse are needed to excite the material coherently.

6.2.1 Transient metallic measurements

Measurements on the ultrafast timescale require a reduction of pulse duration of approximately 6 orders of magnitude over those used in the experiments discussed in section 6.1. Although the photo-induced phase transition is not a result of laser-induced heating of the sample, it is still necessary to ensure that the phase transition occurs when the material is excited with a femtosecond pulse. Measurements of the insulator to metal phase transition were performed in a similar way as those performed by Miyano [24][†]. Gold contacts were deposited 200 μm apart on the surface of a $Pr_{0.7}Ca_{0.3}MnO_3$ sample. The sample was mounted in a liquid nitrogen cooled cryostat and cooled to 77 K, below the charge-ordered (CO) and Néel temperatures ($T_{CO} = 220$ K, $T_N = 110$ K).

The laser used to excite the sample was a 70 fs 800 nm Ti:sapphire laser, which was focused to a spot size that fully illuminated the sample between the electrodes. The sample was biased with a 10 V well below that required for the electric field induced insulator-metal phase transition [43]. The signal was amplified by a fast, 50 Ω input impedance, amplifier and the voltage drop was measured across a 50 Ω resistor in an oscilloscope.

The decay rate of the metallic state was observed to increase with increasing pump power, in agreement with the results obtained by Miyano. At the highest pump fluences, the sig-

[†]Transient resistivity measurements were provided by Dr. M Rini, Lawernce Berkeley National Laboratory.

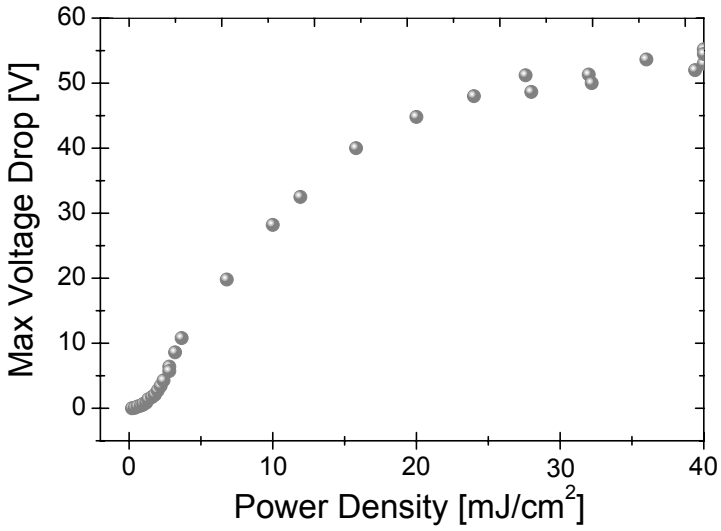

Figure 6.1: The fluence dependence of the voltage drop across the load resister after photo-excitation of $Pr_{0.7}Ca_{0.3}MnO_3$.

nal had not completely recovered before the arrival of the next pump pulse, 1 ms later. The measured voltage drop showed a non-linear dependence on the fluence. A threshold of approximately 1 mJ cm^{-2} is observed, and the voltage dropped across the load resistor saturates for pump fluences above 30 mJ cm^{-2}. For a pump fluence of 50 mJ cm^{-2}, the resistivity dropped from $3 \times 10^4\,\Omega$cm to $1 \times 10^{-1}\,\Omega$cm, which is similar to the change induced by a 6 T magnetic field [35].

In order to measure the formation of the metallic state, the properties of $Pr_{0.7}Ca_{0.3}MnO_3$ have to be probed on a time scale which is much faster than that provided by the oscilloscope, which has a temporal resolution of a few nanoseconds. The formation of the metallic state can be observed by large changes in the reflectivity spectrum, which lends itself to ultrafast measurements with 10 fs resolution.

6.2.2 Ultrafast changes in reflectivity: Low Temperature

Experiments to measure the transient change in reflectivity were performed at the Politecnico di Milano and made use of two independent short pulse visible non-colinear optical parametric amplifiers. The experimental setup was similar to that used to measure the change in reflectivity in $LaMnO_3$ (figure 5.5). However both pump and probe wavelengths were p-polarized. The sample was pumped with a central wavelength of 550 nm with 560 nJ pulses. The probe-

pulse was centred at 650 nm. The pump and probe pulses were focused to a 20 μm diameter spot by the same 5 cm focal length curved mirror. This corresponded to a maximum pump fluence of 25 mJ cm^{-2} at the sample surface. Transient changes in reflectivity were measured at 77 K, in the anti-ferromagnetic, charge-orderd insulating phase and at room temperature when the material is a paramagetic insulator. Measurements were performed using interference filters with a 10 nm bandwidth in order to reduce the effects of scatter from the pump beam and to resolve the measurements as a function of wavelength.

Figure 6.2 shows the change in reflectivity of $Pr_{0.7}Ca_{0.3}MnO_3$ at 77 K when probed at 660 nm over a range of temporal durations. The change in reflectivity is very long lived and lasts for several nanoseconds [109], before decaying back to the ground state. Figure 6.2a shows the dynamics over a 10 ps time scale. On this scale, after the initial dynamics the change in reflectivity change appears constant.

Before discussing the dynamics of the reflectivity change in more detail, it is necessary to show that a phase transition is occuring. Evidence for this provided by measuring the spectral and fluence dependence of the reflectivity change, both of which are shown in figure 6.3. The change in reflectivity as a function of wavelength was measured by changing the interference filter in front of the diode measuring the reflectivity. The wavelength dependence (6.3a) showed the same trend measured by Fiebig, with the lower energy reflectivity showing the largest drop and positive signals at higher photon energies. The fluence dependence of the change in reflectivity (fig 6.3b) has the same dependence on fluence as that of the measured voltage drop, again exhibiting a threshold of approximately 1 mJ cm^{-2}.

The time scale on which the phase transition occurs can now be addressed by examining the reflectivity dynamics in more detail. Figure 6.2b shows the dynamics up to 2 ps. After an initial drop in reflectivity, which lasts for approximately 200 fs, low frequency oscillations were observed. The dynamics relax to an approximately constant value with an exponential decay of 360 fs. After subtracting the decay, the Fourier transform of the oscillations could be performed and the result is displayed in figure 6.4. The central oscillation frequency is at 2.38 THz or 78 cm^{-1}. This mode is observed in Raman measurements, but has not been assigned. The unassigned mode corresponds to motions of the A-site ions, which are most likely excited due to volume changes due to the formation of the metallic state.

Figure 6.2c shows the changes in reflectivity that occur during the first few hundred

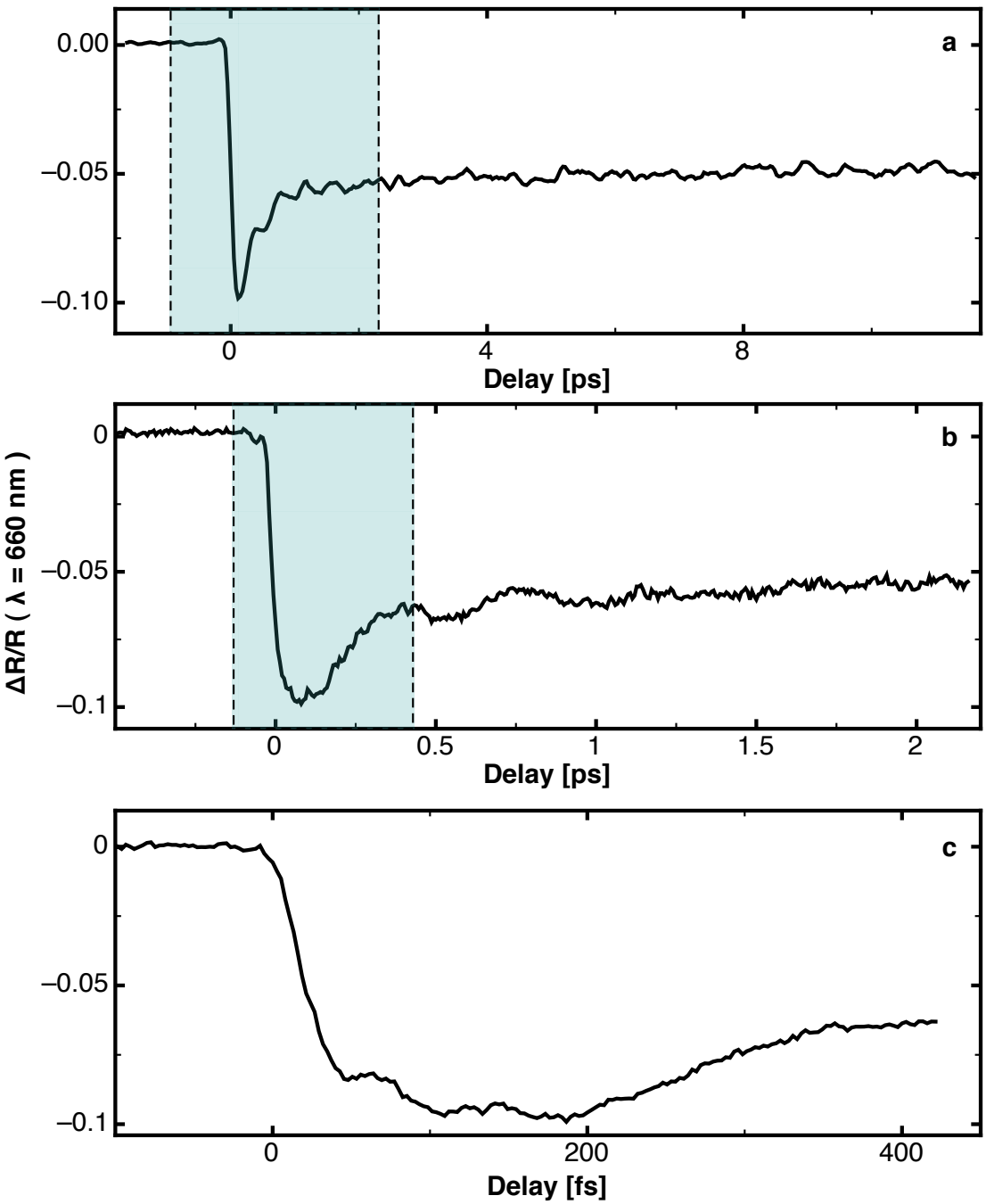

Figure 6.2: The transient change in reflectivity of $Pr_{0.7}Ca_{0.3}MnO_3$ at 77 K over several timescales. The shaded area corresponds to the region examined in higher resolution in the following graph.

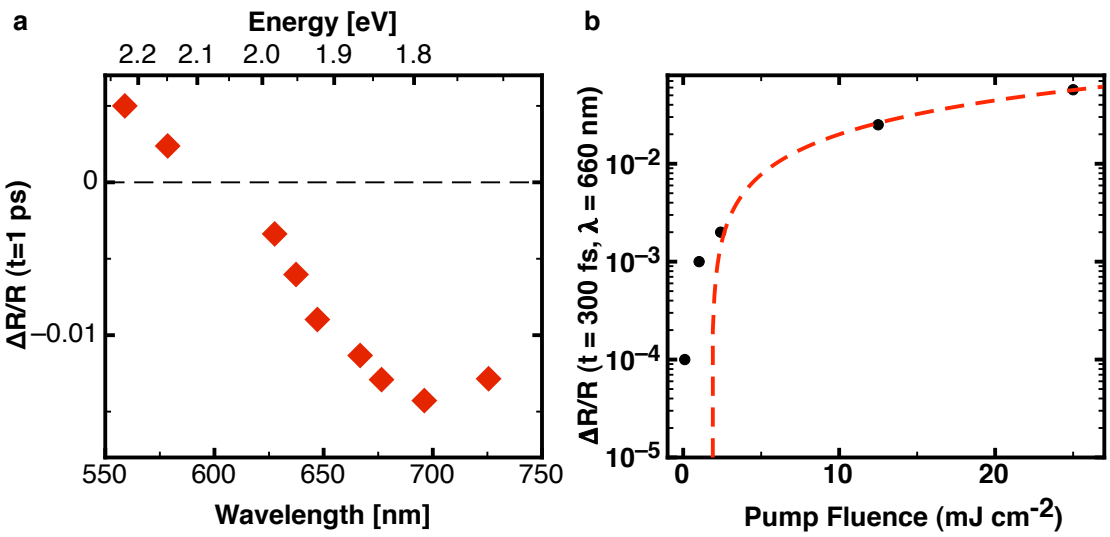

Figure 6.3: a. The spectral dependence of the reflectivity spectra after 1 ps. b. The fluence dependence of the magnitude of the reflectivity change at 660 nm. The dashed line is a linear fit to the last 3 data points, showing a threshold of $\sim$1 mJ cm^{-2}. Both measurements taken at $T = 77$ K.

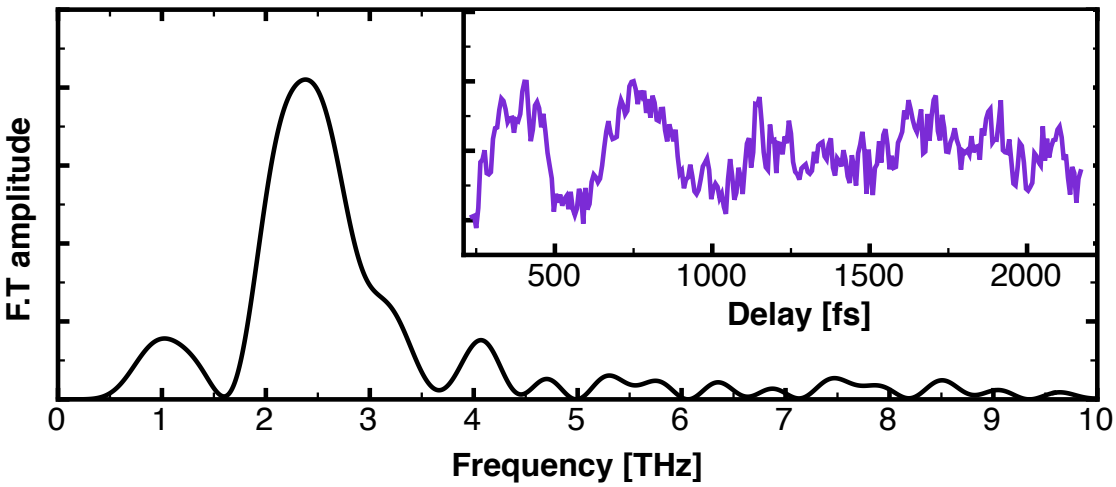

Figure 6.4: The Fourier transform of the low frequency oscillations. The peak occurs at 2.38 THz. The insert shows the background subtracted oscillations.

femtoseconds. On the rising edge of the signal several high frequency oscillations can be observed before the signal reaches a maximum. This can be fitted by the following equation,

$$\frac{\Delta R}{R} = \mathrm{erf}(t)\{Ae^{-t/\tau_1} + B\cos(2\pi ft + \phi)e^{-t/\tau_2} + C(1 - e^{-t/\tau_3})\}. \tag{6.1}$$

The only free parameters in the fit are the amplitudes of the electronic, A, and phononic, B, signals, the phase, ϕ, of the low frequency 2.38 THz oscillation and the time taken, τ_3, to reach the equilibrium value C. The decay time, τ_2, of the oscillation is longer than the measured time window, therefore, it was not used in the fit. The same applies for the decay of the equilibrium value C, which decays on an even longer timescale.

The fit, plotted in figure 6.5a, can be used to interpreted the reflectivity dynamics as follows: There is an initial signal created by the excitation and subsequent relaxation of electrons, which recovers on a timescale of $\tau_1 = 360$ fs, at the same time, coherent, low frequency, 2.38 THz, lattice vibrations are triggered with a phase shift $\phi = 0.93$ rad from a cosine like dependence. After a characteristic time $\tau_3 = 115$ fs the quasi-static reflectivity is obtained.

The fit can be subtracted from the measured data to leave the high frequency oscillations, which, together with the Fourier transform, are displayed in figures 6.5b-c. The 14.7 THz oscillations are strongly damped and completely decay after a few oscillations, with a decay constant of 140 fs. The frequency is again in good agreement with the Jahn-Teller stretching Raman active A_g-mode observed in $LaMnO_3$. There is little change in frequency between the two samples as the mode consists of oxygen ionic motion only. However, the heavy damping of the 14.7 THz mode is in strong contrast to what is observed in the experiments performed in $LaMnO_3$ reported in chapter 5, where a decay time of the oscillation was almost a factor of 2 longer at the same temperature.

The enhanced damping rate of the Jahn-Teller phonon can be used to gauge the formation time of the metallic state. CMR experiments in $La_{0.5}Ca_{0.5}MnO_3$ show that on entering the metallic phase, either by temperature, or by the application of a magnetic field, the amplitude of the Jahn-Teller phonon is reduced to zero and is associated with reduction of the long range static Jahn-Teller distortion in the metallic phase [110]. Therefore, the damping rate of the Jahn-Teller phonon can be used as a gauge of the timescale on which the insulator to metal phase transition occurs.

The 140 fs decay time of the Jahn-Teller phonon is similar to the the time taken to reach

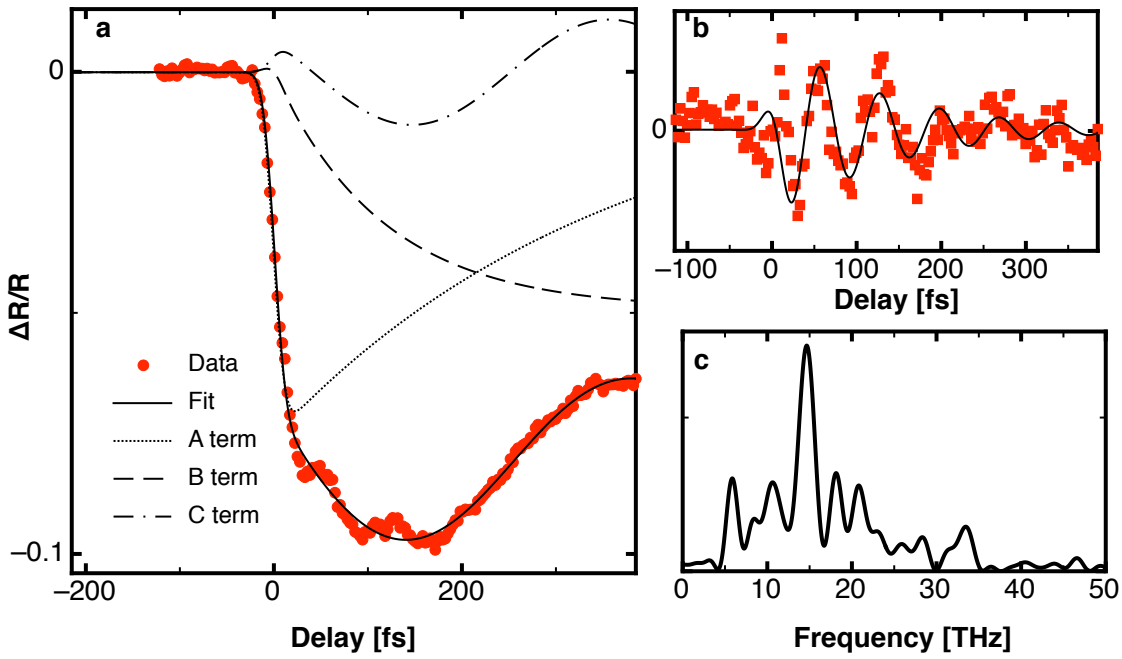

Figure 6.5: a. The change in reflectivity during the first 400 fs together with the fit obtained from equation 6.1. b. The residual high frequency oscillations c. The Fourier transform of b showing a peak at approximately 14.7 THz.

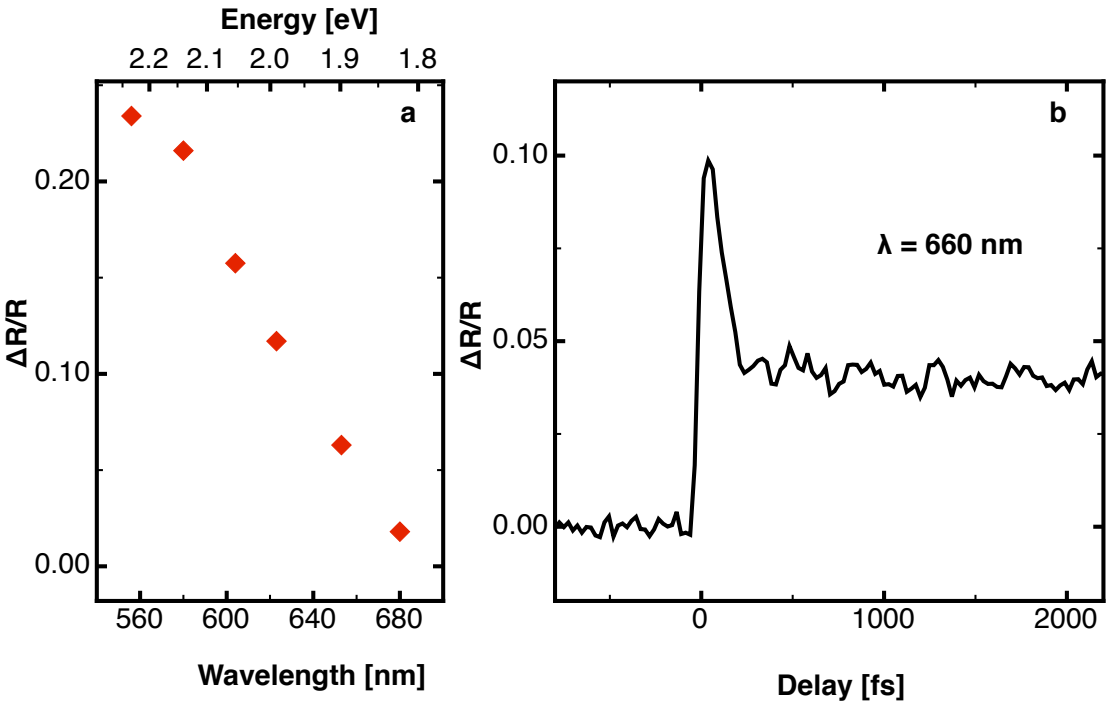

Figure 6.6: a. Spectral dependence of $\frac{\Delta R}{R}$ measured after 1 ps. b The transient change in reflectivity over 2 ps for $Pr_{0.7}Ca_{0.3}MnO_3$ at room temperature

the quasi-static equilibrium reflectivity, $\tau_3 = 115$ fs. In addition, the phase shift of $\phi = 0.93$, corresponds to a temporal shift of 62 ps. The period for the Jahn-Teller phonon $T = 1/f =$ 68 fs, suggesting that the low frequency mode is delayed by the excitation of the Jahn-Teller phonon.

These timescales suggest that metallic state is not formed immediately after photo-excitation, but a structural rearrangement is required, providing a bottleneck for the phase transition. The metallic state does not form until several phonon oscillations have occurred. This is in agreement with measurements of insulator-metal phase transitions in materials with strong electron-phonon coupling, such as VO_2, where the phase transition timescale also depended on the phonon frequency [29]. It is also in contrast to that observed in ET-F_2TCNQ, which has very low electron-phonon coupling and has a rapid response to laser excitation.

6.2.3 Ultrafast changes in reflectivity: High Temperature

The transient change in reflectivity was also measured at room temperature, in the paramagnetic insulating phase. The magnitude of the reflectivity change is comparable to that

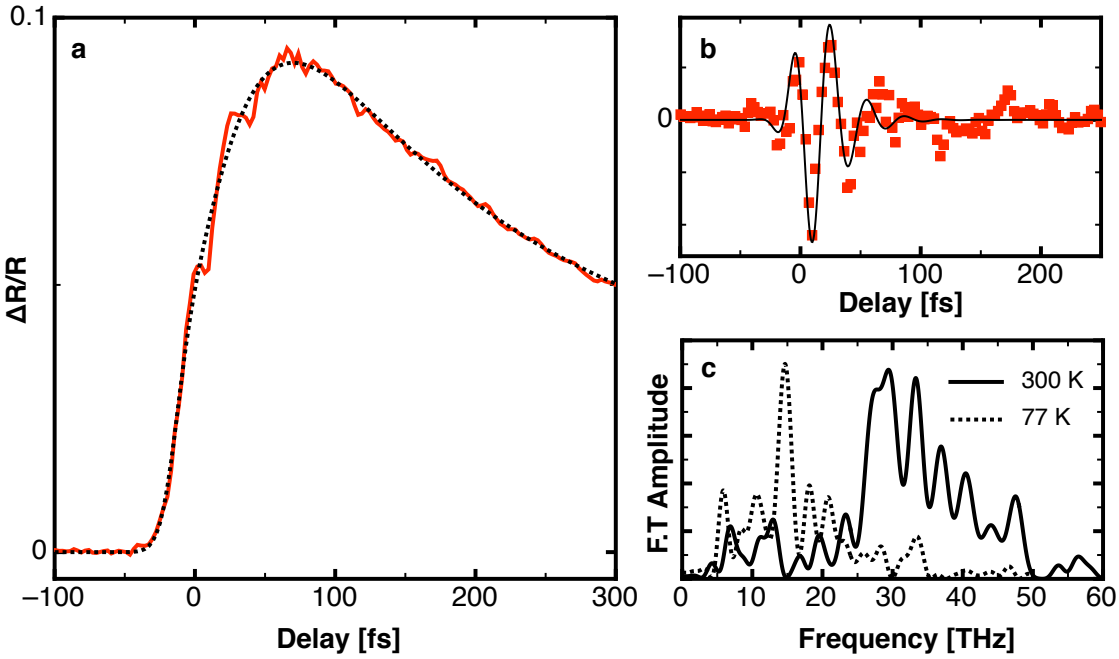

Figure 6.7: a. High temporal resolution transient change in reflectivity at 660 nm and fit. b. Residual high frequency oscillations. c Fourier transform of the oscillations and comparison to low temperature data.

observed when the material is in the anti-ferromagnetic insulating phase, however the spectral response is different. Figure 6.6a shows the wavelength dependence of the change in reflectivity. Again, the higher energy response shows an increase in reflectivity for high photon energies, however, a decree in reflectivity occurs at lower photon energies. A time scan measured at 660 nm is shown in Figure 6.6b. Again a long-lived 'product-phase' is observed which decays on a nanosecond time scale.

The reflectivity is again fitted by equation 6.1. However, in the paramagnetic phase the low frequency 2.38 THz mode is heavily over-damped, with a time constant of $\tau_2 = 30$ fs. The long lived quasi-stable state is formed rapidly with a time constant τ_3=70 fs, and the electronic signal is found to decay with a time constant $\tau_1 = 160$ fs.

The residual change in reflectivity is shown in figure 6.7b. The change in reflectivity in the paramagnetic phase does not exhibit any oscillations at the Jahn-Teller frequency. This is because the paramagnetic phase of $Pr_{0.7}Ca_{0.3}MnO_3$, although not metallic, does not exhibit a long range Jahn-Teller distortion, and the 14.7 THz phonon is not observed in

the static Raman spectra. However, oscillations at a very high frequency are observed. After subtracting the fitted background, the Fourier transform of the oscillation is taken and plotted in figure 6.7c. A broad range of frequencies are present which are centred at approximately 33 THz (132 meV, 1070 cm^{-1}). The Fourier transform is compared to that taken from the low temperature data, showing that no component at the Jahn-Teller frequency is observed. The high frequency oscillations are heavily damped and decay with a time constant of 25 fs.

6.2.4 Orbitons

The long range ordering of orbitals found in the manganites suggests that collective excitations of the orbitals should be possible. An excitation in a magnetically ordered system results in the generation of a spin wave in the material which, when quantized, is called a magnon. In the same way, an excitation of an orbital in an orbitally ordered system should result in an orbital wave, or orbiton. The dispersion relation of the orbiton has been calculated by several authors both with and without, coupling between orbitals and Jahn-Teller phonons [49, 111–113]. In both cases, orbitons remained gapped excitations across the entire Brillouin zone.

Orbitons should be observable using inelastic scattering techniques such as inelastic X-ray scattering [114] and Raman spectroscopy. To date, observation of orbitons has remained controversial, especially in the manganites. Saitoh et al. were the first to claim the observation of orbitons via Raman scattering in the un-doped manganite $LaMnO_3$ [111]. Three peaks were observed at 125, 145 and 160 meV. The assignment of the peaks was justified by theoretical calculations of the orbiton energy. The intensity and energy of these peaks was observed to reduce and soften on heating, and vanishing at T_{JT}, the temperature at which the long-range cooperative Jahn-Teller distortion vanishes, suggesting significant coupling between the orbital-order and the Jahn-Teller distortion.

However, the interpretation of orbital ordering was questioned by Grüninger et al. who suggested that the signal was due to two-phonon scattering [115]. The orbiton peaks are very close to the second harmonic of the ∼80 meV phonon peak. In addition, measurements of the optical conductivity showed the orbiton modes were also IR-active. As orbitons conserve parity, they should not show an IR-active signal, strongly suggesting that orbiton interpretation of the Raman data was incorrect.

The multi-phonon interpretation was reinforced by resonant Raman scattering measure-

ments. The Raman probe wavelength was tuned over several absorption resonances found in $LaMnO_3$ [99]. Different photon energies resonantly enhance different phonon modes, however, it was found that the resonance response of the high energy modes was identical to the low energy mode, suggesting they shared a common origin and the high energy mode was a result of multi-phonon scattering.

It is interesting to review these ideas in light of the high frequency oscillations observed in the transient reflectivity of the paramagnetic phase of $Pr_{0.7}Ca_{0.3}MnO_3$. The high frequency oscillations cover the energy range predicted and observed by Saitoh [111]. Although the modes observed in $LaMnO_3$ by Saitoh are unlikely to be due to orbitons, it is worth considering if the oscillations in the reflectivity of $Pr_{0.7}Ca_{0.3}MnO_3$ are.

There are several arguments against the multi-phonon interpretation for the reflectivity dynamics. The most likely two-phonon combination that would produce an oscillation around 33 THz is from two Jahn-Teller phonon ($2 \times 14.9 = 30$ THz). However, in the paramagnetic phase of $Pr_{0.7}Ca_{0.3}MnO_3$ this mode is not present in the Raman spectra and so is unlikely to contribute. In addition, the reflectivity measurement measures the frequency of the oscillations directly, unlike Raman scattering which measures the change in photon energy. If the oscillations are due a two-phonon process, the low frequency oscillations should also be observable in the reflectivity, yet figure 6.7c shows no Jahn-Teller frequency component. In addition, in the low temperature phase, where the single phonon frequency is observable, no two-frequency oscillation is observed.

However, the two-phonon interpretation cannot be completely discarded. Single-phonon lattice vibrations can only be excited with wave vectors near the zone-centre ($k \approx 0$), due to the low momentum of the incident photons. However, two-phonon excitations, can occur across the entire Brillouin zone as long as the total momentum is zero. Therefore, the single phonon oscillations may be 'dark' whilst the zone centred two-phonon signal can be observed. Detailed knowledge of the phonon-dispersion curves would be needed to see if this is a plausible explanation. Another explanation for the lack of fundamental mode is that a Raman-active two-phonon mode can be derived from Raman-inactive single phonon modes which cannot be excited.

The orbiton interpretation is not without its own difficulties. Long range orbital ordering in $Pr_{0.7}Ca_{0.3}MnO_3$ has a much lower transition temperature than $LaMnO_3$, with the charge

and orbital ordering transition occurring at $T_{\mathrm{CO}} = 220\,\mathrm{K}$. In the paramagnetic phase, where the high frequency oscillations are observed, there is no long range orbital ordering and below the orbital ordering phase transition temperature, the high frequency oscillations are not observed. One tentative explanation for this is that the orbiton energy is too high in the low temperature phase to be excited by a coherent excitation. On heating the system the orbiton mode may soften, to an energy scale that can be excited coherently. Although the high temperature phase is paramagnetic, it is still considered to consist of nano-clusters of phase separated regions [36]. This would allow orbital ordering with a short coherence length, and could explain the very rapid damping time for the oscillations.

It is also interesting to note that no orbiton/two-phonon signal was observed in reflectivity data of $LaMnO_3$ presented in chapter 5. $LaMnO_3$ exhibits a Jahn-Teller distortion up to $\approx 780\,\mathrm{K}$. As all reflectivity measurements were taken below this temperature, there was always a structural component to the orbiton energy. The softening of the mode could come from the relaxation of the structural component of the orbiton energy, leaving only an electronic contribution in the higher temperature phase.

Ultimately, neither explanation is a completely satisfactory explanation for the oscillations in $Pr_{0.7}Ca_{0.3}MnO_3$, and more experimental and theoretical work is needed in order to interpret these results. The argument could be resolved by repeating the experiment with a sample with isotope-substituded oxygen. This will shift the phonon peaks, whist the orbiton frequency should be relatively unchanged. However, as these materials are very sensitive to perturbations, shifts in the phonon frequencies could have dramatic effects on the material properties and result in significantly different behaviour.

Chapter 7

Time resolved XANES spectroscopy of $Pr_{0.7}Ca_{0.3}MnO_3$

7.1 XANES spectroscopy

The microscopic electronic processes that underpin changes in the conductivity and optical properties of a material resulting from an insulator-metal transition occur due to changes in the electronic configuration of specific ionic species. Thus best probed by using element specific techniques. Statically, this is typically achieved using X-ray absorption spectroscopy (XAS). By measuring the energy dependence of the X-ray absorption close to a core-level transition, information about the density of unoccupied states close to the Fermi-level can be obtained. This technique is referred to as X-ray absorption near edge structure (XANES) spectroscopy.

A representation of the transitions probed by XANES spectroscopy is shown in figure 7.1. Core-level electrons are promoted from ionic-bound states to energy bands in the material or to continuum states in the vacuum. Transitions to unoccupied states are constrained by the dipole selection rules, restricting the transitions to those which change the parity of the wavefunction, or states which change the angular momentum of the single electron ($\Delta l = \pm 1$).

XANES spectroscopy can also provide information on the local environment of individual ions. The core-edge absorption wavelength is dependent on the ionic species. By performing XANES measurements at different edges in a material, differences in the bonding states for each ion can be observed.

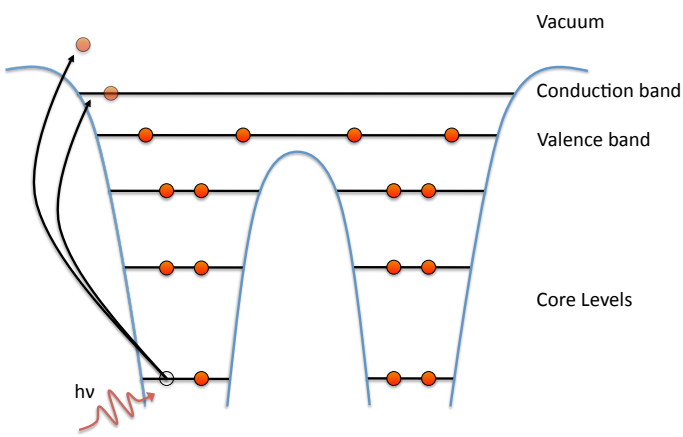

Figure 7.1: Schematic of a transitions probed by XANES spectroscopy. The X-ray produces a hole in the core level and the electron transition is to either a bound of the crystal or to the continuum in the vacuum depending on the X-ray energy.

XANES signals can be measured using several techniques. For optically thin samples, the XANES signal can be measured via the wavelength dependence of the absorption. For optically thick samples, the XANES signal can be measured by collecting all the light emitted from a material as it relaxes back to the ground state, known as the total fluorescence yield (TFY). This radiation is emitted into a 2π solid angle and requires a large area detector. X-ray excitation also generates free electrons, either through direct photo-emission or Auger recombination. The total number of emitted electrons, or total electron yield (TEY), is also proportional to the XANES signal. The TEY signal is generally considered more surface sensitive than the TFY measurement as the escape depth of the electrons is significantly lower than that of light.

7.1.1 Static XANES spectra of $Pr_{0.7}Ca_{0.3}MnO_3$

Figure 7.2 shows the static XANES signal from $Pr_{0.7}Ca_{0.3}MnO_3$ at the oxygen K-edge and the manganese L_{II} and L_{III} edges*. Measurements were taken at room temperature at the 4-ID-C undulator beamline at the Advanced Photon Source, Argonne National Laboratory. The measurements shown in figure 7.2 were obtained using the total electron yield technique with an energy resolution better than 0.25 eV. The XANES signal was also measured in total

*Data shown were provided courtesy of Dr. Matteo Rini, Lawrence Berkeley National Laboratory

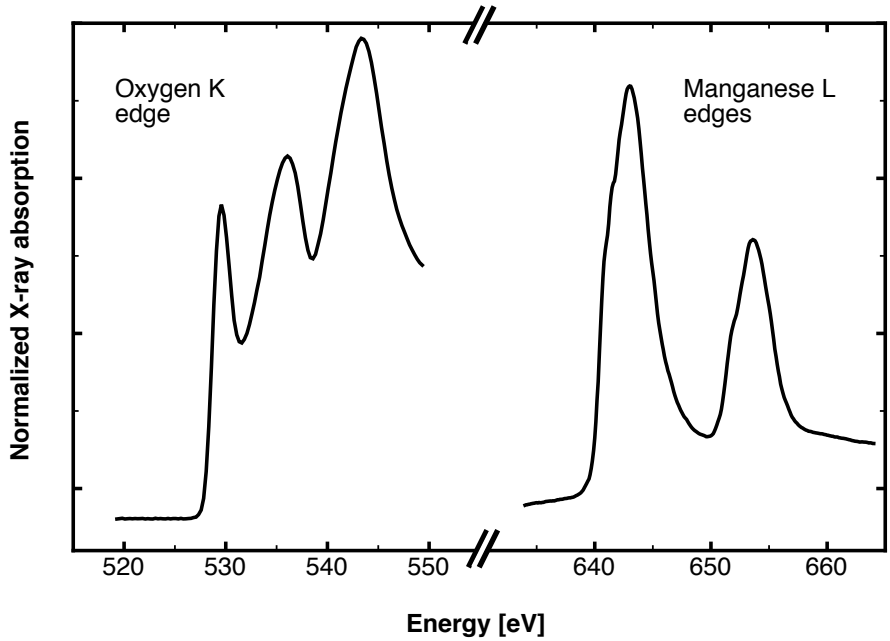

Figure 7.2: The oxygen and manganese XANES spectra measured in total electron yield.

fluorescence yield which gave near identical results, demonstrating that the TEY signal is representative of the bulk properties of $Pr_{0.7}Ca_{0.3}MnO_3$. Measurements were taken at 80 K and room temperature, however, no difference between the XANES signals could be resolved, in agreement with the findings reported in ref [116].

The XANES spectra of the Oxygen K-edge probes transitions of electrons from the O $1s$ level to unoccupied levels around the Fermi level and the continuum. Three peaks are clearly observed at 529.6 eV, 536.1 eV and 543.3 eV, before the transitions into the vacuum. As $\Delta l = \pm 1$, the transitions are to to states that have np[†] character where $n > 1$ is the principle quantum number. All three peaks are due to hybridization states of the oxygen $2p$ levels with the neighboring ionic wavefunctions. The lack of $3p$ character in the final state has been demonstrated in theoretical calculations by reference [117], and is due to the strong covalent bonding between the oxygen $2p$ levels and the surrounding ions dominate in transition metal compounds. The first, lowest energy, peak in the oxygen edge corresponds to transitions to $2p$ levels hybridized with the Mn $3d$ levels [118]. The second peak corresponds to $2p$ levels hybridized with the Pr $5d$/Ca $3p$ levels, and the third, highest energy, peak corresponds to hybridizations with the Mn $4sp$-hybridized levels [119].

[†] $p \equiv l = 2$

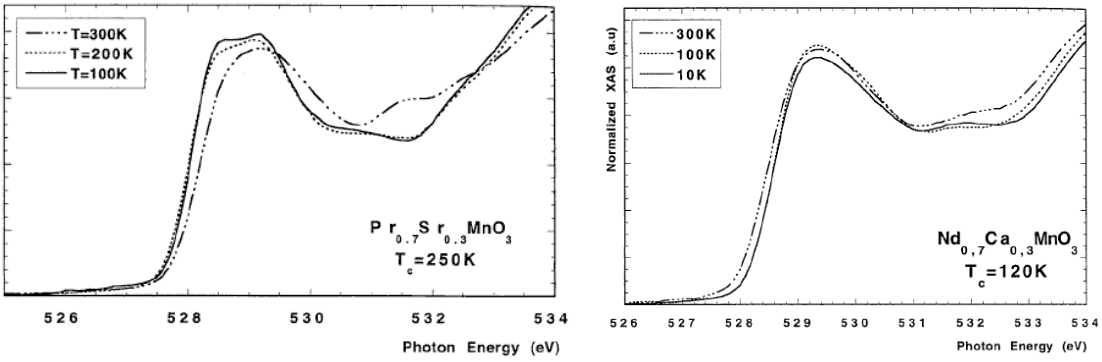

Figure 7.3: The XANES spectra of $Pr_{0.7}Sr_{0.3}MnO_3$ and $Nd_{0.7}Ca_{0.3}MnO_3$ reproduced from ref [118].

The two large peaks correspond to transitions from the spin-orbit split L_{II} and L_{III} ($2p_{\frac{3}{2}}$ and $2p_{\frac{1}{2}}$) levels into states with $4s$ and $3d$ character and the vacuum, however the interpretation of which states are involved are more subtle than for Oxygen. XANES signals can be complicated by affects other than the Pauli exclusion principle and the dipole selection rules. The presence of the core-hole can effect the electronic structure of the excited state due to correlation effects. In such a case, the absorption signal is not simply proportional to the density of unoccupied states.

At the oxygen K-edge, core-hole effects are small because the core hole lies deep within the oxygen potential, and the effects are screened by the surrounding electrons. In addition, the transitions are into heavily hybridized states which are predominately localized on the metal ions, resulting in a large separation between the hole and the excited electron [117]. The core-hole on the manganese L-edge is in the p levels which is higher up the potential well and is screened less. In addition, the states which are probed, states hybridized with Mn-$3d$ and $4s$ levels, are localized on the metal ion and, therefore, experience a strong effect due to the core hole.

7.1.2 Insulator-to-metal transition in XANES measurements

As $Pr_{1-x}Ca_xMnO_3$ does not undergo a temperature driven insulator to metal phase transition, XANES spectra of the metallic state in thermal equilibrium are difficult to obtain. However, many different manganites have a temperature driven effect and have been studied via XANES spectroscopy.

Toulemonde et al. [118] performed XANES measurement on $Pr_{0.7}Sr_{0.3}MnO_3$, which has an insulator-to-metal phase transition at 250 K, and $Nd_{0.7}Ca_{0.3}MnO_3$, which has a transition to a ferromagnetic state at 120 K, but remains insulating. Toulemonde's measured XANES spectra are reproduced in figure 7.3. The insulator-to-metal transition in $Pr_{0.7}Sr_{0.3}MnO_3$ is manifested in the first oxygen peak by an increase in unoccupied density of states on the low energy side of the spectrum, corresponding to a red shift of the rising edge by ∼0.2 eV and the appearance of a double peak structure separated by ∼0.5 eV. $Nd_{0.7}Ca_{0.3}MnO_3$ in contrast, does not show a metallic phase and only a reduction of the density of states is observed when the material turns ferromagnetic.

Toulemonde made assignments of the first peak in the oxygen spectra with the use of cluster calculations on the Mn 3d levels. The resultant energy level diagram is reproduced in figure 7.4. At room temperature, the peak corresponds to transitions from the O1s state to O2p states hybridized with the unresolved set of $e_{g\uparrow}$ and $t_{2g\downarrow}$ sub-levels of the Mn-3d manifold. On cooling, the material enters the metallic state which reduces the Jahn-Teller distortion. This reduces the separation of the e_g levels, which allows the transitions to the lower energy $e_{g\uparrow}$ states and the higher energy $t_{2g\downarrow}$ states to be resolved. Transitions to the $e_{g\downarrow}$ site are at higher energies.

Similar, consistent, effects have also been observed in other insulator-metal transitions in different manganites [120, 121], suggesting that the red shift and two peak structure is a good indicator of the metallic state.

7.2 Time resolved XANES

By extending the XANES technique to the time domain, dynamical information about the changes of density of unoccupied states can be obtained. This is of particular importance for interpreting the photo-induced insulator-metal phase transition in $Pr_{0.7}Ca_{0.3}MnO_3$. This was first achieved, on the picosecond timescale, by Johnson et al. [122], who measured the effects of photo-induced melting of silicon at the silicon L-edge on a picosecond time scale. Cavalleri et al. used the same technique on picosecond [123] and then extending the temporal resolution to the femtosecond [26] timescale to measure the XANES signal during the photo-induced insulator to metal phase transition in thin films of VO_2. By probing photo-induced changes in the absorption at the vanadium L-edge and oxygen K-edge Cavalleri was able to show the

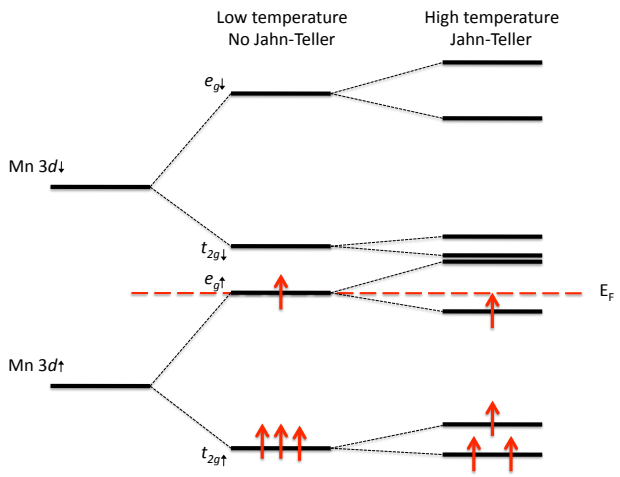

Figure 7.4: Manganese 3d energy level diagram in $Pr_{0.7}Sr_{0.3}MnO_3$ in the room temperature insulating and low temperature metallic state. Assignment based on refs. [118, 120]. In the low temperature phase the $e_{g\uparrow}$ is partially filled, resulting in a conducting band and transitions to unoccupied states in the $e_{g\uparrow}$ band and $t_{2g\downarrow}$ can be resolved. In the high temperature phase the Jahn-Teller distortion splits the e_g and t_{2g} levels resulting in an mix of unoccupied $e_{g\uparrow}$ and $t_{2g\downarrow}$ levels.

ultrafast collapse of the insulating band gap and the formation of a metal with hot-electrons.

The same technique is applied here to study the photo-induced insulator to metal phase transition in $Pr_{0.7}Ca_{0.3}MnO_3$.

7.2.1 Experimental setup

The time resolved XANES experiments were performed at the oxygen K-edge and Manganese L-edges on the ultrafast beamline 6.0.1 at the Advanced Light Source, Lawrence Berkeley national laboratory. The beamline is configured such that experiments can easily switch between femtosecond and picosecond sources of X-rays without having to change alignment of the system. As the experiment uses soft X-rays, the entire X-ray beam path and experiment was performed in UHV conditions with pressures below 10^{-8} mbar.

X-rays produced by the synchrotron traverse the beamline optics to a monochromator, where they are spectrally dispersed in the vertical direction. The beam is then focused by a grazing incidence curved mirror in the horizontal direction only. The X-ray beam passes through a narrow vertical slit of 75 μm which defines both the vertical beam size and the

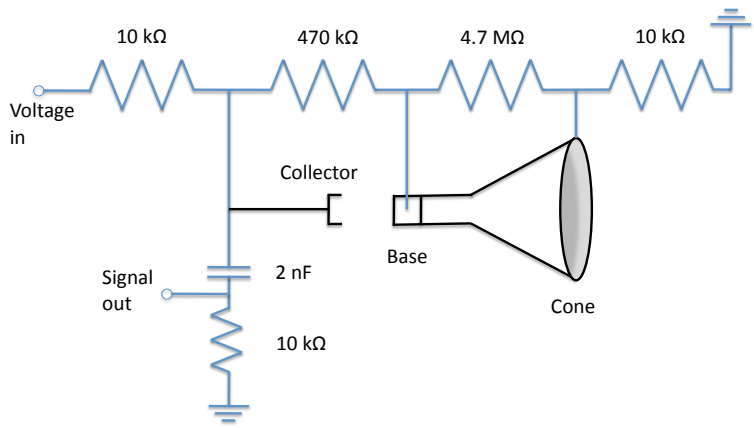

Figure 7.5: Biasing circuit for the channeltron detector.

energy resolution of the system. In the experimental configuration considered here, the energy resolution was approximately 0.5 eV. The experimental end station chamber is located after the slits, the centre of which is at the focus of the X-rays, and contains the sample and the detectors. By adjusting the horizontally focusing mirror, a focus of approximately $60 \times 75\,\mu m^2$ was achieved.

The $Pr_{0.7}Ca_{0.3}MnO_3$ sample, grown by the floating zone method, was cut and polished in the *ab*-plane. The sample was placed on the end of a cold finger which could be cooled to liquid nitrogen temperatures. The sample was mounted on a copper plate with a thermal epoxy and was electrically isolated from the main cold finger by means of a sapphire plate. The isolated sample was connected to a high voltage UHV feedthrough which allowed the drain current to be measured and the sample could be biased. The cold finger was mounted to an XYZ stage so the sample could be moved relative to the X-ray beam in order to find a good position on the sample. The sample could also be fully retracted from the X-ray beam to aid the alignment of the end station chamber and to allow access to timing diagnostic diodes located behind the sample.

The XANES signal was measured in total electron yield (TEY). This setup was chosen because the bulk sample of $Pr_{0.7}Ca_{0.3}MnO_3$ was several millimeters thick which prevented transmission measurements. Scattered photons from the pump laser also ruled out the possibility of TFL measurements. The X-ray-emitted electrons were measured using a channeltron detector. The cone of the channeltron was biased using a voltage dividing circuit shown in

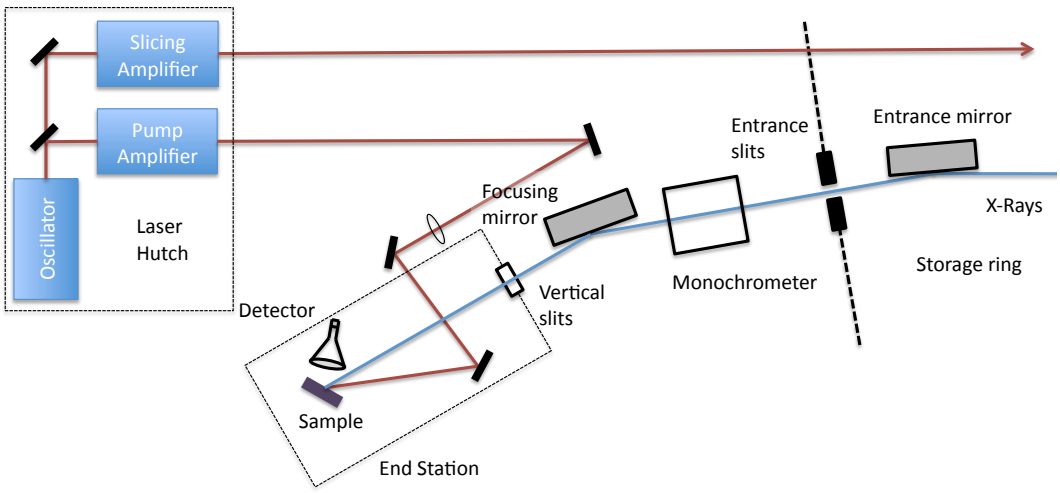

Figure 7.6: Schematic of the experimental setup for the time resolved XANES measurements. Additional beam line optics are not shown.

figure 7.5, with an input voltage of 1800 V. The cone of the channeltron was held close to ground (+40 V) and there was 1.6 kV drop between the cone and the base to accelerate the electrons and amplify the electron signal. The amplified electrons were collected with a 160 V extraction voltage, and the final signal was AC coupled over a 2 nF capacitor. The current signal was amplified by a fast 200× pre-amplifier, before being sent down a coaxial cable to the measurement electronics.

The 1 kHz 800 nm Ti:Saphhire laser used to pump the sample was synchronized to the X-rays and derived from the same source as the laser used in slicing (see appendix A). The pump beam traverses a path of a similar distance (≈50 m) to that of the slicing laser, in order that temporal overlap between the femtosecond X-rays and the laser can be achieved, before arriving at the end station chamber. The pump beam was focused into the chamber using an external 1 m focal length lens. By moving the the position of the lens along the direction of the beam propagation, the spot size at the sample surface could be controlled and matched to that of the X-rays. Inside the chamber was a fixed mirror, mounted close to the incoming X-ray beam in order to minimize the angle between pump and probe. A schematic of the experimental setup is shown in figure 7.6.

The laser produced a large number of relatively low energy electrons, which were detected by the channeltron. The intensity of photo-emitted electrons had a non-linear dependence

on the pump fluence but was only weakly dependent on the pump wavelength[‡]. It was concluded that these electrons were not simply the result of multi-photon photo-emission, but due to electric field enhancement at regions of surface roughness. In order to reduce electrons generated in this manner, great care was taken in polishing the samples to produce flat surface that was free of fissures, as well as by scanning the laser beam in order to find the smoothest region with the lowest laser yield. However, it was not possible to completely reduce the photo-electrons generated by the laser for reasonable pump fluences.

A further reduction in laser induced counts in the channeltron was achieved by applying a positive bias to the sample. The positive bias introduces an electric field between the channeltron and the sample which is slightly repulsive and could be made strong enough to eliminate photo-electrons from entering the channeltron. Applying a bias also reduced the number of counts produced by X-rays. Therefore, a compromise between pump fluence and sample bias was made. The laser fluence at the sample surface was $20\,\mathrm{mJ\,cm^{-2}}$, above saturation of the photo-induced phase transition. The emitted photo-electrons could be eliminated with a $+60\,\mathrm{V}$ bias to be applied to the sample.

Pump-probe data was accumulated at 2 kHz, twice the frequency of the pump laser. Two measurements of the X-ray signal were taken 500 ms apart, corresponding to one measurement with the laser present, S_{ON}, and one measurement with the laser absent, S_{OFF}. By constructing the quantity $\Delta S = \frac{S_{\mathrm{ON}}}{S_{\mathrm{OFF}}} - 1$ the laser induced fractional change in X-ray absorption signal can be measured which is free of longer term drifts and low frequency noise in the X-ray intensity.

7.2.2 Picosecond XANES

Measurements were performed using the picosecond bunch of X-rays, the duration of which was approximately 70 ps. This allows for spectroscopic measurements of the long lived state observed in the optical signal (chapter 6). The results of measurements at the oxygen K-edge and manganese L-edge are shown in figure 7.7. All the data presented here was taken at room temperature.

Time resolved XANES spectra were taken over the vicinity of the first pre-edge peak of

[‡]The wavelength dependence achieved by using the 800 nm pump beam to drive an OPA to generate light at $4\,\mu$m which was used to pump the sample.

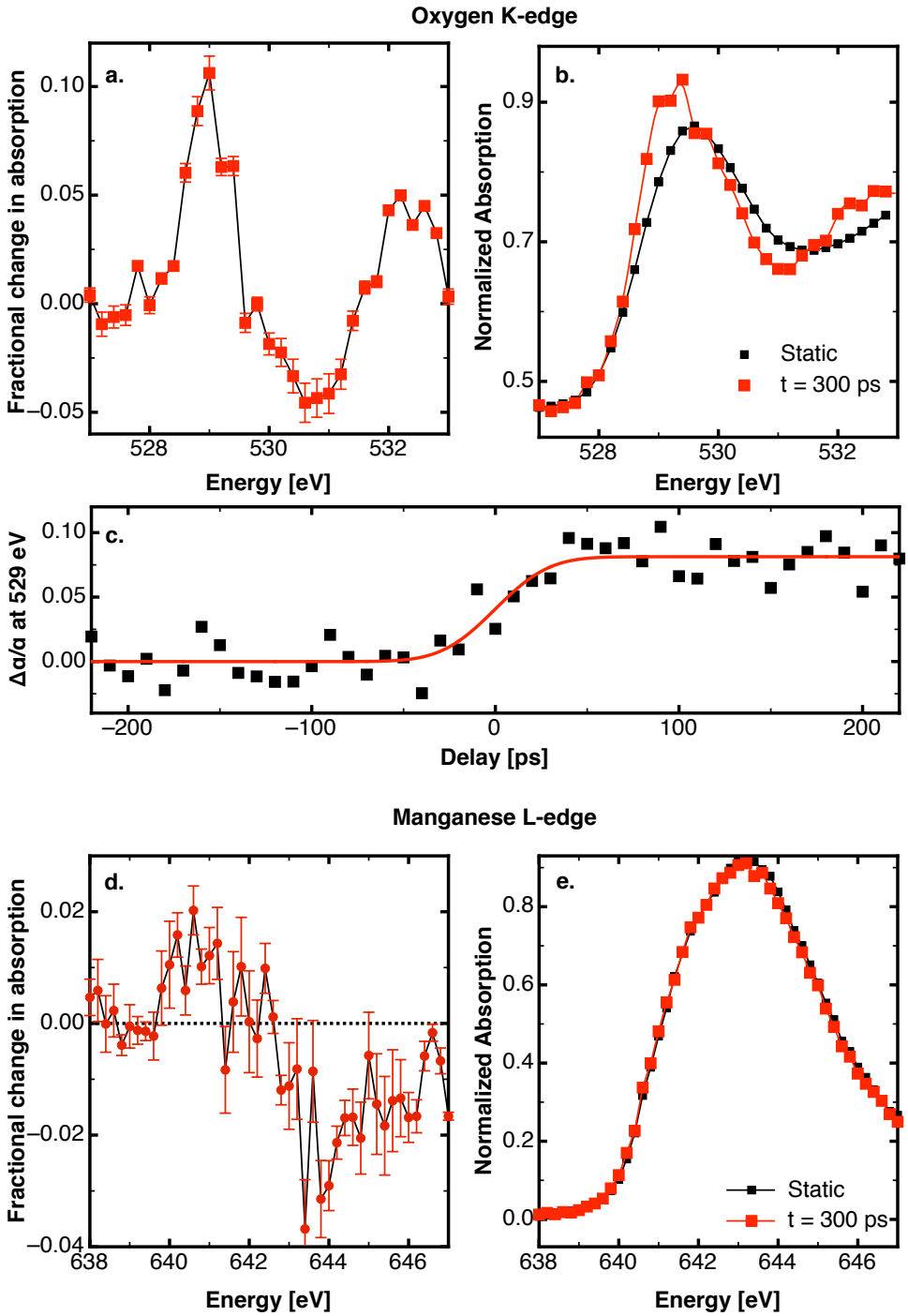

Figure 7.7: Time resolved changes in the XANES signal and the oxygen K-edge and manganese L-edge. a. The relative change in absorption of the first oxygen pre-edge signal. b. The photo-excited state and the static oxygen pre-edge. c. A time resolved scan at 529 eV. d. The relative change in absorption at the L_{II}-edge. e. The photo-excited and static manganese L-edge.

the oxygen K-edge as this peak gives the clearest indication of the metallic state. Figure 7.7a shows the fractional change in absorption from 527 to 533 eV, when measured 300 ps after laser excitation. Figure 7.7b shows the actual shape of the pre-edge in the static and photo-excited state when the data in figure 7.7a is added to that shown in figure 7.2.

The transient state shows a red shift of the pre-edge peak and a large increase in spectral weight of up to 10 % at 529 eV and a 5 % decrease in spectral weight at higher energies ($\sim 530 - 531.5$ eV). The time zero position was verified by performing a time scan at 529 eV, which is shown in figure 7.7c. The solid line is a fit to the curve obtained by an error function, which confirmed the 70 ps duration of the X-ray pulse length. The time resolved scan also shows that the excited state of $Pr_{0.7}Ca_{0.3}MnO_3$ is quasi-stable showing no dynamics over the measured temporal range, but recovers to the ground state within 500 ms.

Measurements of the manganese L-edge proved to be more difficult than at the oxygen edge. The transient signal was much weaker (< 2 %) and required a significantly longer integration time to obtain. The fractional change in absorption is shown in figure 7.7d and the excited state pre-edge peak is shown in figure 7.7e. The L_{II}-edge shows a small red-shift and narrowing upon photo-excitation, which is again long lived.

The data presented here shows striking similarities to the XANES signals observed by Toulemonde [118] and reproduced in figure 7.3. A similar increase in spectral weight at low energies and a decrease in spectral weight at higher energies is also seen during the insulator-metal phase transition in $Pr_{0.7}Sr_{0.3}MnO_3$ on cooling. However, due to the relatively poor energy resolution of the measurement presented here (~ 0.5 eV), the detailed structure, such as the double peak, cannot be observed. The time-resolved measurement indicates that the metallic state forms within the 70 ps of the probe pulse and forms a quasi-stable state. This should be contrasted to the behavior of $Nd_{0.7}Cs_{0.3}MnO_3$, which does not undergo a thermally induced insulator-metal phase transition. As a result the pre-edge does not change shape with temperature, and does not match the changes in spectral weight observed here.

Time resolved experiments were repeated at 80 K and an identical change in the oxygen pre-edge peak was observed. This rules out laser-induced heating as the origin of the time-resolved XANES signal. In the static spectra, no change in the XANES signal could be measured between 80-300 K. Therefore, if the observed signal was a result of simple heating, no time resolved signal should be observable. The effect of photo-excitation of $Pr_{0.7}Ca_{0.3}MnO_3$

has a similar effect as cooling has on $Pr_{0.7}Sr_{0.3}MnO_3$, and is independent of initial temperature, demonstrating that the quasi-stable metallic 'phase' is non-thermal in nature.

7.3 Summary and conclusions

These experiments highlight how the technique of XANES can be extended into the time domain in order to measure the electronic structure of the transient, photo-induced, metallic-like state in $Pr_{0.7}Ca_{0.3}MnO_3$. It was shown that the changes in spectral weight after photo-excitation are similar to those observed in thermally driven insulator-metal phase transitions in other manganites.

Interestingly, the metallic state appears to be accessible from the room temperature phase. This is 150 K higher than what can be achieved when the sample is in a 12 T magnetic field with the CMR effect [35]. Although the paramagnetic room temperature phase does not exhibit a long-range Jahn-Teller distortion, it appears that photo-excition further reduces the Jahn-Teller coupling to the electron mobility, enabling the metallic state to form even at room temperature. As conductivity and ferromagnetism are closely related in the manganites, it would be interesting to observe if the photo-induced high temperature phase is also ferromagnetic. This would require additional measurements, such as X-ray circular dichroism of the Mn L-edge or time-resolved magneto-optical Kerr effect measurements.

Extending the XANES signal to the femtosecond timescale with slicing would enable the measurement of the dynamics associated with the formation of the metallic state. The dynamics associated with the motion of the ions observed in chapter 6 should have an observable effect on the evolution of the density of states until the quasi-equilibrium state is reached. Several experiments were attempted with femtosecond X-rays at the ALS in order to resolve these dynamics, however the measurements were unsuccessful. This was due to the low number of generated femtosecond X-rays and their low probability of producing a detectable electrons. Improvements to both the beamline and experimental setup, such as switching to a transmission setup with thin-film samples, are need before this experiment becomes possible with slicing.

Extending these measurements to a sub-100 fs timescale would reveal the dynamical evolution of the electronic state from the insulating phase to the conducting phase. This would be close to the limit that is achievable with time-resolution available to sliced electrons. If

probing could be achieved with sub-10 fs resolution, the affects of the Jahn-Teller phonon and orbitons on the formation of the metallic state could be observed. However, both measurements require sources that are not currently available, but may be achievable with future sources such as free electron lasers.

Chapter 8

Femtosecond X-ray diffraction from phonon-polaritons in $LiTaO_3$

8.1 Introduction

In previous chapters, this thesis has discussed the generation and observation of coherent lattice vibrations in the manganites. In the examples presented, the lattice is excited by a short pulse of laser light. This provides a displacive force on the lattice modes, causing them to vibrate coherently. These vibrations are observed by measuring the periodic change in the reflectivity of the material. However, the actual atomic motions are not observed and the assignment of the vibration to a normal mode motion is based on estimates of bond strengths.

This chapter discusses the use of ultrafast hard X-ray diffraction to directly observe ionic motion. Static hard X-ray diffraction reveals the structure and symmetry of the crystal, from-which the ionic positions of the material can be obtained. By extending this technique to the time domain, the motion of ions within a solid after laser excitation can be observed directly.

Unlike the lattice vibrations examined previously, this chapter discusses the results of measurements and simulates of a diffraction spot when IR-active phonons are driven by a THz light field. By modeling the propagation of the light field, together with the induced displacement of the lattice, an excellent match between the measured diffraction signal and calculated signal is found.

The work discussed here covers the first measurement of a phonon-polariton, a mixed-

mode consisting of the coupled driving electric field and the mechanical lattice vibration, propagating in $LiTaO_3$, using time-resolved femtosecond X-ray diffraction. The measurement of the mechanical field compliments previous measurements of the optical response of the system [124–126].

8.2 Phonon-Polaritons

When an electromagnetic wave propagates near a discrete resonance, energy is coupled from the light field to the resonant phenomenon. The resulting propagation can be described in terms of polaritons, a mixed-mode consisting of the electromagnetic wave and the resonant phenomenon. In dielectric materials, light can couple to dipole-active displacements of ions near IR resonances. The resulting polariton is referred to as a phonon-polariton. In metals, light can couple to plasma oscillations, resulting in plasmon-polaritons and in magnetic materials light can propagate as magnon-polaritons.

8.2.1 Light propagation in an IR active material

When the frequency of light is far from an IR active phonon, the coupling to the structure will be small, and the light will propagate as if in vacuum with a speed given by c_0/n, where c_0 is the speed of light in vacuum and n is the refractive index of the material. However, as the frequency of the light wave approaches that of the resonance, energy is transferred into the displacement of ions. In most materials this occurs at THz frequencies (10^{12} Hz), which are typical frequencies for atomic vibrations, and results a range of frequencies over which light cannot propagate through the material. This energy region is known as the Restsrahlen band and light is fully coupled to the IR active phonon modes. At higher frequencies, the ions can no longer oscillate as fast as the electric field and, therefore, less energy is coupled into the structural mode.

The propagation of the coupled waves can be described by Maxwell's equations with a polarization, $\boldsymbol{P}$, that depends on the atomic coordinates, the dynamics of which are dictated by Newton's laws of motion. For a linear response these equations can be written as

$$\ddot{\boldsymbol{w}} = b_{11}\boldsymbol{w} + b_{12}\boldsymbol{E}, \tag{8.1}$$

$$\boldsymbol{P} = b_{21}\boldsymbol{w} + b_{22}\boldsymbol{E}, \tag{8.2}$$

where $\boldsymbol{E}$ is the electric field and $\boldsymbol{w}$ is the net displacement of the positive ions relative to the negative ions multiplied by the square root of the reduced mass of the system per unit volume. From equation 8.1, b_{11} can be identified as the harmonic restoring frequency, $-\omega_{\mathrm{TO}}^2$, of the IR excitation which is perpendicular to the direction of the propagation of the wave. Conservation of energy can be shown to give the relation $b_{12} = b_{21}$ [127].

Equations 8.1 and 8.2 can be solved using plane wave solutions for $\boldsymbol{P}$, $\boldsymbol{E}$ and $\boldsymbol{w}$ of the form $e^{-i\omega t}$ which, after eliminating $\boldsymbol{w}$, gives

$$\boldsymbol{P} = \left(b_{22} + \frac{b_{12}^2}{\omega_{\mathrm{TO}}^2 - \omega^2} \right) \boldsymbol{E}, \tag{8.3}$$

and, therefore, the relative permittivity is given by,

$$\epsilon_r = 1 + \frac{1}{\epsilon_0} \left(b_{22} + \frac{b_{12}^2}{\omega_{\mathrm{TO}}^2 - \omega^2} \right)$$

where ϵ_0 is the permittivity of free space.

In the low frequency limit ($\omega \ll \omega_{\mathrm{TO}}$), the relative permativity is given by $\epsilon_r(0) = \epsilon_{\mathrm{dc}}$ and in the high frequency limit ($\omega \gg \omega_{\mathrm{TO}}$) the relative permittivity of the material is given by $\epsilon_r(\infty) = \epsilon_\infty$. These two requirements give

$$b_{12} = \sqrt{\epsilon_0(\epsilon_{\mathrm{dc}} - \epsilon_\infty)}\omega_{\mathrm{TO}},$$

$$b_{22} = \epsilon_0(\epsilon_\infty - 1).$$

and

$$\epsilon_r = \epsilon_\infty + \frac{\epsilon_{\mathrm{dc}} - \epsilon_\infty}{1 - (\frac{\omega}{\omega_{\mathrm{TO}}})^2}. \tag{8.4}$$

The relative permittivity can then be used to calculate the dispersion of the waves using the relation,

$$\omega = \frac{ck}{\sqrt{\epsilon_r}}, \tag{8.5}$$

where c is the speed of light in vacuum and k is the wave vector. The angular frequency, ω, is multi-valued for a given k. For example, the solutions for ω in equation 8.5 when $k = 0$ are $\omega = 0$ or $\epsilon_r = 0$. The latter gives,

$$\omega = \omega_{\mathrm{LO}} = \left(\frac{\epsilon_{\mathrm{dc}}}{\epsilon_\infty} \right)^{\frac{1}{2}} \omega_{\mathrm{TO}}. \tag{8.6}$$

Equation 8.6 is known as the Lyddane-Sachs-Teller relationship and connects the transverse optical phonon frequency to the higher energy longitudinal optical phonon frequency. The

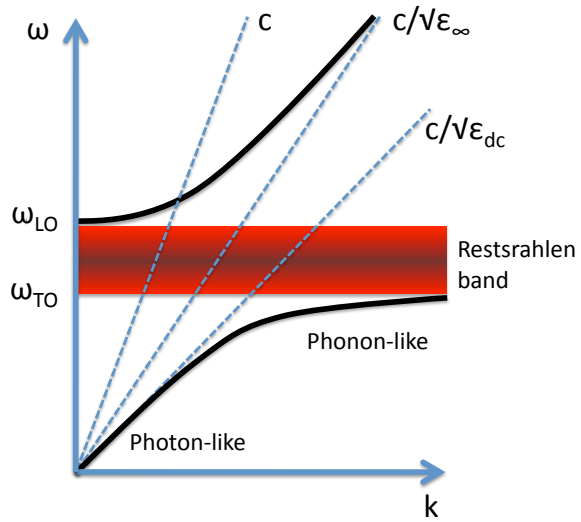

Figure 8.1: The dispersiont relation for light propagation near an IR active resonance. Far from the resonance the propagation of the mixed-mode is photon-like. As the frequency of the light approaches the resonance, the propagation takes more structural characteristics and is phonon-like.

longitudinal nature of the phonon mode can be seen from the solution of Gauss' law in a dielectric medium with no free charges. Gauss' law requires

$$\boldsymbol{\nabla}.\boldsymbol{D} = 0.$$

For plane wave solutions this reduces to

$$\epsilon_r(\boldsymbol{k}.\boldsymbol{E}) = 0.$$

Therefore, when ϵ_r is zero, the electromagnetic wave can have components that are parallel to the direction of motion.

The dispersion relation for an electromagnetic wave in an IR active material is shown in figure 8.1. Below the resonance the propagation is described as $\omega \approx ck/\sqrt{\epsilon_{\mathrm{dc}}}$. As the frequency of the light approaches that of the resonance, energy is coupled into the transverse optical phonon mode. As a result, the propagation takes on a phonon characteristic. On resonance a pure optic phonon is excited which has zero group velocity, i.e. $\mathrm{d}\omega/\mathrm{d}k = 0$, and does not propagate into the material and the electromagnetic wave is reflected from the surface. Above ω_{TO} is the Restsrahlen band which consists of frequencies that do not permit

propagating solutions. At higher frequencies, the propagation is again phonon-like until the frequency of the light field becomes too fast for the lattice to respond and the propagation returns to being light-like with $\omega = ck/\sqrt{\epsilon_\infty}$.

8.3 Time resolved diffraction

8.3.1 Kinematic diffraction

The diffraction of X-rays by a crystal lattice, in a reflection geometry, is described by Bragg's law. Diffraction peaks from $[hkl]$ planes are observed when the Bragg condition

$$d_{hkl}\sin(\theta) = n\lambda, \tag{8.7}$$

is satisfied, where d_{hkl} is the spacing of the $[hkl]$ lattice planes, θ is the angle the x-rays make with respect to the sample surface, λ is the wavelength of the X-rays and n is the order of the diffraction peak.

Bragg's law shows that the angular position of each peak in the diffraction pattern is dictated by the lattice parameters and the crystal symmetry. However, the amplitude of the peaks is dictated by the scattering factor of the unit cell, which is dependent on its constituent ions.

The scattering factor for a reflection from an $[hkl]$-plane is

$$F_{hkl} = \sum_{j}^{N} f_j e^{2\pi i \boldsymbol{G}_{hkl}\cdot\boldsymbol{r_j}}, \tag{8.8}$$

Where the sum is taken over all ions in the unit cell. f_j is the atomic form factor i.e. the scattering amplitude of the ion located at position $\boldsymbol{r}_j$. $\boldsymbol{G}_{hkl} = h\boldsymbol{b_1} + k\boldsymbol{b_2} + l\boldsymbol{b_3}$ is the reciprocal lattice vector, formed by the set vectors which are the reciprocal to the unit cell vectors.

8.3.2 Phonon effects on the diffraction signal

Until recently, the study of phonon dynamics has been left to indirect optical measurements or in-elastic scattering measurements, neither of which can reveal the actual motion of the ions responsible for the produced signals. Atomic positions are obtained from measuring the X-ray diffraction signal, therefore, by extending the technique to the ultrafast timescale, the motion of atoms within a solid can be observed.

The propagation of a phonon can effect both the amplitude and position of the diffraction peaks. Acoustic phonons propagate as density changes in the material and modify the lattice positions in the material. The movement of the lattice affects the spacing between the diffraction planes which results in shifts in the angular position of the diffraction peak.

Acoustic phonons can be generated by rapidly heating a material with an intense laser pulse. The energy deposited into the material is first deposited into the electrons and is then transfered to the lattice. This increases the temperature and pressure at a constant volume and launches a coherent stress-strain wave into the material which effects both the amplitude and position of the diffraction peak [65, 128].

Optical phonons correspond to ionic motions within the unit cell, therefore, do not result in a change in lattice spacing and the diffraction peaks remain in the same position. However, changing the positions of ions within the until cell changes the scattering factor (equation 8.8), which results in a modulation in intensity and width of the diffraction peak. The optical phonons that have been studied by X-ray diffraction to date have been excited through the DECP mechanism (see chapter 3). Phonons excited in this way oscillate at their natural frequency, ω_0, which is observed in the change in diffraction intensity [22, 129].

Phonon-polaritons, although optical phonons, are driven by the electric field of the light. Therefore, instead of oscillating at the natural frequency of the phonon, it propagates at the frequency of the driving electric field.

8.4 Experimental details and results

8.4.1 Properties of $LiTaO_3$

At high temperatures, $LiTaO_3$ is a paraelectric and the symmetry of the crystal is described by the space group $R\bar{3}c$. The structure consists of oxygen planes stacked along the c-axis with lithium ions situated within some of the oxygen planes and tantalum ions situated between some of the oxygen planes. Below $T_c = 907\,\mathrm{K}$ the lithium and tantalum ions move from their symmetric positions along the c-axis, to leave the material ferroelectric. The Ta ions move approximately 170 mÅ relative to the oxygen planes and, as a result, the crystal no longer has a centre of inversion and the space group becomes $R3c$. The crystal structure has been determined by Abrahams et al. using X-ray [130] and neutron [131] diffraction. The structural

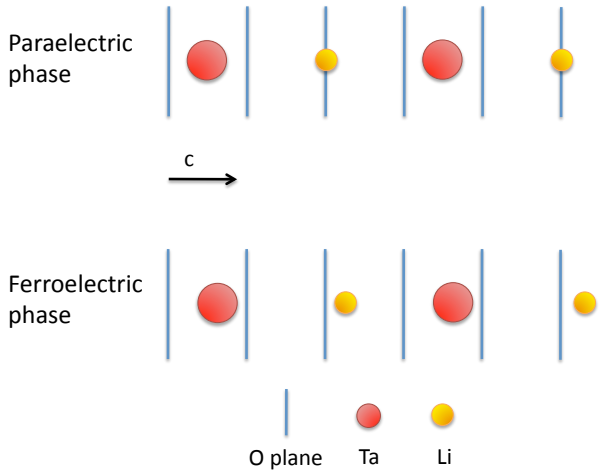

Figure 8.2: High temperature paraelectric (upper) and low temperature ferroelectric (lower) phases of $LiTaO_3$.

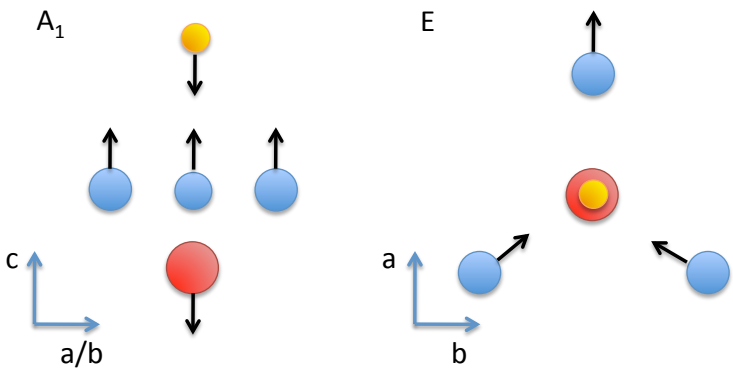

Figure 8.3: A sub unit of the $LiTaO_3$ showing the low frequency A_1 and E modes.

properties are reproduced in table 8.1, together with some optical properties, and a schematic of the unit cell is shown in figure 8.2.

As $LiTaO_3$ is a uniaxial crystal, the optical properties are dependent on the polarization of the light. Low frequency THz Light polarized along the c-axis couples to the A_1 phonon at 6.1 THz. The atomic motion associated with this phonon-mode is shown in figure 8.3a and corresponds to motion along the c axis only. The lowest frequency mode that can be coupled to in the ab-plane is the E mode which has a frequency of 4.3 THz. The motion associated with this mode is shown in figure 8.3b and is entirely within the plane of polarization.

The period of the phonon modes at their natural frequency are 233 fs and 164 fs for the E

Low temperature Atomic positions (fractional units) [130, 131]			
Element	x	y	z
Li	0	0	0.2790±17
Ta	0	0	0
O	0.0501±5	0.3436±3	0.0687±3
Unit cell parameters (hexagonal setting)			
a_H			5.15428±1 Å
c_H			13.78351±2 Å
Optical properties [132]			
for light polarized along the c axis:			
$\omega_{\mathrm{TO}}/2\pi$			6.0 THz
ϵ_{dc}			34.5
ϵ_{∞}			7.6
$n(\lambda = 800\,\mathrm{nm})$			2.25
for light polarized in the ab plane:			
$\omega_{\mathrm{TO}}/2\pi$			4.3 THz
ϵ_{dc}			41.5
ϵ_{∞}			17.4
$n(\lambda = 800\,\mathrm{nm})$			2.25

Table 8.1: Structural and optical properties of $LiTaO_3$

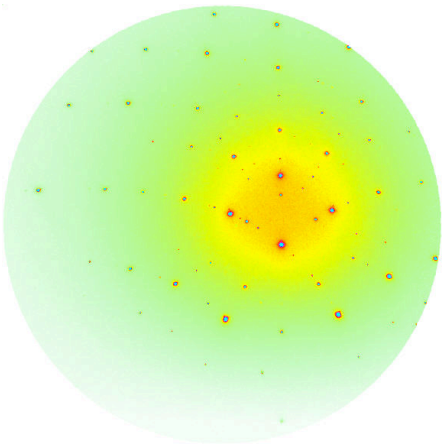

Figure 8.4: The Laue diffraction pattern from $LaTiO_3$.

and A_1 mode respectively, therefore, their effect on the diffraction signal needs to be measured with femtosecond X-rays. As the flux of femtosecond sources can be low, it is important to choose an intense diffraction peak so that good signal-to-noise statistics can be obtained. In order to simplify the analysis of the diffraction data, diffraction peaks which are only sensitive to displacements along a single crystallographic direction should be measured. Both of these conditions are met with the (006) diffraction peak, which is only sensitive to displacements along the c-axis. The crystal was orientated by measuring the Laue diffraction which is shown in figure 8.4.

8.4.2 Generation of THz waves from ISRS

As the frequencies of the lowest transverse optical phonons are 4.3 and 6.1 THz (see table 8.1), low frequency THz waves are needed in order to couple to the structural modes. However, as these waves are close to the resonance, the reflectivity is high and little energy will propagate into the material.

The nonlinear optical properties of $LiTaO_3$ make it a suitable material for generating THz frequency waves inside the material. As the space group $R3c$ does not contain a center of inversion, the electronic second order non-linear susceptibility tensor will contain non-zero components. In such a case the initial electric field displaces the electrons relative to the lattice creating a polarization from a bound dipole. This polarization mixes with a second electric field, or a different frequency component within the same field, and can produce

radiation at the difference-frequency of the two electric fields, as described in chapter 3.

An interesting aspect of the $R3c$ space group is that all Raman active modes are also IR active. As a result it is also possible to generate THz radiation from impulsive stimulated Raman scattering (ISRS - described in chapter 3). In this case, the first pulse undergoes Raman scattering to produce a Stokes scattered photon and a phonon with amplitude Q. As all the phonons are IR active, this will produce a polarization of the material due to the ionic motion. Similarly, a second frequency component can mix with the induced ionic polarization to produce low frequency radiation.

These two processes can be described as the non-linear polarization [125, 133],

$$P_i^{NL} = \chi_{ijk}^{(2)} E_j E_k + \chi_{ijk}^{R} Q_j E_k = \chi_{ijk}^{(2)} E_j E_k + \chi_{ijk}^{R} \beta_j E_j E_k, \tag{8.9}$$

where χ^2 is the second order electronic susceptibility, χ^R is the Raman susceptibility and β is the scattering cross-section for creation of a phonon with amplitude Q from an electric field E.

In $LiTaO_3$, the electronic susceptibility is significantly smaller than the Raman term [133] and, therefore, the non-linear polarization can be approximated as by the ionic susceptibility only as

$$P^{NL} \approx \chi_{ijk}^{NL} E_j E_k. \tag{8.10}$$

Therefore, as $LiTaO_3$ is transparent to near-IR radiation, broadband 800 nm pulses can be used to generate THz frequency radiation within the crystal.

8.4.3 Experimental setup

Experiments were performed at the Advance Light Source synchrotron on Beamline 5.3.1. Femtosecond X-rays were generated using the slicing technique (see chapter 3). The sliced femtosecond electron bunch generated broad-bandwidth femtosecond X-rays in a bend magnet. The resulting radiation was imaged onto a Si-111 monochromator by a toroidal silicon mirror. The monochromator was used to select monochromatic femotsecond X-rays at 7 keV from the broad bandwith generated by the bend magnet. The X-rays were focused onto $LiTaO_3$ to give an elliptical spot size of 200 μm x 170 μm. The repetition rate of the system is set by that of the laser to 2 kHz. After slicing, the femtosecond X-rays are four orders of magnitude less intense than the full picosecond bunch, resulting in a few thousand photons per

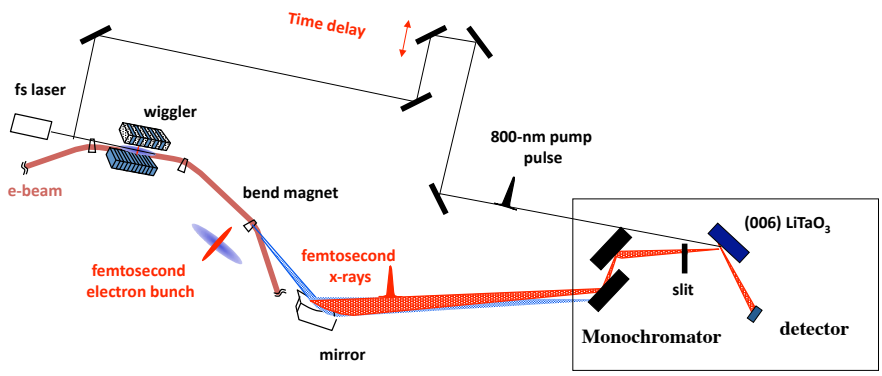

Figure 8.5: A sketch of the slicing experiment used to measure phonon-polaritons with femtosecond X-rays.

second per 0.1% bandwidth. After diffraction a few 100 photons per second were detected by an avalanche photo-diode placed in the Bragg condition. A sketch of the experimental setup is shown in figure 8.5. The $LiTaO_3$ crystal was $2 \times 2 \times 5$ mm in size cut with the c-axis perpendicular to the surface. Using 7 keV X-rays, the Bragg condition required the X-rays to arrive at an angle of 68° relative to the surface normal in order to observe the 006 diffraction peak.

A fraction of the laser used to slice the electron beam was separated by a beam splitter and used as a pump beam to generated the phonon-polaritons. This enabled exact synchronization between the generated femtosecond X-rays and the phonon-polariton excitation. The temporal overlap of the two beams was obtained by a cross-correlation measurement between the 800 nm pump beam and the residual femtosecond visible light generated by the bend magnet. The cross-correlation was measured by two photon absorption in a SiC diode. As a result of electron-electron interactions and the dispersion of the bend magnet, the resulting pulse length of the sliced X-ray beam was measured to be 200 fs. In order to maintain temporal overlap with the X-rays, the laser beam followed a collinear path and also entered the material at 68° which allowed the maximum sampling of the THz wavefront. The polarization of the pump beam was within the plane of the surface normal (p polarized), which allowed excitation of both the A_1 and E symmetry optical phonons. To ensure the X-ray probe measured a homogeneously excited region of the material, the laser was focused to a circular spot with a 1 mm diameter. The pump fluence at the sample surface was 10 mJ cm^{-2}

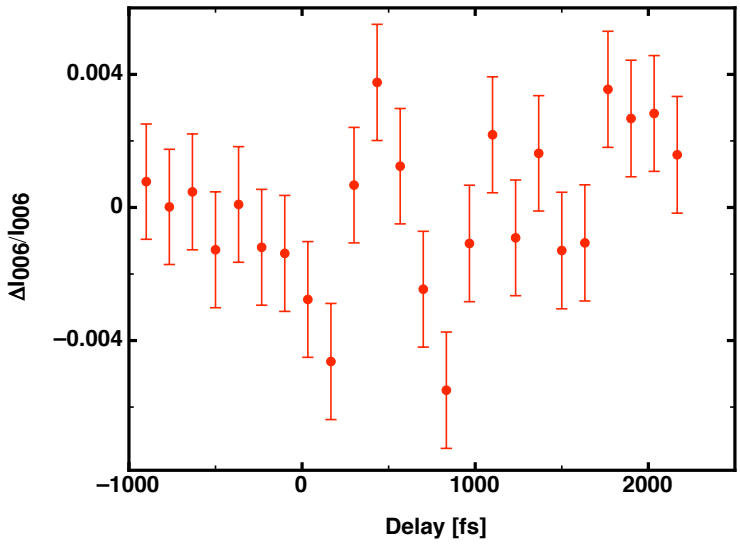

Figure 8.6: Relative change $(\Delta I_{006}(t)/I_{006}(0))$ of the diffraction peak as a function of pump-probe time delay.

to ensure that large amplitude oscillations were induced.

Figure 8.6 shows the measured diffraction signal as the pump beam was delayed relative to the X-ray bunch. Measurements were taken in a photon-counting regime using a discriminator. The error bars represent the standard error (standard distribution divided by the square root of the number of measurements taken) of the total number of counts at each time point. The signal-to-noise is low, making interpretation of the data difficult without comparing it to the theoretical expected signal.

8.5 Simulation of phonon-polaritons

8.5.1 Phonon-polaritons propagation and Maxwell's equations

In order to calculate the ionic displacements caused by the propagation of phonon-polaritons in $LiTaO_3$, Maxwell's equations need to be solved in the geometry set by the experiment. The solutions of these equations give values for the normal mode coordinates as a function of time. From these values, the ionic displacements can be evaluated and used for the calculation of the diffraction signal.

As the solution to Maxwell's equations for the geometry required by the experiment are

not analytic, a numerical solution is needed. The most appropriate, and computationally simple, method to solve time-dependent wave equations is the Finite Difference Time Domain (FDTD) technique. The technique breaks up space and time into discrete network of grid points and solves the equations in an iterative fashion.

The following equations describe temporal and spatial propagation of the phonon-polariton,

$$\nabla \times \boldsymbol{E} = -\mu_0 \dot{\boldsymbol{H}}, \tag{8.11}$$

$$\nabla \times \boldsymbol{H} = \dot{\boldsymbol{D}}, \tag{8.12}$$

$$\boldsymbol{D} = \epsilon_0 \boldsymbol{E} + \boldsymbol{P}, \tag{8.13}$$

where $\boldsymbol{H}$ is the magnetic field, μ_0 is the permeability of free space and $\boldsymbol{D}$ is the displacement field. The polarization vector, $\boldsymbol{P}$, is defined in equation 8.2, however, as $LiTaO_3$ is not isotropic, the b coefficients along the c direction are different to the coefficients in the ab-plane.

The ionic displacements are used to calculate $\boldsymbol{P}$ in the same way as used in the derivation of equation 8.3, however, a phonon-damping term, Γ is added to account for energy loss due to mixing of phonon modes. In addition, a nonlinear term in the electric field is used to account for the phonon amplitude generated from IRIS. The displacement of the ions can then be described as,

$$\ddot{w}_i + \Gamma \dot{w}_i = b_{11i} w_i + b_{12i} E_i + \alpha_{ijk} E_j E_k, \tag{8.14}$$

where the subscripts i, j, k refer to the directions ($i = x, y, z$) along the crystal axis, in order to take into account and anisotropic nature of $LiTaO_3$. α is the non-linear coupling term of the electric fields which produce the THz radiation from ionic displacements. Solving equations 8.2 and 8.14 with plane waves gives the non-linear polarization as,

$$P_i = \chi_{ii}(\omega) E_i + \chi^{NL}_{ijk}(\omega) E_j E_k,$$

with

$$\chi_{ii}(\omega) = b_{22i} + \frac{b^2_{21i}}{\sqrt{\omega^2 - \omega^2_{\mathrm{TO}i} + i\Gamma\omega}}, \tag{8.15}$$

and

$$\chi^{NL}_{ijk}(\omega) = \frac{b_{21i}\alpha_{ijk}}{\sqrt{\omega^2 - \omega^2_{\mathrm{TO}i} + i\Gamma\omega}}. \tag{8.16}$$

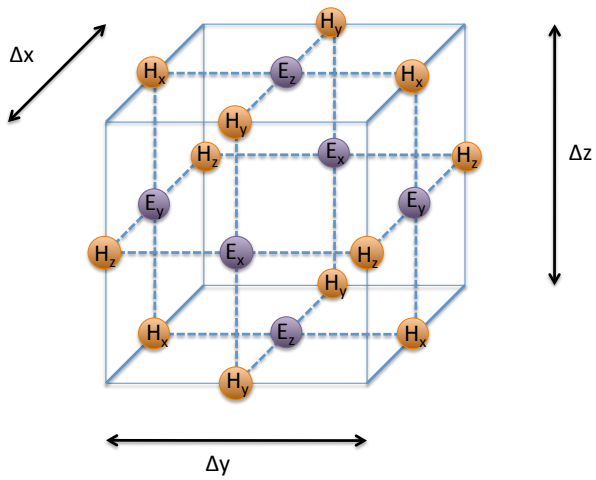

Figure 8.7: The discretization of the electromagnetic field using a Yee cell. The cell has the dimensions $\Delta x \times \Delta y \times \Delta z$

8.5.2 The Finite Difference Time Domain technique

The discretization of equations 8.11-8.14 was achieved using a Yee cell [134]. A Yee cell consists of a discrete volume of space with dimensions $\Delta x \Delta y \Delta z$, within which the magnetic field is physically offset from the electric field by half a grid point. This is a natural result of the curl operation. For example, the z component of the curl of the magnetic field used to calculate the electric field at the point $((i+\frac{1}{2})\Delta x, (j+\frac{1}{2})\Delta y, k\Delta z)$ in a discrete space is:

$$\hat{\boldsymbol{z}}.\boldsymbol{\nabla} \times \boldsymbol{H}\big|_{i+\frac{1}{2},j+\frac{1}{2}+k} = \left[\frac{Hy\big|_{i+1} - Hy\big|_{i}}{\Delta x}\right]_{j+\frac{1}{2},k} - \left[\frac{Hx\big|_{j+1} - Hx\big|_{j}}{\Delta y}\right]_{i+\frac{1}{2},k}. \tag{8.17}$$

As the electric field is related to $\boldsymbol{\nabla} \times \boldsymbol{H}$, it is obvious the the electric field should be offset from the magnetic field for numerical accuracy. A Yee cell is shown in figure 8.7 which locates the electric and magnetic field components at the appropriate points within a cell of the simulated space. The temporal evolution of the electric and magnetic fields are also displaced by half a time step resulting in a 'leap frog' evolution, again for numerical stability.

Equation 8.14 is second order differential equation which has to be converted to two first first order equations. This is achieved by using the substitution $\boldsymbol{v} = \dot{\boldsymbol{w}}$, which gives the following four field equations:

$$\boldsymbol{\nabla} \times \boldsymbol{E} = -\mu_0 \dot{\boldsymbol{H}}, \tag{8.18}$$

$$(\epsilon_0 + b_{22})\dot{\boldsymbol{E}} = \boldsymbol{\nabla} \times \boldsymbol{H} - b_{12}\boldsymbol{v}, \tag{8.19}$$

$$\dot{\boldsymbol{v}} = -\Gamma\boldsymbol{v} + b_{11}\boldsymbol{w} + \alpha\boldsymbol{E}\boldsymbol{E} + b_{21}E, \tag{8.20}$$

$$\boldsymbol{v} = \dot{\boldsymbol{w}}. \tag{8.21}$$

Here $\alpha\boldsymbol{E}\boldsymbol{E}$ is taken to be the vector formed by $\sum_{j,k} \alpha_{ijk}E_jE_k$. Numerical consistency requires that the $\boldsymbol{v}$ field has the same spatial and temporal offset as the $\boldsymbol{H}$ field.

The temporally discrete forms of the equations, which enable the calculation of the fields at a time $(n+1)\Delta t$ given a field at a time $n\Delta t$, are:

$$-\mu_0\frac{(\boldsymbol{H}^{n+\frac{1}{2}} - \boldsymbol{H}^{n-\frac{1}{2}})}{\Delta t} = \boldsymbol{\nabla} \times \boldsymbol{E}^n, \tag{8.22}$$

$$(\epsilon_0 + b_{22})\frac{\boldsymbol{E}^{n+1} - \boldsymbol{E}^n}{\Delta t} = \boldsymbol{\nabla} \times \boldsymbol{H}^{n+\frac{1}{2}} - b_{12}\boldsymbol{v}^{n+\frac{1}{2}}, \tag{8.23}$$

$$\frac{\boldsymbol{v}^{n+\frac{1}{2}} - \boldsymbol{v}^{n-\frac{1}{2}}}{\Delta t} = -\Gamma\frac{\boldsymbol{v}^{n+\frac{1}{2}} + \boldsymbol{v}^{n-\frac{1}{2}}}{2} + b_{11}\boldsymbol{w}^n + \alpha(\boldsymbol{E}^n\boldsymbol{E}^n + \boldsymbol{E}_p^n\boldsymbol{E}_p^n) + b_{21}\boldsymbol{E}^n, \tag{8.24}$$

$$\frac{\boldsymbol{w}^{n+1} - \boldsymbol{w}^n}{\Delta t} = \boldsymbol{v}^{n+\frac{1}{2}}. \tag{8.25}$$

The curl operator is defined by equation 8.17. In these equations, the electric field of the pump beam, $\boldsymbol{E}_p$, has been separated from the field of the THz radiation. This separation allows the pump beam to act as the initial conditions for the simulation and, in order to improve the performance of the simulation, the propagation of the pump beam is not governed by the above equations.

The evolutions of the fields can be visualized in the control diagram shown in figure 8.8 and shows the order in which the operations should be performed.

8.5.3 Simulation details

As the propagation and polarization of the pump beam was in the *ac*-plane, there were seven non-zero spatial fields consisting of: $E_a, E_b, H_b, Q_a, Q_c, \dot{Q}_a$, and $\dot{Q}_c$, where a, b, c refer

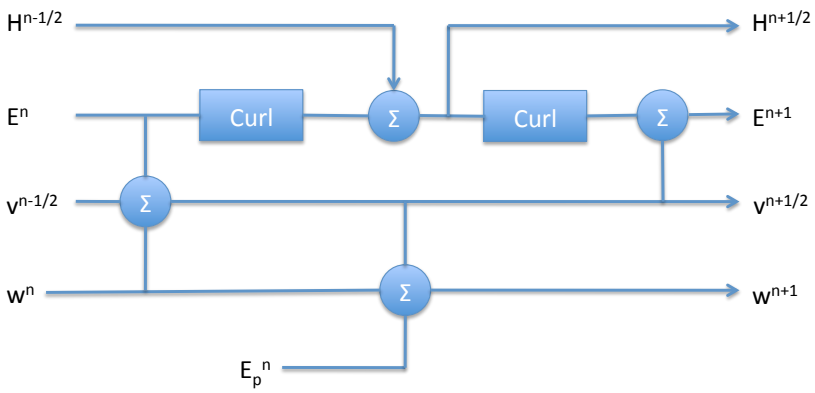

Figure 8.8: The control sequence for the evolution of equations 8.22-8.25. Time flows from left to right. Multiplication factors are not shown.

to the crystal axis directions. For numerical stability and good numerical convergence, the simulation space is usually discretized in to steps which are $\Delta x \ll \lambda$, where λ is the shortest wavelength in the system. Similarly $\Delta t \ll 1/f$, where f is the frequency of the most rapid oscillation [135]. Typical wavelengths IR wavelengths generated by ISRS in $LiTaO_3$ are $\approx$ 100 μm in vacuum. Therefore, for good convergence and stability, a grid size from 1-10 μm was used with a 30 fs step size.

One drawback of the FDTD technique is the problem encountered by the equations at the edges of the simulation space. As the spatial extent of the simulation is finite, the curl operator cannot be applied at the edges. In oder to over come this restriction, assumptions have to be made on the nature of the $\boldsymbol{E}$ and $\boldsymbol{H}$ fields at the boundary. The simplest assumption is that both fields have zero strength at the edge. However, this leads to large reflections of waves at the boundary, which can interfere with subsequent wave propagation in the simulated region and numerical instability.

There are two strategies to overcome this problem. If the size of the simulation space is increased the time taken for a propagating wave to reach the boundary will be longer, and effects from the reflection can be ignored. However, increasing the simulation size dramatically increases the computational load and is only viable if the region of interest is relatively small. Another method is to add a buffer layer around the simulation which is impedance matched to the enclosed simulation region, so there is no reflection from the boundary, but is also attenuating so that the fields are brought to zero smoothly. Such a region is known as a

perfectly matched layer, or PML layer, and is used in the simulations presented here [136].

To simulate the experimental setup, which starts with a 1 mm diameter pump beam initially outside of $LiTaO_3$, a system with a minimum size of 3 mm × 2 mm in size was needed. Using double precision (32-bit) to store the numerical values of each field at each point in space requires approximately 100 MB of computer memory. As the simulation requires approximate 100 time steps to complete approximately 10 GB of data are generated.

If the propagation of the 800 nm beam was described by equations equations 8.22-8.25 the grid would have to be significantly finer and, as a result, require significantly more computer resources. Therefore, in order to relax this requirement, the evolution of the pump beam was not evolved according to Maxwell's equations. Instead the pump pulse is modelled with a Gaussian spatial and temporal profile and is set to follow the path described by ray optics, with refraction due to Snell's law occurring at the interface between the vacuum and $LiTaO_3$. It was assumed that the intensity of the 800 nm pump beam remains constant and it does not disperse.

Equations 8.22-8.25 are first order differential equations, therefore, one boundary condition for each equation is needed. The boundary conditions for this experiment are governed by the pump beam which is used to create the THz field. Therefore, all the fields and their derivatives are set to zero at the start of the simulation. The pump beam will then trigger the generation of coherent polaritons by equation 8.24 when it enters the material.

8.5.4 Polariton propagation results

Figure 8.9 shows the results of a coarse simulation ($\Delta x = 5\,\mu$m) at one point in time. The z and x axis are defined by the crystallographic c and a axis respectively. The false-colour image represents the magnitude of the z component of the ionic displacements, $\boldsymbol{w}$. Dark red represents large displacements and dark blue represents zero displacement. The black and white dashed lines show the path followed by the pump beam. The pump enters the medium with an angle 68° to the surface normal and is refracted to an angle of 24°. The polarization of the pump beam is within the plane, therefore IR active phonons can be generated with motions along the a and c directions.

The simulation results show that two THz frequency waves are created in the material. One wave is generated by the 800 nm in the bulk of the $LiTaO_3$ and follows in the wake due to

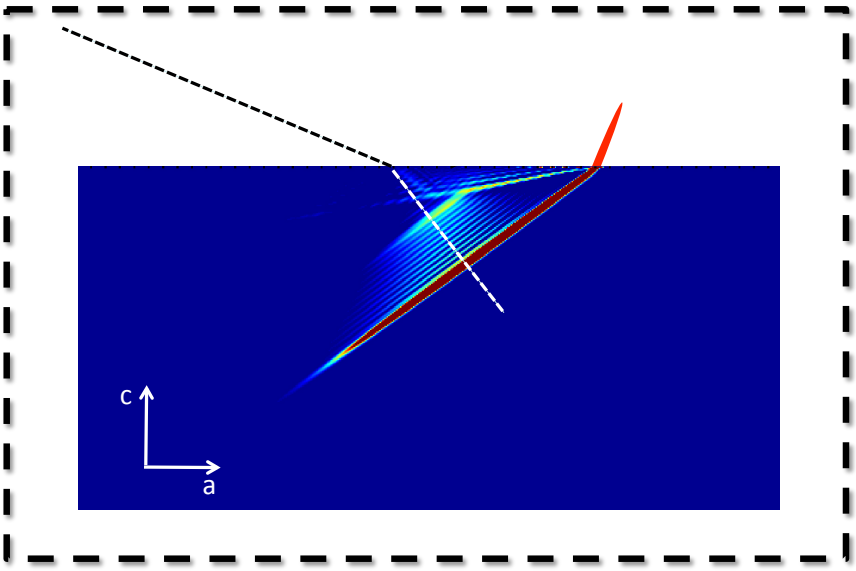

Figure 8.9: A snapshot of the simulation performed on a coarse grid size. The thick black dashed line indicates the size of the simulated region. The thin black and white dashed line indicated the path of the pump beam as it propagates inside the medium. The pump beam is only shown outside the material as a red ellipse. The blue region represents a colour map of the phonon field with amplitude along the c-axis.

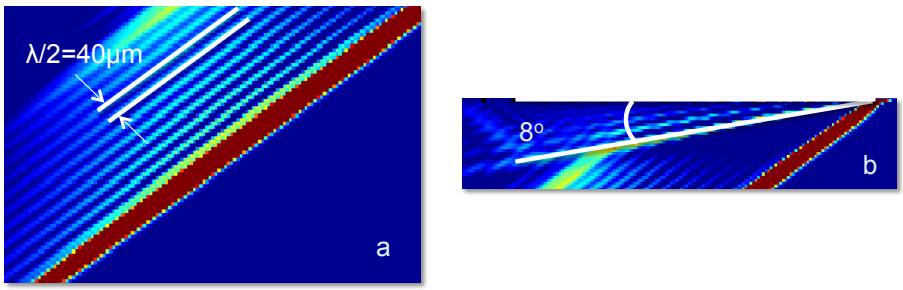

Figure 8.10: An expanded view of the simulation. a) The polaritons generated in the wake of the 800 nm pump pulse. b) Cherenkov radiation emitted from the surface of $LiTaO_3$

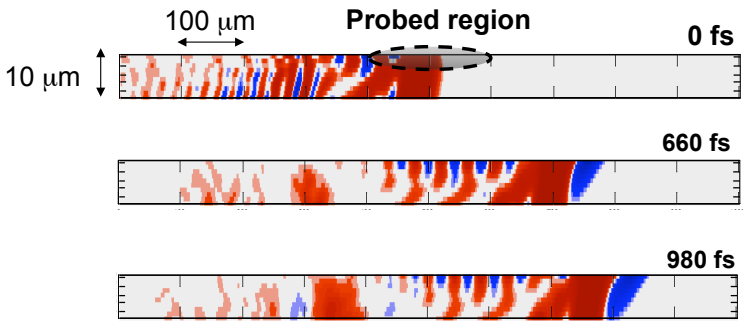

Figure 8.11: High resolution simulation of the c-axis component of phonon-polariton field at the surface of $LiTaO_3$.

the higher index of refraction at THz frequencies and, therefore, slow propagation speed. The wavelength can be measured directly from the simulation as shown in Figure 8.10a, which shows that the 800 nm pump beam generated radiation at 80 μm inside the material.

The second wave is created at the interface between the $LiTaO_3$ and the vacuum and propagates at an angle of 8° to the surface normal, as shown in figure 8.10b. The second wave is the result of Cherenkov radiation generated from a 'point-like' source that is moving along the surface of the crystal with an apparent superluminal velocity. In a time Δt, the pump beam has travelled a distance $c\Delta t$. However, as the beam is not traveling parallel to the surface the distance between the intercept point is given by $\frac{c\Delta t}{\sin\,\theta}$, where θ is the angle the pump beam makes to the surface normal. From this, it can be seen that the surface point moves with an apparent speed $\frac{c}{\sin\,\theta}$. For $\theta = 68°$, as in the experimental setup, the source term moves across the surface has the superluminal speed $1.08c$. The angle of the emitted Cherenkov radiation is given by the equation,

$$\cos\,\phi = \frac{1}{n\beta},$$

where ϕ is the angle taken from the direction of propagation, n is the refractive index of the material and $\beta = \frac{v}{c}$ is the speed of the source term divided by the speed of light in vacuum. From table 8.1, $n \approx 6.1$ which gives an angle $\phi \approx 82°$ to the direction of propagation, or 8° to the surface normal, in agreement with the angle observed in the simulation.

8.5.5 Simulation of diffraction signal

In order to calculate the diffraction signal a simulation with higher, 1 μm, spatial resolution was performed. The results obtained at three time points in time are shown in figure 8.11. The shaded area of the figure corresponds to the region over which the beam is diffracted.

The positions of the ions were calculated by applying the $R3c$ space group operations to the non-equivalent ionic positions given in table 8.1. This gives a conventional unit cell consisting of 16 molecular units. From this the intensity of the static (006)-diffraction peak can be calculated using equation 8.8 and the atomic scattering factors in table 8.2.

The 006 diffraction signal is insensitive to displacements along the a or b axis, therefore, only the displacements along the c axis need to be added to the equilibrium positions. The z-component of the ionic displacements can be written as,

$$w_z = \sqrt{\mu}(z_+ - z_-), \tag{8.26}$$

where $z_\pm$ is the displacement of the positive and negative centre of masses from their equilibrium positions. Therefore, the negative component corresponds to the displacement of the negatively charged oxygen planes in order to calculate the time dependent intensity. The displacement of the positive ions is given by

$$z_+ = \frac{m_{\mathrm{Ta}}}{\mu_+} z_{\mathrm{Ta}} + \frac{m_{\mathrm{Li}}}{\mu_+} z_{\mathrm{Li}}, \tag{8.27}$$

where μ_+ is the reduced mass of the positive ions.

As no momentum transfered between lattice sites, the centre of mass of the unit cell does not change, therefore,

$$3m_{\mathrm{O}} z_{\mathrm{O}} + m_{\mathrm{Ta}} z_{\mathrm{Ta}} + m_{\mathrm{Li}} z_{\mathrm{Li}} = 0. \tag{8.28}$$

Combining equations 8.26, 8.27 and 8.28 gives the displacement of the oxygen ions as

$$z_{\mathrm{O}} = \left(\frac{3m_{\mathrm{O}}}{\mu_+} + 1 \right)^{-1} \frac{w_z}{\sqrt{\mu}}. \tag{8.29}$$

The position of the Ta and Li ions cannot be determined uniquely from the equations above, therefore, it is assumed that $z_{\mathrm{Li}} = \eta z_{\mathrm{Ta}}$, where $\eta > 0$, is a parameter obtained by fitting the simulation results to the measured diffraction signal.

The state of the material at a given time, from the view point of the simulation, is not the same as that experienced by the X-rays. This is shown in figure 8.12. The measured

Element	f	f'	Mass (u)
Li	3.00164	0.465936E-03	6.941
Ta	68.5396	6.86032	180.9479
O	8.06642	0.457894E-01	15.9994

Table 8.2: Atomic form factors at 7 keV [137] and atomic masses [138]

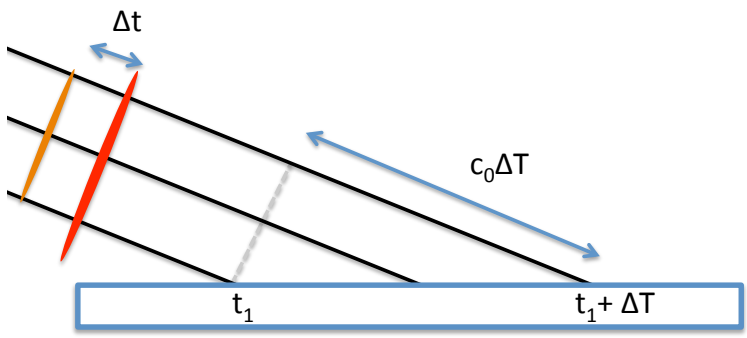

Figure 8.12: An illustration of the time difference between the simulation time and the pump probe time delay. The pump beam is represented by the red ellipse. The X-ray probe beam, which is delayed by a time Δt, is represented by the orange ellipse. For a fixed time delay between the pump and probe, X-ray beam samples the surface over a range of times in the simulation frame of reference.

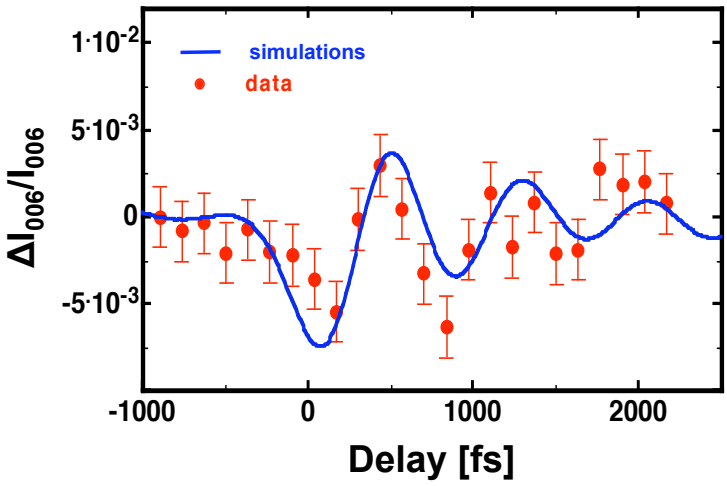

Figure 8.13: The time dependent fit of the fractional change in 006 diffraction intensity to the experimentally measured quantity.

diffraction signal, shown in figure 8.6, is a function of pump-probe delay (Δt in figure 8.12). As a result, X-rays a distance x from the centre of the X-ray beam will arrive at a time $\Delta T = \frac{x \tan\theta}{c}$, where $\theta = 68°$ is the angle the X-rays make to the surface normal. Therefore there is a 1.7 ps time difference between the arrival of the two edges of the X-ray beam.

After the simulation of the diffraction data has finished, the data is re-ordered into the frame of reference of the X-ray probe. The displacements, $\boldsymbol{w}_z$, from each of the discrete spatial regions are used to calculated the diffraction pattern with a given η. The signal from each region was weighted by the spatial and temporal profile of the gaussian X-ray pulse to give an average signal. This procedure was repeated for all X-ray-laser time delays in order to calculate the diffraction signal and the process was then repeated after varying η until the best fit to the data was found.

8.6 Comparison of the simulation and data

Figure 8.13 shows the resulting relative change in 006 diffraction signal after fitting to the measured value. The structure factor is observed to oscillate at a heavily damped frequency of ≈ 1.5 THz, which is typical of the THz frequency oscillations generated in $LiTaO_3$. The calculated signals correspond well to the measured diffraction data, showing a sine-like dependence as expected for phonons generated with ISRS. By fitting the amplitude of the simulated

oscillations to the data a maximum displacement of approximately 5 mÅ was obtained for the displacement of the Ta ion relative to the Oxygen plane. This result demonstrates the first measurement of the mechanical component of the electromagnetic wave as it propagates in a dielectric material.

The numerical simulation of the phonon-polariton propagation was necessary for the interpretation of these data due to the significant noise. However, the simulations also point to ways in which the experiment can be improved in order to increase the measured signal. A significant increase could be obtained by changing the angle between the X-ray and laser path. In the experiment discussed in this chapter, the X-ray and laser beam arrive collinear. On entering the $LiTaO_3$ sample, the 800 nm laser pulse is refracted and results in a deflection of 44° from the X-ray propagation direction. As a result, the polariton wavefront is not parallel to the probing X-rays and a spatially non-uniform displacement is probed, which reduced the total signal. If the X-ray and polariton wavefronts were matched, the X-rays would diffract from a more homogeneous displacement and produce a larger signal.

Matching the wavefronts of the laser beam and X-ray beam is difficult. The X-ray angle is set by the Bragg condition for diffraction and, therefore, cannot be changed. In addition, the maximum angle that the 800 nm beam can propagate into the material is 26° due to Snell's law, significantly less than the 68° that the X-rays propagate at. To overcome this, the intensity wavefront of the laser beam could be tilted with respect to the propagation direction in order to match the wavefronts inside the material [139], whist maintaining the current experimental geometry.

Another important consideration is the modulation of the structure faction with respect to the phonon coordinate. Although the 006 diffraction peak is an intense scatterer of 7 keV X-rays, the amplitude change with respect to the phonon mode is relatively low. This is because the Ta ion is very heavy and only moves a small distance with respect to the Oxygen plane. The Ta ion provides the majority of the diffraction intensity due to its large atomic scattering factor, therefore it's small displacement results in a small change in the scattering factor. The lighter Li ion moves a large distance, but the low atomic form factor results in a small modulation in the signal. By performing a complete analysis of the variation of scattering factor with respect to the phonon mode, the peak with the highest intensity modulation could be identified and used in future measurements.

This experiment can be expanded by measuring additional diffraction spots, enabling a complete reconstruction of the material's response without making any assumptions on the normal mode motion. To date, normal modes are assigned frequencies based on estimates of bond strengths inside the material. By measuring in this way, these assignments can be verified. Being able to completely reconstruct the ionic motions would also enable the study of the affects of anharmonicity on the normal mode. This would be particularly interesting for the study of the phonon modes in the vicinity of the ferroelectric to paraelectric phase transition, driven either by temperature or by intense polariton propagation.

Chapter 9

Summary and outlook

9.1 Summary of thesis

This thesis has presented time-resolved experimental data on photo-induced non-equilibrium dynamics of correlated materials. The thesis has demonstrated and combined two fundamental requirements in this field, namely the dynamics that are under study should be excited on a timescale that is prompt when compared to their subsequent evolution and that the response of the material should be probed in regions of spectral interest i.e. regions of the material's spectrum that are well characterized by the affect being induced and measured.

The combination of these two requirements is not trivial, requiring short pulses of probe light to be generated over a wide range of wavelengths or energies. To this end, this thesis has discussed the generation of, and presented results that have used, femtosecond pulses to probe an energy range covering four orders of magnitude, from 0.7 eV to 7 keV.

9.1.1 Dynamics in a 1D Mott insulator

Chapter 4 demonstrated these principles in the case of the non-equilibrium dynamics in the 1D Mott insulator (BEDT-TTF)-F_2TCNQ. By exciting and probing the Mott gap, the many-body dynamics of the correlated electrons could be observed. The cornerstone of this measurement was the use of an ultra-broad-bandwidth source centred around 0.7 eV, enabling the dynamics to be observed with a temporal and spectral resolution an order-of-magnitude better than had been previously possible [80].

The high temporal and spectral resolution enabled the dynamics to be compared to a

many-body quantum calculation. In particular, it was found that both the static and dynamic properties of this material are best replicated by the introduction of a V term in the Mott-Hubbard Hamiltonian, representing nearest neighbour interactions between vacant and doubly occupied lattice sites. This enabled a picture of electron delocalization to emerge.

This technique could be used to probe correlation-induced gaps in other correlated materials, such as high-T_C superconductivity. By measuring and modeling the dynamics at the gap, the terms in the Hamiltonian that effect the dynamical properties of the material can be identified. This would provide an important step in verifying which terms in the Hamiltonian are needed in order to represent high-T_C superconductors.

9.1.2 Dynamics in manganites

Chapters 5-7 discuss the dynamics observed in the manganites at the charge transfer resonance, located in the visible spectral region, and at the oxygen $K-$ and manganese L-edgess, in the soft X-ray spectral region.

By exciting $LaMnO_3$ at the charge transfer resonance, coherent lattice vibrations could be induced which were observed by their influence on the reflectivity. By measuring the damping rate of the lattice vibrations as a function of initial temperature, coupling between the charge, lattice, spin and orbital degrees of freedom could be indentified. This result was only possible with the use of short, sub-10 fs, pulses which could excite the dynamics coherently.

The coupling between the multiple degrees of freedom could be explained by returning to the Goodenough-Kanamori rules, which can be used to describe the static orbital and magnetic ordering in the manganites. By considering the excitations induced by the pump laser beam, a qualitative description of the dynamics could be obtained by considering a photo-induced change in the local magnetic-exchange constant and bond energy. The mechanism is general for all manganites and may explain how photo-excitation can drive metallic and magnetic state formation in doped manganites [24, 75].

Similar experiments were also performed in the doped manganite $Pr_{0.7}Ca_{0.3}MnO_3$. This compound is known to exhibit a photo-induced insulator-metal phase transition [24]. By measuring the damping rate of the phonons together with the formation rate of the quasi-stable state, a formation time of under 100 fs was deduced for the phase transition.

The metallic nature of the quasi-stable state was confirmed by time-resolved measurements

of the X-ray absorption spectra at the oxygen K-edge and manganese L-edges. Although the time resolution of this measurement was not sufficient to observe the dynamics of phase transition, the quasi-stable state was shown to undergo similar shifts in spectral weight as observed in manganites that exhibit a thermally driven phase transition. An obvious extension of this work would be to probe the X-ray signal with sub-100 fs resolution in order to resolve the transition between the two states.

The other surprising observation that emerge as a direct result of using short pulses was the possible observation of the orbiton. The nature of these particles and their possible link to a photo-induced metallic phase in $Pr_{0.7}Ca_{0.3}MnO_3$ remains controversial, and further experimental and theoretical work is required to clarify many remaining issues as outlined in chapter 6. Many other materials also exhibit orbital ordering, and it would also be interesting to see if the quasi-particle can be observed in different systems.

9.2 Future directions

There are many interesting new avenues to pursue in this area of ultrafast science. Both with samples discussed here and with other correlated materials. These include the application of other established techniques to extend the region over which the out of equilibrium dynamics can be measured in materials as well as the use of new sources and emerging techniques.

For example, time domain THz spectroscopy is an established technique that can be used to measure low energy excitations in materials. It would be particularly interesting to use the technique to measure the low energy response of the excitations in photo-excited (BEDT-TTF)-F_2TCNQ. The measurements could be compared to the predictions of the low-energy dynamics from the quantum model proposed to describe the dynamics of the Mott gap, and may point to directions in which the model can be improved.

These experiments would also be interesting to apply to the manganites in order to reveal the dynamics of the conducting electrons in the photo-induced insulator-metal transition.

Newly emerging techniques, such as time and angle-resolved photoemission will also give complimentary information such as the photo-induced change in Fermi-surface [10, 140]. This will be particularly interesting for photo-induced insulator-metal transitions, as they have the potential to show the regions of the Brillouin zone where the insulating gap collapses.

New sources also present new opportunities for studying correlated materials. Future free

electron lasers should provide high photon-flux at X-ray energies, with pulses much short than that which are currently available. These new sources would bring many benefits to the experiments discussed in chapters 7 and 8, improving both the signal, due to the brighter source, and the time resolution.

The improvements in the time resolution would also enable many important structural dynamics that cannot yet be captured, such as the distortions that are associated with the Jahn-Teller phonon in the manganites. This thesis has shown that this phonon-mode is of particular importance in the manganites, therefore, dynamics need to be probed on a similar timescale to the associated atomic motions.

Another new direction is to develop is the pump source. Very recently it has been shown that an insulator-metal phase transition can be induced by exciting an IR active phonon [27]. The same technique has also been used to melt orbital order in a different material [45]. These experiments suggest new ways to control and excite complex materials, and enable a new method to investigate the coupling between multiple degrees of freedom. With future developments of IR free electron lasers and improvements in laser techniques, generation of intense probes at a wide range of energies will become available, promoting more interest in this field.

Appendix A

Synchronization and timing between laser and X-ray sources

The following describes the synchronization between the laser and X-ray sources at the Advanced Light Source (ALS), Lawrence Berkeley National Laboratory, which is required for femtosecond and picosecond X-ray measurements.

One femtosecond titanium sapphire laser oscillator is used to seed two amplifiers and is electronically synchronized to the storage ring orbit clock of the synchrotron. One amplifier is used to slice the electron beam and generate femtosecond X-rays (see chapter 3), and the second amplifier is used to generate the pump, which is used to excite the sample. The amplifiers can run at a 1-4 kHz repetition rate and the oscillator pulses are selected by a Pockels cell. The common oscillator to both amplifiers ensures absolute synchronization between the slicing laser and the pump laser.

The ALS runs in a multi-bunch structure. The ring cavity consists of 320 RF 'buckets' separated by 2 ns. Each bucket is filled with electrons to produce a quasi-cw X-ray source. In order to perform timing measurements, one bucket, the 'camshaft', is filled with significantly more electrons than the quasi-cw multi-bunch. In addition, the buckets in the vicinity of the camshaft are left empty, resulting in an intense burst of X-rays in the middle of a 20 ns dark 'window'. With the use of fast detectors and gated amplifiers, such as a box car integrator, the camshaft signal can be separated from the signal produced by the multi-bunch.

Temporal overlap between the laser and the X-rays can be achieved by measuring the arrival time of each pulse on a fast avalanche photo diode (APD). The APD is biased with

200 V and the signal was amplified by a fast pre-amplifier. Biasing the APD increases the response time of the diode light irradiation produced a signal with a rising edge time constant of approximately 1 ns. The APD signal was resolved on a fast 2 GHz oscilloscope which was externally triggered by the storage ring orbit clock signal used to synchronize the oscillator. The arrival time of the signal was defined as the point in time at which the signal reached the half its maximum value, relative to the trigger signal. Measuring the difference in arrival time between the signal generated by the picosecond X-ray bunch and the femtosecond laser, enables the delay between X-rays and the laser to be determined.

The X-ray beam path is fixed, therefore changes in the delay must be made to the laser path. The arrival time of the laser can be controlled with three techniques. Coarse timing can be achieved by changing the timing on the Pockels cell used to select the pulses for the amplifiers from the oscillator. The oscillator produced pulses which were separated approximately 8 ns, therefore changing the timing of the Pockels cell shifts the laser time by integer multiples of 8 ns.

Finer resolution timing can be achieved by changing the output phase of the oscillator. Changing the oscillator phase changes the time at which the laser pulse leaves the cavity relative to the storage ring orbit clock. By momentarily adjusting the length of the oscillator the time at which can the pulse leaves the cavity can be changed. The accuracy to which the phase can be controlled is approximately 1 ps.

The finest resolution is achieved by moving a retro reflective mirror on a motorized delay state. The stage could be controlled with a precision of less than 1 μm, allowing the timing to be adjusted in less than 5 fs steps. The above techniques were used to adjust the arrive time of the laser until the laser and X-ray generated APD signals were temporally overlapped on the oscilloscope and allowed time zero to be determined to within $\sim$500 ps.

Bibliography

[1] Wikipedia. Eadweard Muybridge — Wikipedia, the free encyclopedia, 2004. URL `http://en.wikipedia.org/wiki/Eadweard_Muybridge`. [Online; accessed 15-June-2009].

[2] Nobel prize website, 2009. URL `http://nobelprize.org/`.

[3] C. V. Shank and E. P. Ippen. Subpicosecond kilowatt pulses from a mode-locked cw dye laser. *Applied Physics Letters*, 24(8):373–375, 1974. doi: 10.1063/1.1655222.

[4] F. Krausz and M. Ivanov. Attosecond physics. *Reviews of Modern Physics*, 81(1):163, 2009. doi: 10.1103/RevModPhys.81.163.

[5] A. L. Cavalieri, Müller, N. Th. Uphues, V. S. Yakovlev, A. Baltus, B. Horvath, B. Schmidt, L. Blümel, R. Holzwarth, S. Hendel, M. Drescher, U. Kleineberg, P. M. Echenique, R. Kienberger, F. Krausz, and U. Heinzmann. Attosecond spectroscopy in condensed matter. *Nature*, 449:1029–1032, Oct 2007.

[6] R. W. Schoenlein, S. Chattopadhyay, H. H. W. Chong, T. E. Glover, P. A. Heimann, C. V. Shank, A. A. Zholents, and M. S. Zolotorev. Generation of femtosecond pulses of synchrotron radiation. *Science*, 287(5461):2237–2240, Jan 2000.

[7] B. J. Siwick, J. R. Dwyer, R. E. Jordan, and R. J. D. Miller. An atomic-level view of melting using femtosecond electron diffraction. *Science*, 302:1382–1385, 2003.

[8] P. Baum, D. S. Yang, and A. H. Zewail. 4D visualization of transitional structures in phase transformations by electron diffraction. *Science*, 318:788–792, 2007.

[9] A. L. Cavalieri, D. M. Fritz, S. H. Lee, P. H. Bucksbaum, D. A. Reis, J. Rudati, D. M. Mills, P. H. Fuoss, G. B. Stephenson, C. C. Kao, D. P. Siddons, D. P. Lowney, A. G. MacPhee, D. Weinstein, R. W. Falcone, R. Pahl, J. Als-Nielsen, C. Blome, S. Düsterer, R. Ischebeck, H. Schlarb, H. Schulte-Schrepping, Th. Tschentscher, J. Schneider, O. Hignette, F. Sette, and K. Sokolowski-Tinten. Clocking femtosecond x rays. *Physical Review Letters*, 94(11):114801, Mar 2005.

[10] L. Perfetti, P. A. Loukakos, M. Lisowski, U. Bovensiepen, H. Berger, S. Biermann, P. S. Cornaglia, A. Georges, and M. Wolf. Time evolution of the electronic structure of 1T-TaS_2 through the insulator-metal transition. *Physical Review Letters*, 97(6):067402, 2006. doi: 10.1103/PhysRevLett.97.067402.

[11] R. Peierls. *More Surprises in Theoretical Physics*. Princeton University Press, 1991.

[12] J. H. de Boer and E. J. W. Verwey. Semi-conductors with partially and with completely filled 3d-lattice bands. *Proceedings of the Physical Society*, 49(4S):59–71, 1937.

[13] E. Wigner. On the interaction of electrons in metals. *Physical Review*, 46(11):1002–1011, Dec 1934.

[14] N. F. Mott. The basis of the electron theory of metals, with special reference to the transition metals. *Proceedings of the Physical Society*, A62:416, 1949.

[15] N. F. Mott. Metal-insulator transition. *Reviews of Modern Physics*, 40(4):667, 1968.

[16] M. Imada, A. Fujimori, and Y. Tokura. Metal-insulator transitions. *Review of Modern Physics*, 70(4):1039–1263, Oct 1998.

[17] C. V. Shank, R. Yen, R. L. Fork, J. Orenstein, and G. L. Baker. Picosecond dynamics of photoexcited gap states in polyacetylene. *Physical Review Letters*, 49(22):1660–1663, Nov 1982.

[18] C. V. Shank, R. Yen, and C. Hirlimann. Time-resolved reflectivity measurements of femtosecond-optical-pulse-induced phase transitions in silicon. *Physical Review Letters*, 50(6):454–457, Feb 1983.

[19] C. W. Siders, A. Cavalleri, K. Sokolowski-Tinten, C. Toth, T. Guo, M Kammler, H. H. von Hoegen, K. R. Wilson, D. von der Linde, and C. P. J. Barty. Detection of nonthermal melting by ultrafast x-ray diffraction. *Nature*, 286(5443):1340–1342, Nov 1999.

[20] S. Koshihara, Y. Tokura, T. Mitani, G. Saito, and T. Koda. Photoinduced valence instability in the organic molecular compound tetrathiafulvalene-p-chloranil (TTF-CA). *Physical Review B*, 42(10):6853–6856, Oct 1990. doi: 10.1103/PhysRevB.42.6853.

[21] A. Cavalleri, Cs. Tóth, C. W. Siders, J. A. Squier, F. Ráksi, P. Forget, and J. C. Kieffer. Femtosecond structural dynamics in VO_2 during an ultrafast solid-solid phase transition. *Physical Review Letters*, 87(23):237401, Nov 2001.

[22] K. Sokolowski-Tinten, C. Blome, J. Blums, A. Cavalleri, C. Dietrich, A. Tarasevitch, I. Uschmann, E. Forster, M. Kammler, M. Horn von Hoegen, and D. von der Linde. Femtosecond x-ray measurement of coherent lattice vibrations near the lindemann stability limit. *Nature*, 422(6929):287, 2003.

[23] M. Chollet, L. Guerin, N. Uchida, S. Fukaya, H. Shimoda, T. Ishikawa, K. Matsuda, T. Hasegawa, A. Ota, H. Yamochi, G. Saito, R. Tazaki, S. Adachi, and S. Koshihara. Gigantic photoresponse in 1/4-filled-band organic salt $(EDO\text{-}TTF)_2PF_6$. *Science*, 307 (5706):86, Jan 2005.

[24] K. Miyano, T. Tanaka, Y. Tomioka, and Y. Tokura. Photoinduced insulator-to-metal transition in a perovskite manganite. *Physical Review Letters*, 78(22):4257–4260, Jun 1997.

[25] G. Yu, C. H. Lee, A. J. Heeger, N. Herron, and E. M. McCarron. Transient photoinduced conductivity in single crystals of $YBa_2Cu_3O_{6.3}$: 'Photodoping' to the metallic state. *Physical Review Letters*, 67(18):2581–2584, Oct 1991.

[26] A. Cavalleri, M. Rini, H. H. W. Chong, S. Fourmaux, T. E. Glover, P. A. Heimann, J. C. Kieffer, and R. W. Schoenlein. Band-selective measurements of electron dynamics in VO_2 using femtosecond near-edge x-ray absorption. *Physical Review Letters*, 95(6): 067405, Aug 2005.

[27] M. Rini, R. Tobey, N. Dean, J. Itatani, Y. Tomioka, Y. Tokura, R. W. Schoenlein, and A. Cavalleri. Control of the electronic phase of a manganite by mode-selective vibrational excitation. *Nature*, 449(7158):72–74, Jan 2007.

[28] M. Eckstein and M. Kollar. Theory of time-resolved optical spectroscopy on correlated electron systems. *Physical Review B*, 78(20):205119, 2008.

[29] A. Cavalleri, Th. Dekorsy, H. H. W. Chong, J. C. Kieffer, and R. W. Schoenlein. Evidence for a structurally-driven insulator-to-metal transition in VO_2 : A view from the ultrafast timescale. *Physical Review B*, 70(16):161102, Oct 2004.

[30] John B. Goodenough. The two components of the crystallographic transition in VO_2. *Journal of Solid State Chemistry*, 3(4):490 – 500, 1971.

[31] A. Zylbersztejn and N. F. Mott. Metal-insulator transition in vanadium dioxide. *Physical Review B*, 11(11):4383–4395, Jun 1975.

[32] J. Hubbard. Electron correlations in narrow energy bands. ii. the degenerate band case. *Proceedings of the Royal Society*, A227:237, 1964.

[33] J. Zaanen, G. A. Sawatzky, and J. W. Allen. Band gaps and electronic structure of transition-metal compounds. *Physical Review Letters*, 55(4):418–421, Jul 1985.

[34] G. H. Jonker and J. H. Vansanten. Ferromagnetic compounds of manganese with perovskite structure. *Physica*, 16(3):337–349, 1950.

[35] Y. Tomioka, A. Asamitsu, H. Kuwahara, Y. Moritomo, and Y. Tokura. Magnetic-field-induced metal-insulator phenomena in $Pr_{1-x}Ca_xMnO_3$ with controlled charge-ordering instability. *Physical Review B*, 53(4):R1689–R1692, Jan 1996.

[36] E. Dagotto, T. Hotta, and A. Moreo. Colossal magnetoresistant materials: The key role of phase separation. *Physics Reports*, 344(1):1–153, Jan 2001.

[37] J. Kanamori. Crystal distortion in magnetic compounds. *Journal of Applied Physics Supplement*, 31(5):14s, Oct 1960.

[38] P. M. Woodward. Octahedral Tilting in Perovskites. I. Geometrical Considerations. *Acta Crystallographica Section B*, 53(1):32–43, Feb 1997.

[39] Y. Tokura and Tomioka Y. Colossal magnetoresistive manganites. *Journal of Magnetism and Magnetic Materials*, 200(1-3):1 – 23, 1999.

[40] C. Zener. Interaction between the d-shells in the transition metals. 2. Ferromagnetic compounds of manganese with perovskite structure. *Phys. Rev.*, 82(3):403–405, Jan 1951.

[41] J. Kanamori. Superexchange interaction and symmetry properties of electron orbitals. *Journal of Physics and Chemistry of Solids*, 10(2):87–98, Jan 1959.

[42] H. Y. Hwang, T. T. M. Palstra, S. W. Cheong, and B. Batlogg. Pressure effects on the magnetoresistance in doped manganese perovskites. *Physical Review B*, 52(21): 15046–15049, Jan 1995.

[43] A. Asamitsu, Y. Tomioka, H. Kuwahara, and Y. Tokura. Current switching of resistive states in magnetoresistive manganites. *Nature*, 388(6637):50–52, Jan 1997.

[44] V Kiryukhin, D Casa, JP Hill, B Keimer, A Vigliante, Y Tomioka, and Y Tokura. An X-ray-induced insulator-metal transition in a magnetoresistive manganite. *Nature*, 386 (6627):813–815, Jan 1997.

[45] R. I. Tobey, D. Prabhakaran, A. T. Boothroyd, and A. Cavalleri. Ultrafast electronic phase transition in $La_{1/2}Sr_{3/2}MnO_4$ by coherent vibrational excitation: Evidence for nonthermal melting of orbital order. *Physical Review Letters*, 101(19), Nov 2008.

[46] John B. Goodenough. Theory of the role of covalence in the perovskite-type manganites [La, M(II)]MnO_3. *Physical Review*, 100(2):564–573, Oct 1955.

[47] K. I. Kugel and D. I. Khomskii. The Jahn-Teller effect and magnetism: transition metal compounds. *Soviet Physics Uspekhi*, 25(4):231–256, 1982.

[48] D. I. Khomskii and K. I. Kugel. Orbital and magnetic structure of two-dimensional ferromagnets with Jahn-Teller ions. *Solid State Communications*, 13(4):763–766, 1973.

[49] G. Khaliullin and V. Oudovenko. Spin and orbital excitation spectrum in the kugel-khomskii model. *Physical Review B*, 56(22):R14243–R14246, Dec 1997.

[50] Y. Endoh, K. Hirota, S. Ishihara, S. Okamoto, Y. Murakami, A. Nishizawa, T. Fukuda, H. Kimura, H. Nojiri, K. Kaneko, and S. Maekawa. Transition between two ferromagnetic states driven by orbital ordering in $La_{0.88}Sr_{0.12}MnO_3$. *Physical Review Letters*, 82 (21):4328–4331, May 1999.

[51] K. Nakamura, T. Arima, A. Nakazawa, Y. Wakabayashi, and Y. Murakami. Polarization-dependent resonant-x-ray diffraction in charge- and orbital-ordering phase of $Nd_{1/2}Sr_{1/2}MnO_3$. *Physical Review B*, 60(4):2425–2428, Jul 1999.

[52] M. v. Zimmermann, J. P. Hill, Doon Gibbs, M. Blume, D. Casa, B. Keimer, Y. Murakami, Y. Tomioka, and Y. Tokura. Interplay between charge, orbital, and magnetic order in $Pr_{1-x}Ca_xMnO_3$. *Physical Review Letters*, 83(23):4872–4875, Dec 1999.

[53] S. B. Wilkins, P. D. Spencer, P. D. Hatton, S. P. Collins, M. D. Roper, D. Prabhakaran, and A. T. Boothroyd. Direct observation of orbital ordering in $La_{0.5}Sr_{1.5}MnO_4$ using soft x-ray diffraction. *Physical Review Letters*, 91(16):167205, Oct 2003.

[54] S. S. Dhesi, A. Mirone, C. De Nadaï, P. Ohresser, P. Bencok, N. B. Brookes, P. Reutler, A. Revcolevschi, A. Tagliaferri, O. Toulemonde, and G. van der Laan. Unraveling orbital ordering in $La_{0.5}Sr_{1.5}MnO_4$. *Physical Review Letters*, 92(5):056403, Feb 2004.

[55] Alexander L. Gaeta. Catastrophic collapse of ultrashort pulses. *Physical Review Letters*, 84(16):3582–3585, Apr 2000.

[56] G. Cerullo and S. De Silvestri. Ultrafast optical parametric amplifiers. *Review of Scientific Instruments*, 74(1):1–18, 2003.

[57] D. Brida, G. Cirmi, C. Manzoni, S. Bonora, P. Villoresi, S. De. Silvestri, and G. Cerullo. Sub-two-cycle light pulses at 1.6 μm from an optical parametric amplifier. *Optics Letters*, Jan 2008.

[58] Ian Walmsley, Leon Waxer, and Christophe Dorrer. The role of dispersion in ultrafast optics. *Review of Scientific Instruments*, 72(1):1–29, 2001.

[59] D. J. Kane and R. Trebino. Characterization of arbitrary femtosecond pulses using frequency-resolved optical gating. *IEEE Journal of Quantum Electronics*, 29(2):571–579, Jan 1993.

[60] D. Polli, L. Lüer, and G. Cerullo. High-time-resolution pump-probe system with broadband detection for the study of time-domain vibrational dynamics. *Review of Scientific Instruments*, 78(10):103108, 2007.

[61] G. Cerullo, M. Nisoli, S. Stagira, and S. De Silvestri. Sub-8-fs pulses from an ultra-broadband optical parametric amplifier in the visible. *Optics Letters*, 23(16):1283–1285, 1998.

[62] R. W. Schoenlein, W. P. Leemans, A. H. Chin, P. Volfbeyn, T. E. Glover, P. Balling, M. Zolotorev, K.J. Kim, S. Chattopadhyay, and C. V. Shank. Femtosecond x-ray pulses at 0.4 Å generated by 90° thomson scattering: A tool for probing the structural dynamics of materials. *Science*, 274:236–238, Oct 1996.

[63] M. Murnane, H. C. Kapteyn, M. D. Rosen, and R. W. Falcone. Ultrafast x-ray pulses from laser-produced plasmas. *Science*, 251:531–536, Feb 1991.

[64] C. Rischel, A. Rousse, I. Uschmann, P. A. Albouy, J. P. Geindre, P. Audebert, J.C. Gauthier, E. Froster, J. L. Martin, and A. Antonetti. Femtosecond time-resolved x-ray diffraction from laser-heated organic films. *Nature*, 390:490–492, Dec 1997.

[65] C. Rose-Petruck, R. Jimenez, T. Guo, A. Cavalleri, C. Siders, F. Raksi, J.A. Squier, B.C. Walker, K.R. Wilson, and C.P.J. Barty. Picosecond-milliångström lattice dynamics measured by ultrafast x-ray diffraction. *Nature*, 398:310–312, Feb 1999.

[66] A. Rousse, P. Audebert, J. P. Geindre, F. Falliès, J. C. Gauthier, A. Mysyrowicz, G. Grillon, and A. Antonetti. Efficient K_α x-ray source from femtosecond laser-produced plasmas. *Physical Review E*, 50(3):2200–2207, Sep 1994.

[67] D. T. Attwood. *Soft X-Rays and Extreme Ultraviolet Radiation: principles and applications*. Cambridge University Press, 2000.

[68] A. A. Zholents and M. S. Zolotorev. Femtosecond x-ray pulses of synchrotron radiation. *Physical Review Letters*, 76(6):912–915, Feb 1996.

[69] W. H. Knox, D. S. Chemla, G. Livescu, J. E. Cunningham, and J. E. Henry. Femtosecond carrier thermalization in dense Fermi seas. *Physical Review Letters*, 61(11): 1290–1293, Sep 1988. doi: 10.1103/PhysRevLett.61.1290.

[70] Y-X. Yan and K. A. Nelson. Impulsive stimulated light scattering. I. General theory. *The Journal of Chemical Physics*, 87(11), 1987.

[71] H. J. Zeiger, J. Vidal, T. K. Cheng, E. P. Ippen, G. Dresselhaus, and M. S. Dresselhaus. Theory for displacive excitation of coherent phonons. *Physical Review B*, 45(2):768–778, Jan 1992.

[72] G. A. Garrett, T. F. Albrecht, J. F. Whitaker, and R. Merlin. Coherent THz phonons driven by light pulses and the Sb problem: What is the mechanism? *Physical Review Letters*, 77(17):3661–3664, Oct 1996.

[73] T. E. Stevens, J. Kuhl, and R. Merlin. Coherent phonon generation and the two stimulated raman tensors. *Physical Review B*, 65(14):144304, Mar 2002.

[74] A. Cavalleri, S. Wall, C. Simpson, E. Statz, D. W. Ward, K. A. Nelson, M. Rini, and R. W. Schoenlein. Tracking the motion of charges in a terahertz light field by femtosecond x-ray diffraction. *Nature*, 442(7103):664, Jan 2006.

[75] M. Matsubara, Y. Okimoto, T. Ogasawara, Y. Tomioka, H. Okamoto, and Y. Tokura. Ultrafast photoinduced insulator-ferromagnet transition in the perovskite manganite $Gd_{0.55}Sr_{0.45}MnO_3$. *Physical Review Letters*, 99(20):207401, 2007. doi: 10.1103/PhysRevLett.99.207401.

[76] Elliott H. Lieb and F. Y. Wu. Absence of Mott transition in an exact solution of the short-range, one-band model in one dimension. *Physical Review Letters*, 20(25): 1445–1448, Jun 1968. doi: 10.1103/PhysRevLett.20.1445.

[77] C. Kim, A. Y. Matsuura, Z.-X. Shen, N. Motoyama, H. Eisaki, S. Uchida, T. Tohyama, and S. Maekawa. Observation of spin-charge separation in one-dimensional $SrCuO_2$. *Physical Review Letters*, 77(19):4054–4057, Nov 1996. doi: 10.1103/PhysRevLett.77.4054.

[78] S. Iwai, M. Ono, A. Maeda, H. Matsuzaki, H. Kishida, H. Okamoto, and Y. Tokura. Ultrafast optical switching to a metallic state by photoinduced Mott transition in a halogen-bridged nickel-chain compound. *Physical Review Letters*, 91(5):057401, Jul 2003. doi: 10.1103/PhysRevLett.91.057401.

[79] L. Perfetti, P. A. Loukakos, M. Lisowski, U. Bovensiepen, M. Wolf andH. Berger, S. Biermann, and A. Georges. Femtosecond dynamics of electronic states in the Mott insulator 1T-TaS_2 by time resolved photoelectron spectroscopy. *New Journal of Physics*, 10: 053019, 2008.

[80] H. Okamoto, H. Matsuzaki, T. Wakabayashi, Y. Takahashi, and T. Hasegawa. Photoinduced metallic state mediated by spin-charge separation in a one-dimensional organic Mott insulator. *Physical Review Letters*, 98(3):037401, 2007. doi: 10.1103/PhysRevLett.98.037401.

[81] A. Takahashi, H. Itoh, and M. Aihara. Photoinduced insulator-metal transition in one-dimensional Mott insulators. *Physical Review B*, 77(20):205105, 2008. doi: 10.1103/PhysRevB.77.205105.

[82] T. Hasegawa, T. Mochida, R. Kondo, S. Kagoshima, Y. Iwasa, T. Akutagawa, T. Nakamura, and G. Saito. Mixed-stack organic charge-transfer complexes with intercolumnar networks. *Physical Review B*, 62(15):10059–10066, Oct 2000. doi: 10.1103/PhysRevB.62.10059.

[83] K. Yakushi, T. Kusaka, and H. Kuroda. Low-teimperature reflection spectrum of K-TCNQ single crystal. *Chemical Physics Letters*, 68(1):139–142, Dec 1979.

[84] K. Tanimura. Femtosecond time-resolved reflection spectroscopy of photoinduced ionic-neutral phase transition in TTF-CA crystals. *Physical Review B*, 70(14):144112, Oct 2004. doi: 10.1103/PhysRevB.70.144112.

[85] J. D. Jackson. *Classical electrodynamics third edition.* Wiley, 1998.

[86] R. M. Fye, M. J. Martins, D. J. Scalapino, J. Wagner, and W. Hanke. Drude weight, optical conductivity, and flux properties of one-dimensional Hubbard rings. *Physical Review B*, 44(13):6909–6915, Oct 1991. doi: 10.1103/PhysRevB.44.6909.

[87] F. H. L. Essler, H. Frahm, F. Göhmann, A. Klümper, and V. E. Korepin. *The One-Dimensional Hubbard Model.* Cambridge University Press, 2005.

[88] N. Takubo, I. Onishi, K. Takubo, T. Mizokawa, and K. Miyano. Photoinduced metal-to-insulator transition in a manganite thin film. *Physical Review Letters*, 101(17):177403, 2008. doi: 10.1103/PhysRevLett.101.177403.

[89] T. Ogasawara, T. Kimura, T. Ishikawa, M. Kuwata-Gonokami, and Y. Tokura. Dynamics of photoinduced melting of charge/orbital order in a layered manganite $La_{0.5}Sr_{1.5}MnO_4$. *Physical Review B*, 63(11):113105, Mar 2001. doi: 10.1103/PhysRevB.63.113105.

[90] E. O. Wollan and W. C. Koehler. Neutron diffraction study of the magnetic properties of the series of perovskite-type compounds $[(1-x)\mathrm{La}, x\mathrm{Ca}]\mathrm{MnO}_3$. *Physical Review*, 100 (2):545–563, Oct 1955. doi: 10.1103/PhysRev.100.545.

[91] J. Rodríguez-Carvajal, M. Hennion, F. Moussa, A. H. Moudden, L. Pinsard, and A. Revcolevschi. Neutron-diffraction study of the Jahn-Teller transition in stoichiometric $LaMnO_3$. *Physical Review B*, 57(6):R3189–R3192, Feb 1998. doi: 10.1103/PhysRevB.57.R3189.

[92] N. N. Kovaleva, A. V. Boris, C. Bernhard, A. Kulakov, A. Pimenov, A. M. Balbashov, G. Khaliullin, and B. Keimer. Spin-controlled Mott-Hubbard bands in $LaMnO_3$ probed by optical ellipsometry. *Physical Review Letters*, 93(14):147204, Oct 2004. doi: 10.1103/PhysRevLett.93.147204.

[93] K. Tobe, T. Kimura, Y. Okimoto, and Y. Tokura. Anisotropic optical spectra in a detwinned $LaMnO_3$ crystal. *Physical Review B*, 64(18):184421, Oct 2001. doi: 10.1103/PhysRevB.64.184421.

[94] S. Satpathy, Zoran S. Popović, and Filip R. Vukajlović. Electronic structure of the perovskite oxides: $La_{1-x}Ca_xMnO_3$. *Physical Review Letters*, 76(6):960–963, Feb 1996. doi: 10.1103/PhysRevLett.76.960.

[95] J. H. Jung, K. H. Kim, D. J. Eom, T. W. Noh, E. J. Choi, Jaejun Yu, Y. S. Kwon, and Y. Chung. Determination of electronic band structures of $CaMnO_3$ and $LaMnO_3$ using optical-conductivity analyses. *Physical Review B*, 55(23):15489–15493, Jun 1997. doi: 10.1103/PhysRevB.55.15489.

[96] D Prabhakaran, A I Coldea, A T Boothroyd, and S J Blundell. Growth of large $La_{1-x}Sr_xMnO_3$ single crystals under argon pressure by the floating-zone technique. *Journal of Crystal Growth*, 237:806–809, Apr 2002.

[97] A. J. Sabbah and D. M. Riffe. Femtosecond pump-probe reflectivity study of silicon carrier dynamics. *Physical Review B*, 66(16):165217, Oct 2002. doi: 10.1103/PhysRevB.66.165217.

[98] M. N. Iliev, M. V. Abrashev, H.-G. Lee, V. N. Popov, Y. Y. Sun, C. Thomsen, R. L. Meng, and C. W. Chu. Raman spectroscopy of orthorhombic perovskitelike $YMnO_3$ and $LaMnO_3$. *Physical Review B*, 57(5):2872–2877, Feb 1998. doi: 10.1103/PhysRevB.57.2872.

[99] R. Krüger, B. Schulz, S. Naler, R. Rauer, D. Budelmann, J. Bäckström, K. H. Kim, S-W. Cheong, V. Perebeinos, and M. Rübhausen. Orbital ordering in $LaMnO_3$ investigated by resonance raman spectroscopy. *Physical Review Letters*, 92(9):097203, Mar 2004.

[100] Fabrice Vallée. Time-resolved investigation of coherent lo-phonon relaxation in iii-v semiconductors. *Physical Review B*, 49(4):2460–2468, Jan 1994. doi: 10.1103/PhysRevB.49.2460.

[101] F. Moussa, M. Hennion, J. Rodriguez-Carvajal, H. Moudden, L. Pinsard, and A. Revcolevschi. Spin waves in the antiferromagnet perovskite $LaMnO_3$: A neutron-scattering study. *Physical Review B*, 54(21):15149–15155, Dec 1996. doi: 10.1103/PhysRevB.54.15149.

[102] T. Chatterji, Paul F. Henry, and B. Ouladdiaf. Neutron diffraction investigation of the magneto-elastic effect in $LaMnO_3$. *Physical Review B*, 77(21):212403, 2008. doi: 10.1103/PhysRevB.77.212403.

[103] A. Melnikov, A. Povolotskiy, and U. Bovensiepen. Magnon-enhanced phonon damping at Gd(0001) and Tb(0001) surfaces using femtosecond time-resolved optical second-harmonic generation. *Physical Review Letters*, 100(24):247401, 2008. doi: 10.1103/PhysRevLett.100.247401.

[104] Muneaki Hase, Kohji Mizoguchi, Hiroshi Harima, Shin-ichi Nakashima, and Kiyomi Sakai. Dynamics of coherent phonons in bismuth generated by ultrashort laser pulses. *Physical Review B*, 58(9):5448–5452, Sep 1998. doi: 10.1103/PhysRevB.58.5448.

[105] G. Subías, J. Herrero-Martín, J. García, J. Blasco, C. Mazzoli, K. Hatada, S. Di Matteo, and C. R. Natoli. Origin of the resonant x-ray scattering in $LaMnO_3$. *Physical Review B*, 75(23):235101, 2007. doi: 10.1103/PhysRevB.75.235101.

[106] M. Fiebig, K. Miyano, Y. Tomioka, and Y. Tokura. Visualization of the Local Insulator-Metal Transition in $Pr_{0.7}Ca_{0.3}MnO_3$. *Science*, 280(5371):1925–1928, 1998. doi: 10.1126/science.280.5371.1925.

[107] M. Fiebig, K. Miyano, T. Satoh, Y. Tomioka, and Y. Tokura. Action spectra of the two-stage photoinduced insulator-metal transition in $Pr_{1-x}Ca_xMnO_3$. *Physical Review B*, 60(11):7944–7949, Sep 1999. doi: 10.1103/PhysRevB.60.7944.

[108] M. Fiebig, K. Miyano, Y. Tomioka, and Y. Tokura. Reflection spectroscopy on the photoinduced local metallic phase of $Pr_{0.7}Ca_{0.3}MnO_3$. *Applied Physics Letters*, 74(16): 2310–2312, 1999. doi: 10.1063/1.123834.

[109] M Fiebig, K Miyano, Y Tomioka, and Y Tokura. Ultrafast photoinduced insulator-metal transition in $Pr_{0.7}Ca_{0.3}MnO_3$. *Journal of Luminescence*, 87-89:82 – 85, 2000.

[110] M. Kim, H. Barath, S. L. Cooper, P. Abbamonte, E. Fradkin, M. Rübhausen, C. L. Zhang, and S.-W. Cheong. Raman scattering studies of the temperature- and field-induced melting of charge order in $La_xPr_yCa_{1-x-y}MnO_3$. *Physical Review B*, 77(13): 134411, 2008. doi: 10.1103/PhysRevB.77.134411.

[111] E. Saitoh, S. Okamoto, K. T. Takahashi, K. Tobe, K. Yamamoto, T. Kimura, S. Ishihara, S. Maekawa, and Y. Tokura. Observation of orbital waves as elementary excitations in a solid. *Nature*, 410(6825):180–183, Jan 2001.

[112] K. P. Schmidt, M. Grüninger, and G. S. Uhrig. Fate of orbitons coupled to phonons. *Physical Review B*, 76(7):075108, 2007.

[113] J. van den Brink. Orbital excitations in $LaMnO_3$. *Physical Review Letters*, 87(21): 217202, Nov 2001.

[114] F. Forte, L. J. P. Ament, and J. van den Brink. Single and double orbital excitations probed by resonant inelastic x-ray scattering. *Physical Review Letters*, 101(10):106406, Sep 2008.

[115] M. Grüninger, R. Ruckamp, M. Windt, P. Reutler, C. Zobel, T. Lorenz, A. Freimuth, and A. Revcolevschi. Orbital physics - experimental quest for orbital waves. *Nature*, 418(6893):39–40, Jan 2002.

[116] M. K. Dalai, P. Pal, B. R. Sekhar, N. L. Saini, R. K. Singhal, K. B. Garg, B. Doyle, S. Nannarone, C. Martin, and F. Studer. Electronic structure of $Pr_{0.67}Ca_{0.33}MnO_3$ near the Fermi level studied by ultraviolet photoelectron and x-ray absorption spectroscopy. *Physical Review B*, 74(16):165119, 2006.

[117] F. M. F. de Groot, M. Grioni, J. C. Fuggle, J. Ghijsen, G. A. Sawatzky, and H. Petersen. Oxygen 1s x-ray-absorption edges of transition-metal oxides. *Physical Review B*, 40(8): 5715–5723, Sep 1989.

[118] O. Toulemonde, F. Millange, F. Studer, B. Raveau, J. H. Park, and C. T. Chen. Changes in the Jahn-Teller distortion at the metal-insulator transition in CMR manganites $(Pr,Nd)_{0.7}(Sr,Ca)_{0.3}MnO_3$. *J Phys-Condens Mat*, 11(1):109–120, Jan 1999.

[119] M. Abbate, F. M. F. de Groot, J. C. Fuggle, A. Fujimori, O. Strebel, F. Lopez, M. Domke, G. Kaindl, G. A. Sawatzky, M. Takano, Y. Takeda, H. Eisaki, and S. Uchida. Controlled-valence properties of $La_{1-x}Sr_xFeO_3$ and $La_{1-x}Sr_xMnO_3$ studied by soft-x-ray absorption spectroscopy. *Physical Review B*, 46(8):4511–4519, Aug 1992.

[120] J.-H. Park, T. Kimura, and Y. Tokura. Competition between lattice distortion and charge dynamics for the charge carriers of double-layered manganites. *Physical Review B*, 58(20):R13330–R13333, Nov 1998.

[121] N. Mannella, A. Rosenhahn, M. Watanabe, B. Sell, A. Nambu, S. Ritchey, E. Arenholz, A. Young, Y. Tomioka, and C. S. Fadley. Temperature-dependent x-ray absorption spectroscopy of colossal magnetoresistive perovskites. *Physical Review B*, 71(12):125117, Mar 2005.

[122] S. L. Johnson, P. A. Heimann, A. M. Lindenberg, H. O. Jeschke, M. E. Garcia, Z. Chang, R. W. Lee, J. J. Rehr, and R. W. Falcone. Properties of liquid silicon observed by time-resolved x-ray absorption spectroscopy. *Physical Review Letters*, 91(15):157403, Oct 2003. doi: 10.1103/PhysRevLett.91.157403.

[123] A. Cavalleri, H. H. W. Chong, S. Fourmaux, T. E. Glover, P. A. Heimann, J. C. Kieffer, B. S. Mun, H. A. Padmore, and R. W. Schoenlein. Picosecond soft x-ray absorption measurement of the photoinduced insulator-to-metal transition in VO_2. *Physical Review B*, 69(15):153106, Apr 2004.

[124] H. J. Bakker, S. Hunsche, and H. Kurz. Time-resolved study of phonon polaritons in $LiTaO_3$. *Physical Review B*, 48(18):13524–13537, Nov 1993. doi: 10.1103/PhysRevB.48.13524.

[125] J. K. Wahlstrand and R. Merlin. Cherenkov radiation emitted by ultrafast laser pulses and the generation of coherent polaritons. *Physical Review B*, 68(5):054301, Aug 2003. doi: 10.1103/PhysRevB.68.054301.

[126] T. E. Stevens, J. K. Wahlstrand, J. Kuhl, and R. Merlin. Cherenkov Radiation at Speeds Below the Light Threshold: Phonon-Assisted Phase Matching. *Science*, 291 (5504):627–630, 2001. doi: 10.1126/science.291.5504.627.

[127] M. Born and K. Huang. *Dynamical theory of crystal lattices*. Oxford University Press, 1954.

[128] A. M. Lindenberg, I. Kang, S. L. Johnson, T. Missalla, P. A. Heimann, Z. Chang, J. Larsson, P. H. Bucksbaum, H. C. Kapteyn, H. A. Padmore, R. W. Lee, J. S. Wark, and R. W. Falcone. Time-resolved x-ray diffraction from coherent phonons during a laser-induced phase transition. *Physical Review Letters*, 84(1):111–114, Jan 2000. doi: 10.1103/PhysRevLett.84.111.

[129] S. L. Johnson, P. Beaud, E. Vorobeva, C. J. Milne, É. D. Murray, S. Fahy, and G. Ingold. Directly observing squeezed phonon states with femtosecond x-ray diffraction. *Physical Review Letters*, 102(17):175503, 2009. doi: 10.1103/PhysRevLett.102.175503.

[130] S.C. Abrahams and J.L. Bernstein. Ferroelectric lithium tantalate–1. single crystal x-ray diffraction study at 24°C. *Journal of Physics and Chemistry of Solids*, 28(9):1685 – 1692, 1967.

[131] S.C. Abrahams, Walter C. Hamilton, and A. Sequeira. Ferroelectric lithium tantalate–2. single crystal neutron diffraction study at 24°C. *Journal of Physics and Chemistry of Solids*, 28(9):1693 – 1698, 1967.

[132] A. S. Barker, A. A. Ballman, and J. A. Ditzenberger. Infrared study of the lattice vibrations in $LiTaO_3$. *Physical Review B*, 2(10):4233–4239, Nov 1970. doi: 10.1103/PhysRevB.2.4233.

[133] I. P. Kaminow and W. D. Johnston. Quantitative determination of sources of the electro-optic effect in $LiNbO_3$ and $LiTaO_3$. *Physical Review*, 160(3):519–522, Aug 1967. doi: 10.1103/PhysRev.160.519.

[134] J.L. Young and R.O. Nelson. A summary and systematic analysis of FDTD algorithms for linearly dispersive media. *Antennas and Propagation Magazine, IEEE*, 43(1):61–126, Feb 2001. doi: 10.1109/74.920019.

[135] David Ward. *Polaritonics: An Intermediate Regime Between Electronics and Photonics*. PhD thesis, Massachusetts Institute of Technology, 2005.

[136] J-P. Berenger. A perfectly matched layer for the absorption of electromagnetic waves. *Journal of Computational Physics*, 114(2):185–200, 1994. doi: http://dx.doi.org/10.1006/jcph.1994.1159.

[137] B.L. Henke, E.M. Gullikson, and J.C. Davis. X-ray interactions: photoabsorption, scattering, transmission, and reflection at E=50-30000 eV, Z=1-92. *Atomic Data and Nuclear Data Tables*, 54(2):181–342, Jul 1993.

[138] M. E. Wieser. Atomic weights of the elements 2005 (iupac technical report). *Pure and Applied Chemistry*, 78(11):2051–2066, 2006.

[139] János Hebling, Ka-Lo Yeh, Matthias C. Hoffmann, Balázs Bartal, and Keith A. Nelson. Generation of high-power terahertz pulses by tilted-pulse-front excitation and their application possibilities. *J. Opt. Soc. Am. B*, 25(7):B6–B19, 2008.

[140] F. Schmitt, P. S. Kirchmann, U. Bovensiepen, R. G. Moore, L. Rettig, M. Krenz, J.-H. Chu, N. Ru, L. Perfetti, D. H. Lu, M. Wolf, I. R. Fisher, and Z.-X. Shen. Transient Electronic Structure and Melting of a Charge Density Wave in $TbTe_3$. *Science*, 321 (5896):1649–1652, 2008. doi: 10.1126/science.1160778.